Fall 2019

A Non-Contacting System for Rail Neutral Temperature and Stress Measurements

Katelyn Knopf

A Non-Contacting System for Rail Neutral Temperature and Stress Measurements

By

Katelyn Knopf

Bachelor of Science
University of South Carolina, 2018

Submitted in Partial Fulfillment of the Requirements

For the Degree of Master of Science in

Civil Engineering

College of Engineering and Computing

University of South Carolina

2019

Accepted By:

Dimitris Rizos, Director of Thesis

Yu Qian, Reader

Robert Mullen, Reader

Michael Sutton, Reader

Cheryl L. Addy, Vice Provost and Dean of the Graduate School

Acknowledgements

This thesis would not have been possible without the devotion and support of the following people. I would like to express my thanks and gratitude to my advisor, Dr. Dimitris Rizos for initially motivating me to apply for the Magellan Scholar that ultimately led to the completion of my M.S. degree. I have learned so much from having you as a mentor and am beyond grateful for all the time and energy you have put towards helping me complete this chapter of my life. Furthermore, I would like to thank Dr. Robert Mullen, Dr. Yu Qian, and Dr. Michael Sutton for being a part of my thesis committee and for all the additional help and guidance you have provided. Your sound advice has led to many great advancements in my research. I would like to thank Dr. Iman Asareh for always sharing your wisdom in answering the many questions I had; or for providing me with many valuable resources. Additionally, I would like to express my sincere thanks to Kevin Barberena for all the laboratory testing you have performed with me; in addition to all the extra help you have provided. I could not have done it without you, and I am glad that I can now call you not only a colleague, but a friend.

This work has been partially funded by the Federal Railroad Administration (FRA) under contract 693JJ619C000007. The opinions expressed in this article are solely those of the authors and do not represent the opinions of the funding agency.

Abstract

Continuous Welded Rail (CWR) has become the standard in modern railway track construction around the world because it alleviates well-documented disadvantages of rail joints in a track. CWR practice results in long segments of continuous rail in the track that will develop significant thermal elongation. To avoid the use of impractical large thermal expansion joints and limit the expected thermal elongation, the rail is anchored to the ties. Consequently, the rail is exposed to higher thermal stress demands as the rail temperature varies. At the time a CWR is laid, the rail is free of thermal stresses; the temperature at that time is known as the Rail Neutral Temperature (RNT). As temperatures deviate from the RNT, significant tensile or compressive thermal stresses are introduced longitudinally, leading to potential failures, including pull-apart and buckling that compromise the integrity of the track and the safety of train operation. Although the CWR installation procedures control RNT, it generally decreases over time. Since a decrease in RNT increases the risk of buckling due to moderate temperature increases, there is a need to determine the state of stress in the rail at different temperatures, as well as changes in the RNT.

Existing methods meet this need with various success levels but are not free of shortcomings. Disadvantages are related to the ease of implementation, system

complexity, practicality, reliability, simplicity, cost, and instrumentation demands. All methods rely on data collected through means of contact with the rail. We propose a novel concept for measuring stress in rail and determining the RNT. The proposed technology is a non-contacting method that uses stereo-vision and three-dimensional (3D) Digital Image Correlation (StereoDIC) technology for full-field deformation and strain measurements. The StereoDIC system acquires rail deformations within a thermal cycle and processes the data in two steps. Initially, a reference free estimate of the RNT is obtained. Subsequently, the longitudinal stress in the rail is estimated as a function of the temperature. The StereoDIC hardware and software proposed is a technology developed at the University of South Carolina (USC). The method to process the StereoDIC measurements is the true innovation presented in this work.

Table of Contents

List of Tables

List of Figures

Chapter 1. Introduction

This chapter presents background information and identifies a critical problem in the rail industry, as well as sets the objectives for this work.

1.1 Problem Statement

The rail industry has been a driving force behind economic development in the United States for over two centuries, moving people and goods across the country and beyond. The industry's sustained growth depends heavily on the status of the infrastructure and its ability to adopt new technologies. Continuous Welded Rail (CWR) has become the standard in modern railway track construction around the world because it alleviates well-documented disadvantages of rail joints in a track. CWR practice eliminates thermal expansion joints and results in long segments of continuous rail in the track. At the time a CWR is laid, the rail is free of thermal stresses; the temperature at that time is known as the Rail Neutral Temperature (RNT). As temperatures deviate from the RNT, significant tensile or compressive longitudinal stresses develop, leading to rail buckling or pull-apart that compromises the integrity of the track and the safety of train operations (Chinowsky, et al. 2019). Such failures are among the leading causes of railway derailments (Liu, et al. 2013; Palese and Zarembski 2006). Current practices to prevent buckling from occurring include reducing rail traffic during extreme elevated

temperatures by introducing slow orders and sometimes track closure, which is very disruptive to track operations (Chinowsky, et al. 2019). Understanding the impact of temperature variations on the longitudinal stress in CWR has become fundamental to track design and rail installation. The anchoring of the rail on the ties imposes boundary conditions that restrict expansion and contraction of the rail. Consequently, changes in the ambient temperature conditions cause fluctuations in the rail temperature that lead to the development of axial compressive or tensile stresses that induce rail failures. In today's practice, the rail is installed at a pre-determined temperature, typically between 32°C and 43°C (Rizzo and Nasrollahi 2019), accounting for regional climate projections to mitigate extreme temperature deviations from the RNT. Although the CWR installation procedures control the RNT to preclude buckling under typical seasonal temperature cycles (A. Kish 2013), the RNT in a track segment generally decreases (rarely increases) over time due to factors related to operating conditions, repair, maintenance and the associated track deformations and shifting of the track structure (Rizzo and Nasrollahi 2019). Furthermore, with climate projections continuing to forecast an increase in average ambient temperatures, along extended extreme temperature durations, it is imperative to address the lack of efficient and effective monitoring and prevention methods existing today.

1.2 Objectives of this Thesis

This thesis presents the fundamental concepts for the development of a novel method for estimating the RNT and determining the longitudinal (axial) stress in rail. The proposed method belongs to the Deformation Measurements broader family of methods.

The proposed method is based on the hypotheses pertaining to the non-uniform thermal deformations of rail installed in the track, due to constraints in the longitudinal and transverse directions. These non-uniform deformations and the strain can be measured through a non-contacting vision-based data acquisition system and correlated to the RNT and longitudinal stress in the rail. The objectives of this thesis are to:

1. Study the deformation patterns of the rail in track and verify and validate the hypotheses for which the proposed method is developed on through simulations and laboratory investigations.
2. Propose a methodology that processes the deformation measurements and correlates them to the RNT and longitudinal stress in the rail.
3. Investigate the effects of track parameters and testing procedures on rail deformations due to thermal loadings through computer simulations.
4. Demonstrate and verify the proposed method for RNT and longitudinal stress calculations using simulated measurements.

1.3 Organization of this Thesis

The thesis is organized as follows: Chapter 1 identifies the problem and sets the objectives of this work. Chapter 2 presents the current state of knowledge in the field, discusses competing methods and summarizes the advantages and disadvantages, and introduces the proposed technology adopted in this work. Chapter 3 states the initial hypotheses and discusses the development of the proposed measurement concept through qualitative investigations, experimental measurements, and finite element

computer simulations. The developed RNT and stress measurement system is then presented. Chapter 4 discusses the physical rail system and describes the computer simulations developed of a simplified rail system by defining the model components, material properties, boundary conditions, connections, and loadings. Chapter 5 presents the investigated parametric studies, conducted through computer simulations, pertaining to the boundary conditions, heating techniques, heating surface areas, rail geometry, tie spacing, and track stiffness and provides an overall assessment determining the critical parameters that will serve as a guide for future construction of a full-scale prototype system. Chapter 6 implements the proposed measurement method on computer simulated measurements to obtain an RNT estimate and the longitudinal stress in rail for method verification. Chapter 7 states the conclusions of this work and provides recommendations for future experimental work and potential improvements to computer simulations.

Chapter 2. General Background

This chapter presents a critical discussion of existing and competing methods, identifies advantages and shortcomings of these methods, and introduces the details of the proposed technology adopted in this work.

2.1 Review of Existing and Competing Methods

Existing methods and technologies meet the need to estimate the RNT and longitudinal stress in rail at various success levels, however, they are not free of shortcomings (Kish and Samavedam 2013; Arts 2011). The disadvantages are related to the ease of implementation, system complexity, practicality, accuracy, reliability, simplicity, cost, and instrumentation demands. Some of the existing techniques are destructive and disrupt train operations, and all methods rely on data collected through some sort of contact of the equipment/instrumentation with the rail. Some of these technologies exist as commercial products, while others are at a research and development phase. These methods can be grouped with respect to the underlying basic principles as: (i) rail cutting; (ii) rail lifting; (iii) deformation measurements; (iv) ultrasonic; (v) x-ray; (vi) magnetics; (vii) piezoelectrics; (viii) vibro-elastics. Techniques (i)-(iii) have limited acceptance in the industry due to the destructive and disruptive nature. The remaining techniques have been proven ineffective except in some laboratory

applications (Kish and Samavedam 2013). These techniques are discussed further in the following sections.

2.1.1 Rail Cutting

The most commonly used method found in practice today is the rail cutting method. This simplistic approach entails marking two points 100 mm apart along the rail base flange, releasing the rail from the ties, and severing the rail at the center between these marked points (Johnson 2004). Upon severing the rail, the longitudinal displacement between the cuts is measured with a sliding caliber, as well as the rail temperature, T_R. A negative displacement, -e, suggests that the rail is in compression, and thus indicating that the RNT is lower than the rail temperature. Whereas a positive displacement, +e, suggests the rail is in tension, and thus indicating that the RNT is higher than the rail temperature. With these two variables, the RNT can then be directly calculated through Hooke's thermoelastic law:

$$e = \alpha * L * (RNT - T_R) \quad (1)$$

From the equation above, the *RNT* is computed as a function of the displacement, e, thermal expansion coefficient, α, length, L, and rail temperature, T_R. With the RNT calculated, the rail can be adjusted to the desired RNT through destressing procedures which use thermal and/or mechanical techniques to reset the rails to a new RNT (A. Kish 2005). The advantages of this method are that it is a well-known and established method with no additional educational requirements, it does not require a stress-free reference measurement (Arts 2011), and it is found to be accurate to ± 2°C in normal conditions of

the actual RNT (Johnson 2004). However, this technique is: (i) destructive to the track, (ii) a time-consuming procedure, and (iii) disruptive to train operations due to track closure.

2.1.2 Rail Lifting

The rail lifting technique is another common method found in practice. The basis behind this technique pertains to the beam column bending theory which states that the axial load is a function of vertical stiffness (Johnson 2004). This method involves unclipping 30 m of rail and inflicting a vertical force at the center of the unclipped rail length (Kjell and Johnson 2009). The magnitude of force required to lift the rail to a pre-determined distance, and the rail temperature are measured and used to directly compute the rail stiffness. Commercial products are available that automatically calculate the RNT through force distribution triangles. The advantages of this method are that it is a cost-effective technique, a single measurement typically takes about an hour (Weaver and Damljanovic 2005), and is sufficiently accurate at estimating the RNT within ± 3.5°C (Johnson 2004). Nevertheless, this technique is: (i) semi-destructive to the track, (ii) limited within curved track regions, (iii) disruptive to train operations, and (iv) it cannot be executed if the rail is in compression. If the rail is in compression, 30 m of unclipped rail will buckle before it vertically lifts (Johnson 2004). Therefore, this technique can only be used to measure tension, when the rail temperature is below the RNT (Rizzo and Nasrollahi 2019).

2.1.3 Deformation Methods

Deformation methods is a group of RNT measurement techniques that can be carried out with instrumentation including strain gauges or extensometer sensors. Strain

gauges have a unique electrical resistance that can then be used to calculate rail deformations (Arts 2011). This method operates by sending a current along the strain gauge wire and measures the voltage in the sensor that is proportional to the resistance. The voltage change is correlated to the change in gauge length, which is defined by the resistance in the wire. Temperature sensors must also be equipped with the strain gauges to measure the existing rail temperature. Given that this material is linearly elastic, the stress can then be directly computed through Hooke's law. The advantages of this method are that it is a non-destructive technique, a proven and lasting system, and has the capability to sustain environmental challenges (Arts 2011). However, the disadvantages of this method are: (i) requires rail contact, (ii) can be time consuming due to instrumentation installation, and (iii) relies on a changing dimension to indicate force (if the rail is not thermally loaded, data cannot be obtained regarding the rail stress state), and (iv) the thermal strain at the time of rail installation or a zero-force measurement is required. If the rail is already installed in a track, an additional measurement technique is necessary to implement this method.

2.1.4 Ultrasonic Technique

The ultrasonic technique is an indirect method that has been successfully developed in other applications but is still within the experimental stages in rail application. Ultrasonic techniques take advantage of the linear relationship between the velocity of propagating sound waves in a medium and the stress in a material (Alers and Manzanares 1990). A technique explored is known as the ultrasonic birefringence method. Generally, the rail is excited with an ultrasonic wave to obtain the linearly

polarized shear waves with respect to the sound propagation velocity (Szelazek 1998). This sound velocity is then correlated to stress based on rail material properties. The advantages of this technique include that it is non-destructive, produces rapid data acquisitions, enables continuous time measurements, and is not disruptive to train operations (Johnson 2004). However, the shortcomings of this technique are: (i) requires rail contact, (ii) a stress-free reference measurement is necessary, (iii) fairly sensitive to material structure and defects, and (iv) relies on the assumption that acoustic properties and residual stress are constant to accurately implement the method (Szelazek 1998).

2.1.5 Magnetics Method

The magnetics method is an indirect method based on the Barkhausen effect. The Barkhausen effect is produced by longitudinally energizing a beam to a specified audio frequency range to generate a magnetic field on the rail. Subsequently, due to the magno-elastic interaction found in rail's ferromagnetic microstructure, high frequency electromagnet and acoustic response signals are obtained (Posgay, et al. 1999). These electromagnetic and acoustic response signals are also known as the level of Barkhausen noise that exists on the surface of the energized region. The response signals are used to generate a magnetic field and the permeability of the magnetic field is investigated. An increase in the permeability, indicates an increase in tension, and vice-versa for compression (Wegner 2007). Temperature sensors must equip this technique to obtain an RNT estimate. The advantages of this method include that it is non-destructive, sufficiently accurate at estimating the RNT within ±3°C, and the rail can exist in either tension or compression. However, the disadvantages of this method are: (i) the

Barkhausen effect is sensitive to various parameters (geometry, the resonance and reflections, surface roughness, contamination/corrosion of instrumentation, and acoustic coupling of sensors (Posgay, et al. 1999, Wegner 2007), (ii) requires elimination of all local surface perturbations (Austill 1991), (iii) residual stresses influence the measurements (Wegner 2007), (iv) high instrumentation demands, (v) time-consuming calibration process, and (vi) a reference measurement from an identical material is required to correlate the response signals to stress values.

2.1.6 X-Ray Diffraction

The x-ray diffraction method is an indirect approach at capturing the strains in the crystal lattice structure of rail. The interplanar spacing of a crystallite at various angles is computed (Hauk 1997) utilizing the Bragg equation. The Bragg equation requires knowledge of three main variables: the specified wavelength of radiation, λ, the integer describing the order of interference, n, and the Bragg angle, θ,, which is the angle between the incident and diffracted x-ray beam. Together, the lattice interplanar spacing, D, can be directly calculated using the following equation:

$$2Dsin\theta = n * \lambda \tag{2}$$

The change in interplanar spacing, D, is indicative of axial stress development. This technique is non-destructive, obtains relatively rapid measurements, and can measure thermal strains directly. However, the shortcomings of this technique are: (i) requires a stress-free reference measurement, (ii) only a small volume near the surface is captured (Kjell and Johnson 2009), (iii) requires a clean rail surface because the system is sensitive

to oxide and corrosion on the surface layer (Ruud 1979), (iv) high instrumentation demands, and (v) relies heavily on the atomic plane distance and material properties to compute accurate stress levels.

2.1.7 Vibration Methods

Another method currently being investigated experimentally to measure rail stress is the vibration method. The basis of this technique relies on the dependence that eigenfrequencies in a beam have on the axial loading conditions. Higher frequencies develop when there exists an increase in tension in the beam. The Ultrasonic Guided Wave (UGW) technique is a vibration method that entails laterally exciting the rail at a fixed frequency, followed by measuring the wavelength of the propagating lateral bending wave (Kjell and Johnson 2009). Temperature sensors allow the system to relate measurements to the rail temperature. The Euler-Bernouli beam theory is applied to the data to obtain the longitudinal load as a function of the computed wavenumber (Weaver and Damljanovic 2005). Advantages of this technique include that it is non-destructive, the rail can exist in either tension or compression, and is not dependent on boundary conditions. Disadvantages of this technique include: (i) requires a stress-free reference wavelength measurement, (ii) requires instrumentation installation, (iii) advanced finite element calculations are necessary, and (iv) requires a very high accuracy - which can be challenging due to the lack of sensitivity and temperature drift in sensors, amplifiers, and the data acquisition system (Kjell and Johnson 2009). A newer development of this method has emerged which investigates non-linear UGW (Rizzo and Nasrollahi 2019). This technique entails inducing non-linear solitary waves along an L-shaped transducer, filled

with a chain of spherical particles, that is in point contact with the rail web (Rizzo and Nasrollahi 2019). An electromagnet is then used to generate an incident solitary wave (ISW) to release the first sphere in the chain. In response to this pulse, some of the particles acoustic energy is used to reflect a primary solitary wave (PSW), while the remaining energy deforms elastically and generates the secondary solitary waves (SSWs) (Rizzo and Nasrollahi 2019). This acoustic energy distribution depends on the elastic properties, the rail geometry in contact with the transducer, and defects that may be present between the transducer and rail interface. The axial stress is then computed as a function of the amplitude ratio of the PSW and SSWs, and the time of flight of the PSW and SSWs. Upon axial stress computation, the RNT can be estimated as the temperature at which the rail shifts from tension to compression. The advantages of this technique include that it is non-destructive, day long measurements are not required because once the equipment is installed, measurements can be recorded throughout the year, and it is highly sensitive to variations in axial stress (Rizzo and Nasrollahi 2019). The shortcomings of this technique are: (i) requires rail contact, (ii) instrumentation installation, (iii) acquired measurements must pass through the RNT, (iv) high instrumentation demands, and (v) while this technique may not be time-consuming in terms of receiving a single data acquisition, the complete RNT method requires a timely process to obtain different rail stress states.

2.1.8 Piezoelectric Method

The Electro-Mechanical Impedance technique is another non-destructive technique that uses a piezoelectric transducer (PZT). The method depends on the

relationship that exists between the electrical impedance of a PZT and the mechanical impendence of the bonded host structure (Rizzo and Nasrollahi 2019). The mechanical response of the rail to the PZT excitation is known as the Electro-Mechanical Impedance (EMI). In this technique, the PZT acts as both the actuator and receiver. The rail is first excited, subsequently, the rail produces a frequency response back to the PZT, also known as the EMI (Phillips, Zhu and Lanza di Scalea 2012). The PZT then produces an alternating electric field corresponding to the rail's EMI to indicate deformation in the structure. The EMI is a function of the rail's stiffness, mass, and damping, the PZT geometry and mass, in addition to the adhesive that bonds these two domains together (Zhu and Lanza di Scalea 2016). Advantages of this technique include that it is non-destructive, the rail can exist in either tension or compression, and has well-documented success in other applications. Disadvantages of this technique include: (i) requires rail contact, (ii) a time-consuming instrumentation installation, (iii) high instrumentation demands, and (iv) is still within experimental stages in rail application.

Table 2.1 summarizes these technologies by class, outlines the basic principles and lists the major shortcomings described above.

Table 2.1: ***Existing Method for RNT measurements***

Method	Basic Principles	Shortcomings
Rail Cutting	Cut rail to release thermal deformations for direct measurement of rail deformations.	• Time consuming • Destructive • Disruptive to train operations
Rail Lifting	Impose vertical force to unclipped rail until	• Time consuming • Semi-destructive

Rail Lifting (continued)	reaching a pre-determined distance. Vertical stiffness correlated to axial force to estimate RNT.	• Disruptive to train operations • Rail must be in tension
Deformation Measurements	Uses strain gage or extensometer data to measure rail thermal elongation to compute stress.	• Contacting • Instrumentation installation • Relies on changing dimension • Stress-free reference measurement
Ultrasonic	Velocity of propagating sound waves in a medium is correlated to the stress state in rail.	• Contacting • Stress-free reference measurement • Sensitive to material structure/defects • Assumes acoustic properties and residual stresses are constant
X-Ray	Distance between two atomic planes in a crystal is measured and related to material stresses. Change in interplanar spacing is indicative of axial stress development.	• Measures the stresses in a small volume close to the surface • Stress-free reference measurement • Distance data of the atomic planes in material at various stress states • Requires clean rail surface • High instrumentation demands
Magnetic	Electromagnetic and acoustic response signals (Barkhausen noise) produce a magnetic field. The permeability in the magnet field is correlated to the longitudinal stress.	• Time consuming calibration procedure • Reference material measurement • Eliminate local surface perturbations • High instrumentation demands • Barkhausen noise distribution depends on microstructure condition • Influenced by residual stress
Vibration	Exciting the rail to obtain vibration mode characteristics that change with the axial force.	• Contacting • Instrumentation installation • High instrumentation demands • High instrumentation accuracy • Stress-free reference measurement • Advanced FE calculations
Piezoelectric	The PZT excites the rail to obtain an EMI response signal from the rail that indicates deformation.	• Contacting • Instrumentation installation • High instrumentation demands • Within experimental stages

2.2 Non-Contacting Vision Method

The proposed concept is based on deformation patterns observed in the rail due to a naturally occurring or induced thermal loading. A stereo-vision data acquisition system coupled with three-dimensional (3D) Digital Image Correlation (DIC) technology (StereoDIC) is proposed to capture these deformations. The StereoDIC data acquisition system acquires full-field measurements of shape, curvature, deformation, and strain, in a single acquisition. This proposed technology has been routinely used in the aerospace and automotive industries and has recently been successfully implemented in quality control of pre-stressed concrete ties (Abdulqader 2017), (Rajan, et al. 2017) and (Bartelmo, et al. 2016) while shown to be effective and accurate (Bartelmo, et al. 2016). These studies have demonstrated the significant advantages that the stereo-vision system has over existing technologies since: (i) It is a non-contacting system; (ii) Captures full-field surface deformations; (iii) It acquires highly accurate measurements in the presence of both large rotations and displacements; (iv) It can be utilized for both curved and flat surfaces, and (v) It allows for a variable field of view with the utilization of different lenses. This technology has been developed over the last three decades within USC laboratories (Sutton, et al. 2008) and in other countries (Synnergren and Sjok 1999).

2.2.1 Typical System Equipment

A typical stereo-vision system used with the StereoDIC consists of a pair of cameras, lenses, commercial software VIC-Snap - Version 8 and VIC-3D - Version 7, for image acquisition and processing, respectively, a calibration target, and computer hardware, as shown in **Figure 2.1** below. This technology utilizes white light illumination

and captures images of surfaces with high contrast speckle patterns. Specimen preparation entails spray painting the region flat white to minimize reflections (polarizers can also be used to eliminate reflections if necessary), followed by manually applying the speckle pattern. Various techniques can be used to apply the patterns; they can be adhered, engraved, or projected onto a steel specimen. Additionally, cameras are mounted on an aluminum rigid bar, attached to an adjustable tripod to reach the appropriate platforms depending on the application. Furthermore, supplemental low heat emission lighting equipment is required to achieve high contrast within images.

Figure 2.1: Typical StereoDIC measurement system equipment

2.2.2 Camera and Lenses

The cameras used in this work are 9.1-megapixel FLIR-Point Grey cameras. These cameras use a Sony ICX814 imaging sensor with a physical pixel size of 3.69 µm and a camera resolution of 3376 x 2704 pixels. Attached to these cameras are two Tamron 23FM16SP 2/3" high resolution mono-focal lenses with a focal length of 16 mm. These

cameras, coupled with the lenses, are mounted on a rigid bar and positioned to achieve a desired field of view ranging between 7” - 16”. The distance between the cameras ranges between 6” - 12”. This distance is selected based on the ideal stereo angle range, 15° - 25°, to improve the accuracy of the StereoDIC measurements. The focus and aperture of the lenses are adjusted until maximizing the saturation and focus. The camera and lenses are displayed in **Figure 2.2** below.

Figure 2.2: 9.1 MP FLIR-Point Grey cameras and 16mm Tamron focal lens

2.2.3 Lighting

Lighting equipment, shown in **Figure 2.3**, is used to ensure adequate illumination for high contrast within images. This testing procedure employs two Bi-color 500 Ultra Bright Dimmable LED Studio Light Panel – 9M-01LED009-500-07. Due to the focus of this study on temperature, it is imperative to have low heat emission lighting to minimize any additional external heat sources. The LED lights are powered by direct current to ensure a constant light source that doesn’t vary with power supply. The lights are either mounted on platforms or portable supports to properly illuminate the field of view. The LED source includes four attached, movable reflectors (see **Figure 2.3**) that are also utilized to maximize illumination of the region of interest. Platforms are placed on either side of the

tripod and tilted towards the specimen. The mount that the lighting equipment rests on should not be at the same height as the camera system to minimize undesirable reflections. Reflections generally result in saturation of the pixel intensity levels, resulting in increased error in the StereoDIC measurements within the reflection-saturated image region.

Figure 2.3: LED light panels that supplement the StereoDIC system

2.2.4 Calibration Target

StereoDIC calibration is used to compute the intrinsic and extrinsic parameters to eliminate measurement bias and triangulate the field of view with the cameras (Correlated Solutions, Inc. 2019). The calibration target is selected based on the area of interest. Ideally, it should cover at least 1/3 of the field of view. In this study, the field of view dimensions are consistently 7”- 16”, so a 4” x 5” calibration target, pictured in **Figure 2.4**, is selected for all tests conducted. This target contains a 12 x 9 grid of black dots in the x and y, respectively, on a rigid white plate. All dots are equally spaced 5mm apart.

There are three donut-shaped orientation dots that are used to define the coordinate system.

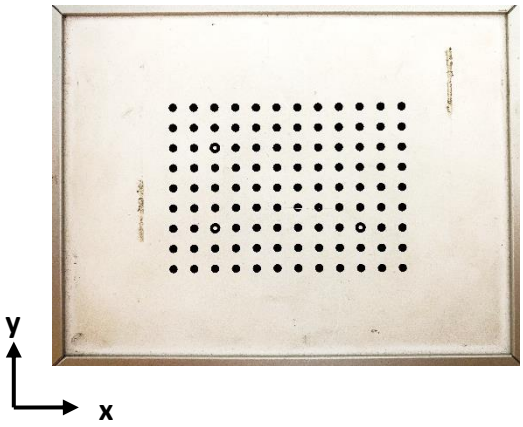

Figure 2.4: Target used for StereoDIC system calibration

2.2.5 Pattern Application

The speckle pattern may be applied in different ways to a specimen's surface. In this case, an ultra-fine point water resistant permanent black marker is used to manually generate a speckle pattern with a dot size of approximately 0.5 mm. To obtain accurate measurements with the StereoDIC system, not only is it imperative to apply a high contrast pattern, but the appropriate dot size must also be selected. An appropriate dot size should be captured by a minimum of 3 x 3 pixels on the digital image (Schreier, Orteu and Sutton 2009). This oversampling process is recommended to ensure that the StereoDIC measurements are unbiased and accurate. The dot size is a function of the field of view and the resolution of the cameras. With a 3376 x 2704-pixel resolution and a maximum field of view dimensions ranging between 7" - 16", the minimum dot size can be computed. Dividing the smaller resolution, 2704 pixels, and the higher field of view, 16", it can be determined that a captured image has a minimum of 169 pixels/in.

Therefore, a 3 x 3-pixel dot must be at least a minimum of 0.0178” (0.45 mm) in dimensions. Thus, the 0.5 mm selected dot size is appropriate. Additionally, to prevent oversaturation, the contrast histogram in VIC 3D – Version 8 software should show consistent values of gray levels in the range of 20 - 220 on a scale of 0 - 255.

2.2.6 Image Acquisition

The image acquisition process begins with the acquisition of calibration images, followed by the acquisition of speckle images. Initially, the cameras are turned on to allow them to reach a steady temperature state prior to capturing images. The cameras must be properly connected via a USB 3.0 hub so that the system is time synchronized. Upon setup completion, the calibration images are taken using the calibration target shown in **Figure 2.4**. This process entails capturing approximately 50 images while manually rotating and translating the target within the field of view. The target and specimen are located within the depth of field for the lens-camera combinations used in the stereo-vision system to ensure complete dot extraction throughout the calibration process. During calibration, a 2^{nd} order radial distortion correction algorithm is selected to limit any lens distortion errors. These calibration images are then uploaded into the VIC-3D – Version 8 software to assess the calibration. After achieving a successful calibration score of less than 0.1, the initial speckle images are captured prior to the specimen being heated. These initial images can be used to represent the reference image, prior to thermally loading, that all subsequent images may be compared to, but it is noted that any speckle image at any thermal loading could be used as the reference image. All data sets captured after the initial speckle image represent a thermal loading step. A total of

50 images are captured per data set and images are averaged for each camera through a MATLAB code. These images are processed for analysis in VIC-3D – Version 8.

2.2.7 Image Analysis and Deformation Measurements

Following image acquisition after the final thermal loading step, VIC-3D – Version 8 is then used for image correlation and processing. As is typical of modern CMOS and CCD cameras, the FLIR-Point Gray cameras employed in this thesis have a Gaussian distribution with variability in pixel intensity. This creates a standard deviation of ± 1 gray level of the total available 255 gray levels that may introduce a ± 0.02-pixel error for any low contrast deformation images captured throughout the thermal cycle (Abdulqader 2017). Depending on the imposed rail boundary conditions and the subjected rail temperature change, the developed strains may be under 200 $\mu\varepsilon$. It is therefore imperative to minimize the level of variability that exists in these measurements. Because variability in the recorded pixel-level intensity values has a Gaussian distribution, the images captured in a single thermal load set are averaged to decrease the noise that exists in the measurements. In this thesis, 50 images are captured, and the images are averaged for each camera per thermal load set using a MATLAB code. By averaging the images, the assumption is made that there is negligible motion occurring during the image acquisition of a single load set. The noise associated with pixel intensity can be quantified by uploading all 50 images in a single load set and setting one as the reference image. The level of variability in deformation measurements per load set can then be seen between images. By capturing 50 images per load set, it is found that this source of noise can be significantly reduced. Because of heat propagation throughout the rail during a thermal

loading, motion may actually be occurring throughout a loading set. For this reason, perhaps the function in VIC-3D – Version 8 that averages the measurements based on the pixel intensity in the images may be a better approach at minimizing noise. Additional sources of noise may exist due to other experimental factors, but additional measures are taken to minimize these:

1. The cameras are mounted on a rigid aluminum bar. This aluminum bar is attached to a tripod that has rubberized compression mounts to isolate any background vibrations from the laboratory test.
2. During experimental setup, the initial step includes turning the cameras on to allow time for them to reach a steady state temperature, prior to calibration procedures. Due to the heating procedures inherent in these laboratory tests, it is important to minimize any variations in camera temperature.
3. The 2nd order radial distortion correction algorithm is applied to the calibration to account for lens distortion errors.
4. Low heat emission lighting equipment is selected to minimize any external heat sources exposed to the specimen and cameras.

Chapter 3. RNT Measurement Method Development

This chapter discusses the fundamentals in the development of the proposed RNT and stress measurement method. The hypotheses of the method are discussed and verified qualitatively through preliminary computer simulations. Subsequently, experimental testing, coupled with finite element computer simulations, validate and verify the hypotheses presented. Upon validation and verification, the development of the proposed measurement methodology is presented.

3.1 Hypotheses

Using the schematic of a rail with the corresponding coordinate system shown in **Figure 3.1**, development of the RNT and stress measurement system is based on two main hypotheses:

(i) Thermal loads will induce nonuniform expansion over the rail head in the transverse direction, y, due to constraints imposed by the boundary conditions located at the anchoring points and due to the continuity of the rail in the longitudinal direction, x, and

(ii) The transverse direction, y, of the web at a location between two consecutive ties remains stress-free, while significant transverse strain, ε_y, exists and

directly depends on temperature change. In opposition, the thermal stress in the longitudinal direction is significant and depends directly on the level of constraint and temperature change, while the longitudinal strain, ε_x, is considered negligible.

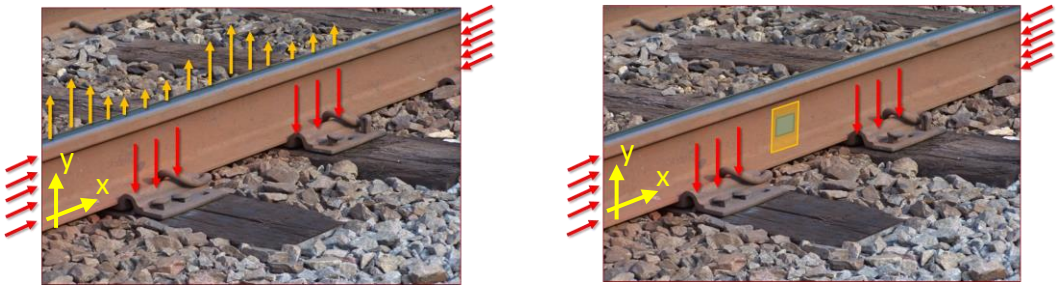

(a) **(b)**

Figure 3.1: Hypotheses schematics: (a) Constraints located at the ties and due to continuity of CWR (red arrows) cause flexure-like deformations (yellow arrows); (b) Due to the same constraints, ε_x is negligible compared to ε_y at the center of the web between ties (yellow square)

3.2 Qualitative Investigation through Computer Simulations

The two hypotheses are first verified qualitatively through a preliminary computer simulation study in order to formulate the RNT measurement concept. To this end, a single segment of rail is modeled using Finite Element analysis with commercially available Abaqus/Standard software. The Finite Element (FE) method is a numerical technique that simulates a physical phenomenon to obtain approximate solutions. The FE geometric model, shown in **Figure 3.2(a)**, consists of a 132 RE rail cross section extruded to a length of 15'. The 132 RE rail cross section is an industry standard rail cross section defined by the American Railway Engineering and Maintenance-of-Way Association (AREMA). The 132 number defines the mass density (lb/yd) of the cross section and the RE denotes that the section geometry was defined by AREMA. The rail is constrained

longitudinally at the end faces and rigidly attached to the ties at the rail seats. In addition, the stiffness of the tie and track are ignored. The rail is initially undisturbed and stress free, defined at an initial rail temperature of 0^oF, representing the rail at its RNT state. The rail is subjected to uniform temperature changes in the range of $\Delta T = \pm 100^oF$ above and below the RNT. The deformed configurations for the two cases are shown in **Figure 3.2(b)**. The computed deformations are in the range of 150-1,000 microns and are well above the lower limit of accuracy of the StereoDIC system used in this work. The non-uniform deformations in the rail are clearly visible in both configurations. The curvature changes are evident in **Figure 3.2(b),** both at the top of the rail head and the base of the rail and always in the immediate region of the ties. It is observed that:

(i) The curvature changes proportionally with the temperature variation and

(ii) The curvature changes sign as the temperature in the rail shifts from above to below its RNT.

Furthermore, the strain and stress values are in reference to an element located at point A on the web between consecutive ties shown in **Figure 3.2(c)**, which are representative of only the order of magnitude. Computed strains are in the range of 250 - 1,000 $\mu\varepsilon$ and are well above the lower limit of accuracy of the StereoDIC system used in this work. Under the assumed conditions of perfect constraints, it is observed that:

(i) The longitudinal strain, ε_x, is negligible while the corresponding stress, σ_x, is significant and proportional to the temperature change and

(ii) The transverse strain, ε_y, is significant and proportional to the temperature change, while the corresponding stress, σ_y, is negligible.

This analysis verifies the assumption that the imposed constraints induce curvature changes between two successive ties or about the anchoring points under thermal loads. Moreover, the transverse direction remains unconstrained and stress-free throughout temperature fluctuations. With the proposed hypotheses qualitatively verified, experimental procedures are then carried out to quantitatively validate and verify these hypotheses, as discussed in the next section.

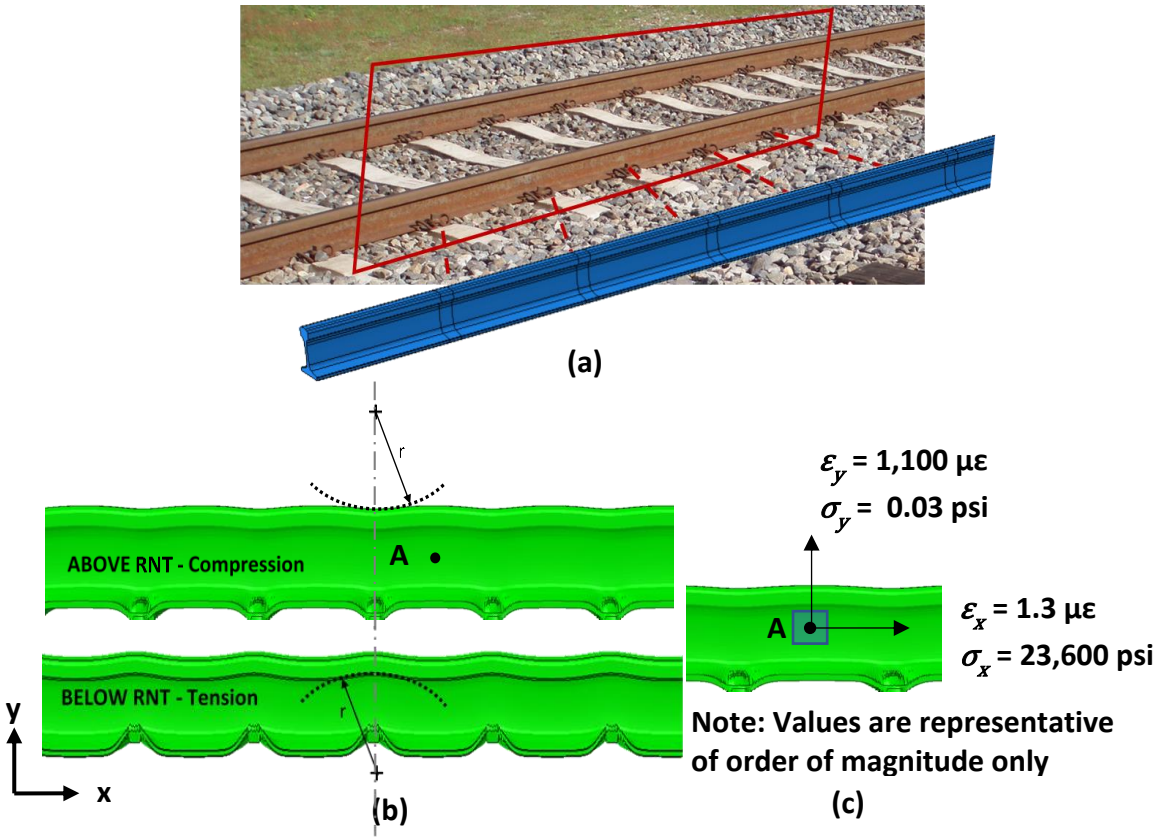

Figure 3.2: Hypotheses verification: (a) Physical rail and corresponding FE geometric model; (b) Deformed configurations of rail subjected to temperatures 100°F above (uniform scale deformation factor: 10^3) and 100°F below the RNT (uniform scale deformation factor: 10^2 and additional Y coordinate scaling: 5); (c) Strain and stress values for the longitudinal, x, and transverse, y, direction at point A

3.3 Validation and Verification through Experimental and Analytical Studies

This section verifies that the expected deformations can be measured using the StereoDIC technology. To this end, two rail segments are considered for experimental testing. The first rail segment is a 12-inch physical segment of a free-standing 132 RE rail, shown in **Figure 3.3(a)** and is considered fully unconstrained. The second segment is a 16-inch physical segment of 132 RE rail, shown in **Figure 3.3(b)**, and is considered only partially constrained due to imperfections in the fabricated configuration. It is noted that the difference in rail length is not intentional but were the provided segments for laboratory testing. However, the length of the unconstrained segment is not expected to impact the deformations and strains incurred due to thermal loads. To constrain the longitudinal movement, steel plates with stiffeners at either side of the rail are welded to a bottom base plate beneath the rail. Two additional plates of shorter width are welded to the top of each side plate, leaving a 3-inch gap for rail head exposure, as depicted in **Figure 3.3(c)**. The ends of the rail segment are welded to these plates, leaving a 1-inch gap between the rail base and the steel base plate to foster vertical deformations. Schematics are shown in **Figure 3.3(d)** and **Figure 3.3(e)** to visualize the welded configuration with corresponding dimensions to depict the side view of the rail web region and the plan view of the rail head. Due to imperfections in the fabrication of this configuration, as well as the fact that the constraining parts will eventually heat up during testing, the rail is considered only partially constrained. Experimental measurements obtained using the StereoDIC technology are used to validate FE thermoelastic computer using software Abaqus. Details of the models are presented in the following sections.

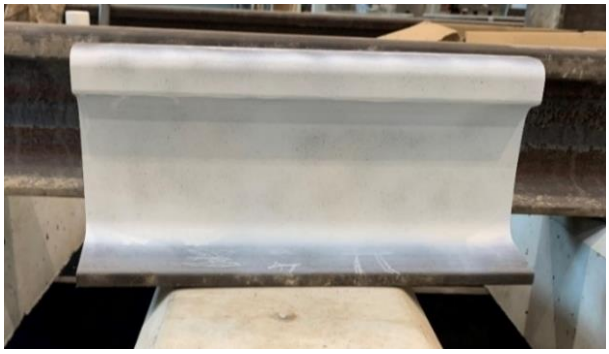

(a)

(b)

(c)

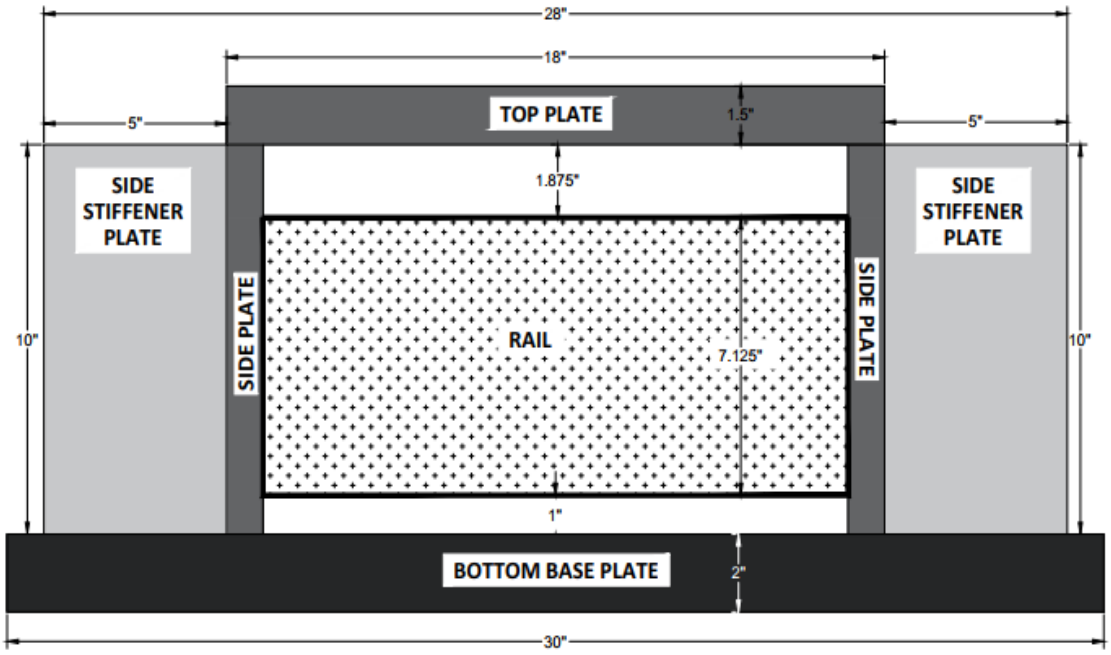
28"
18"
5"
TOP PLATE
1.5"
5"
1.875"
SIDE STIFFENER PLATE
SIDE STIFFENER PLATE
SIDE PLATE
SIDE PLATE
RAIL
7.125"
10"
10"
1"
BOTTOM BASE PLATE
2"
30"

(d)

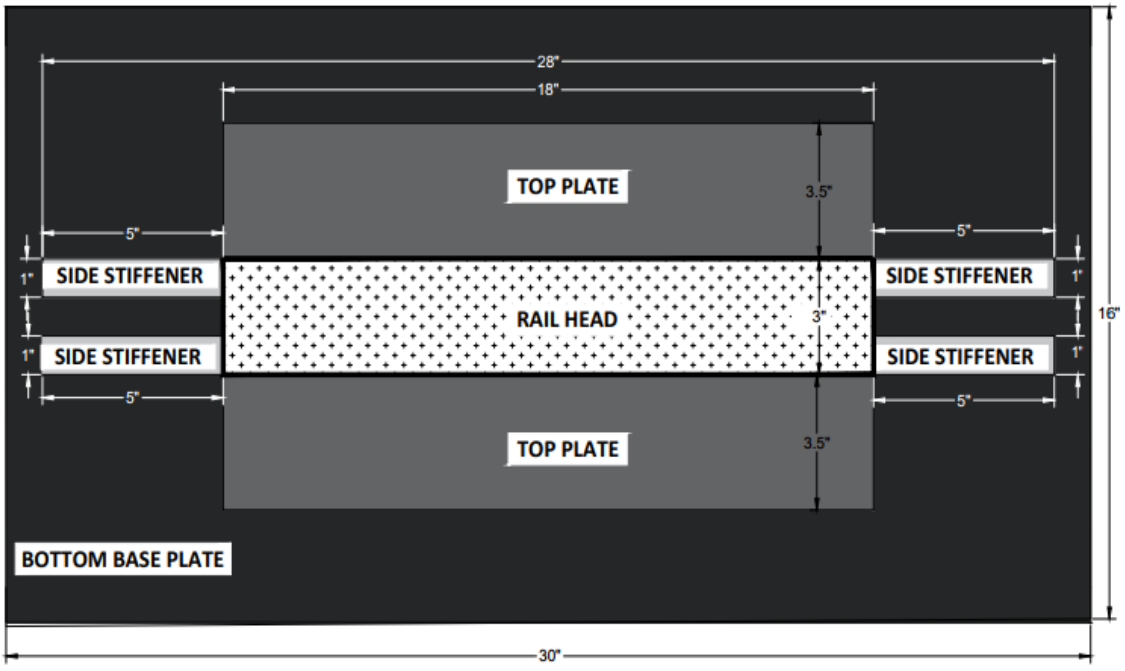

(e)

Figure 3.3*: *Experimental testing specimens: (a) 12-inch unconstrained specimen; (b) 16-inch partially constrained specimen – side view of the rail web; (c) 16-inch partially constrained specimen – plan view of the rail head; (d) Schematic of the side view of partially constrained specimen; (e) Schematic of the plan view of partially constrained specimen

3.3.1 Strain Field on Web

This section presents the implementation of the StereoDIC system for laboratory experimentation performed on the rail web to obtain the strain fields of the specimens. The rail webs for both specimens are manually patterned with the 0.5 mm dot size discussed in section **2.2.5**. The first laboratory test is conducted on the unconstrained specimen (see **Figure 3.3(a)**). The specimen is thermally loaded, and images are captured as the rail is cooling down. Following this, the partially constrained specimen (see **Figure 3.3(b)**) is thermally loaded, and images are captured as the rail is heating up and cooling down. The rail web temperature is recorded by employing a UEI INF165C 12:1 Infrared

(IR) Thermometer. This IR thermometer uses circular laser targeting to capture the maximum temperature in a region and is accurate to ± 4°F. The rail web temperature which defines each thermal load step is in respect to the rail web center point. It is noted that an IR thermometer is used to determine the temperature at various locations along the web. The temperatures that define each data sets solely reflect the temperature at the web center point, but temperatures throughout the entire rail web region vary from this temperature throughout testing procedures. The measurements obtained using StereoDIC are verified analytically through the theoretical value of strain and numerically through FE computer simulations that are described throughout the section.

3.3.1.1 Unconstrained Rail

Experimental testing is initially performed on the 12-inch unconstrained rail specimen. This data is used as validation for the FE computer model predictions.

StereoDIC Measurements

The 12-inch specimen is acclimated at room temperature, 83°F, when initial reference images are taken after StereoDIC calibration. The specimen is then heated to approximately 240°F using an acetylene torch along the back side of the rail web. The heat source is maintained until reaching slightly above this predetermined temperature, and to allow the heat to begin uniformly distributing throughout the specimen, prior to capturing measurements. Using the StereoDIC system, strain measurements are captured as the specimen returns to room temperature at approximately every 30°F temperature decrement. The induced thermal cycle led to StereoDIC strain measurements shown in **Figure 3.4** of the rail specimen. The strain fields are superimposed and averaged over a

2” x 2” square in the center region of the rail web, shown in **Figure 3.4(a)**. As shown in **Figure 3.4(b)** and **Figure 3.4(c)**, at a rail web temperature of 180°F (ΔT= +97°F), values are similar in deformation magnitude and shape for both directions of strain. This indicates that the rail is expanding at the same rate in all directions.

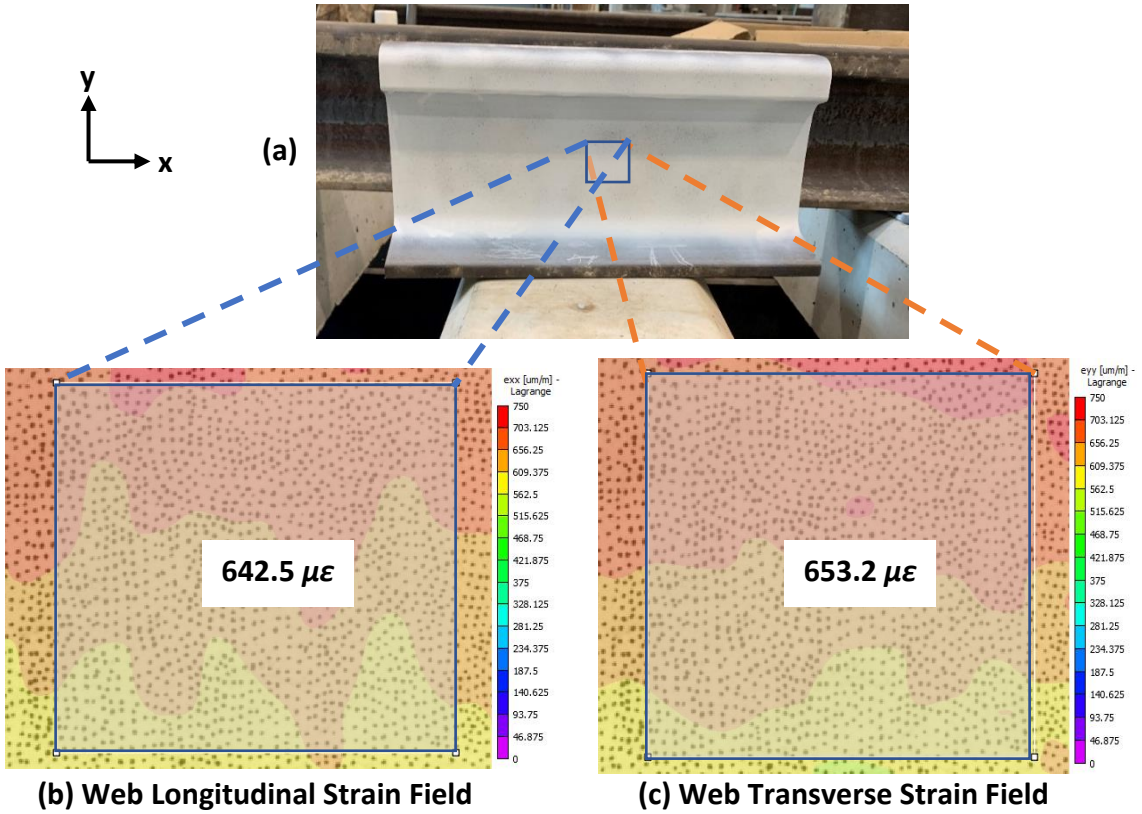

(b) Web Longitudinal Strain Field **(c) Web Transverse Strain Field**

Figure 3.4: Unconstrained rail strain fields superimposed on the face of the web with average values when heated 97°F above room temperature: (a) Strain is averaged over the square; (b) Color map of the longitudinal strain, ε_x, field; (c) Color map of the transverse strain, ε_y, field

Finite Element (FE) Solutions

The experimental findings are used to validate the developed FE model numerical predictions for the unconstrained rail case. This model is comprised of only one domain, a rail segment, defined as a 3D deformable solid formed by extruding a 132 RE rail cross

section to a length of 16”. The rail is meshed with 29,707 hexahedral-dominated reduced integration elements. This is comprised of 25,440 linear hexahedral elements (C3D6RT) and 1,260 linear wedge elements (C3D6T). **Figure 3.5** shows the FE geometry and mesh of the rail segment. This hexahedral dominated mesh is selected to accurately capture and mesh the irregular rail cross section. The longitudinal and transverse strain as a function of temperature are extracted from element A located in the center of the rail web, as shown **Figure 3.5**. This element is located at the centroidal height of a 132 RE rail section, 3.2” from the bottom of the rail segment, and at mid-length of the 12” specimen, 6” from one rail end. A thermoelastic analysis is performed on the rail segment which requires both mechanical and thermal properties to be defined. Typical steel material properties are selected and defined in **Table 3.1**. These material properties are used for all models in this section.

Table 3.1: Steel material properties defined in FE models

	Property	**Value**
Steel	Modulus of Elasticity (psi)	29×10^{6}
	Poisson Ratio	0.3
	Thermal Expansion Coefficient (in/in/°F)	6.7×10^{-6}
	Specific Heat (Btu/(lb-°F))	0.122
	Conductivity (Btu/s*°F*in)	7.18×10^{-4}
	Density ($lbf*s^2/in^4$)	730×10^{-6}

The rail ends remain free to allow the rail to expand longitudinally. Heat is applied to the outer surface of the rail by a surface heat flux. Through trial and error, different heat flux values are input until reaching a temperature change that matches the recorded testing temperature change. A more in-depth description of the model type can be found in **Chapter 4**.

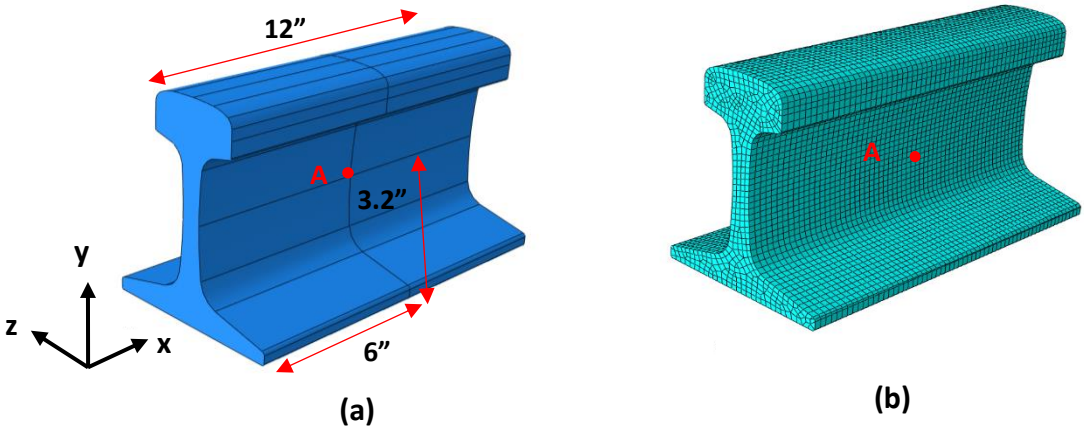

Figure 3.5: FE unconstrained rail depicting element A where strain measurements are extracted: (a) Rail geometry with corresponding dimensions; (b) Rail mesh

Figure 3.6(a) and **Figure 3.6(b)** show the longitudinal and transverse strain at the rail web in respect to temperature change. Linear regression is applied to the StereoDIC measurements to describe the linear relationship between strain and temperature. The StereoDIC and FE strain results increase linearly and at approximately the same rate. Results indicate that the thermal strain predictions obtained from the numerical model used in this work are in agreement with the StereoDIC experimental measurements.

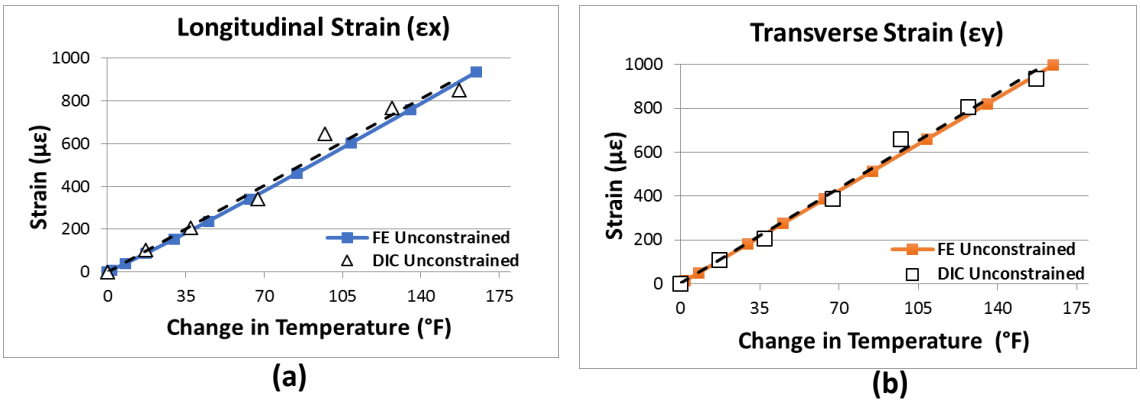

Figure 3.6: Plots comparing the unconstrained rail numerical results to the StereoDIC measurements with respect to temperature change at the center web: (a) Longitudinal strain, ε_x; (b) Transverse strain, ε_y

3.3.1.2 Partially Constrained Rail

Experimental testing is then performed on the 16-inch partially constrained rail specimen. This data is used as validation for the FE computer model predictions.

StereoDIC Measurements

A similar testing procedure is performed for the partially constrained rail specimen. The 16-inch specimen is acclimated at room temperature, 77°F, and then heated to approximately 240°F using an acetylene torch along the back side of the rail. In this testing procedure, measurements are captured every 20-30°F increase in temperature at the rail web center point. The heat source is maintained until reaching the next temperature increment, and then subsequently removed. After measurements are captured, the heat source is then reapplied to the back side of the rail until reaching the next temperature increment. Upon reaching 240°F, the heat source is permanently removed, and strain measurements are captured in 20°F decrements as the specimen cools down until returning to room temperature. As the rail cools down, the rail temperature is more uniformly distributed within the specimen. **Figure 3.7** shows the strain field measurements superimposed across the middle section of the web for the partially constrained rail at a rail temperature of 230^{o}F (ΔT=+153^{o}F). The transverse and longitudinal components are averaged over the 2” x 2” square shown in **Figure 3.7(a**). The color maps of the longitudinal and transverse strain are superimposed on the face of the web and shown in **Figure 3.7(b)** and **Figure 3.7(c)**, respectively, along with the averaged values.

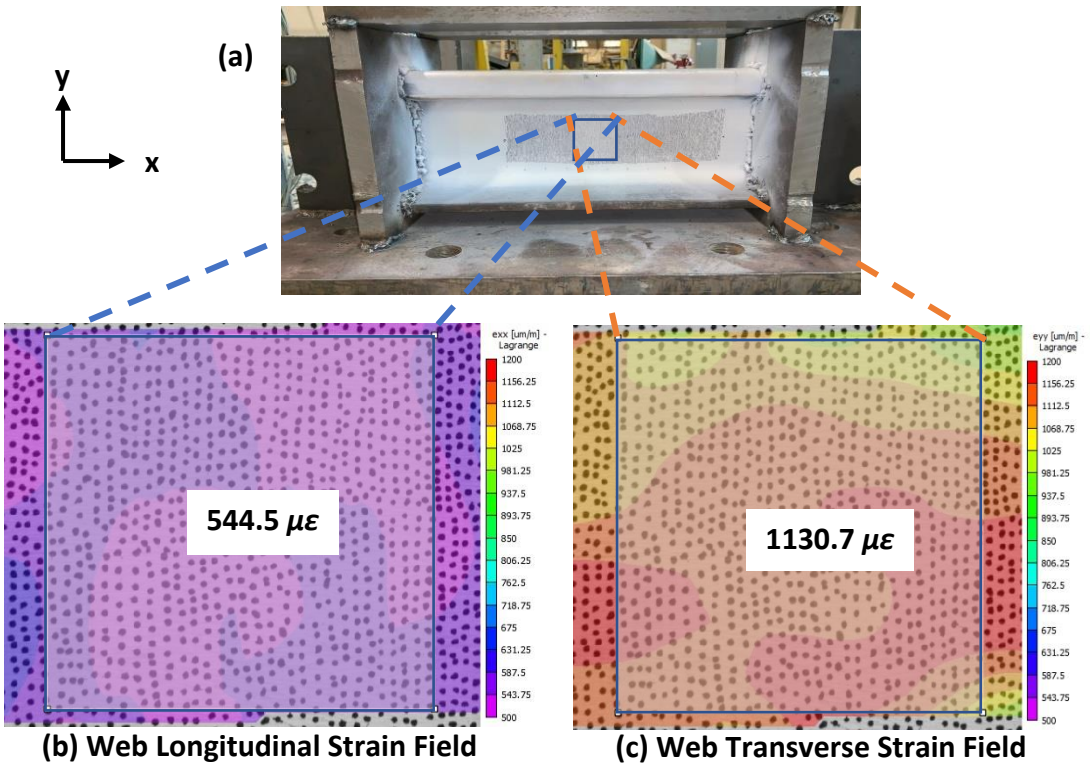

Figure 3.7: Partially constrained rail strain fields superimposed on the face of the web with average values when heated 153°F above room temperature: (a) Strain is averaged over the square; (b) Color map of the longitudinal strain, ε_x, field; (c) Color map of the transverse strain, ε_y, field

Figure 3.8(a) and **Figure 3.8(b)** display the StereoDIC captured longitudinal strain, ε_x, and transverse strain, ε_y, in respect to change in temperature for the heating and cooling processes. Linear regression is applied to the StereoDIC measurements to describe the linear relationship between strain and temperature. **Figure 3.8(a)** plots the measurements as the specimen is heating up in respect to the reference image that represents the rail at room temperature, T = 77°F. **Figure 3.8(b)** plots the measurements as the specimen is cooling down in respect to the reference image that represents the maximum temperature loading, T = 240°F. It is observed that the measurements captured during the heating and cooling of the rail are approximately symmetric. It is shown that

the longitudinal and transverse strain are increasing/decreasing at different rates. If the rail specimen was fully constrained longitudinally, the expected longitudinal strain would be zero. In contrast, the unconstrained rail strains increase linearly at approximately the same rate for both directions of strain. Therefore, the partially constrained specimen longitudinal expansion is clearly restrained by the welded supports, but not to the extent that the specimen is considered fully constrained axially. It is concluded that transversely this rail can still expand freely, however, longitudinally, the rail specimen is limited by the level of constraint that exists at the rail ends.

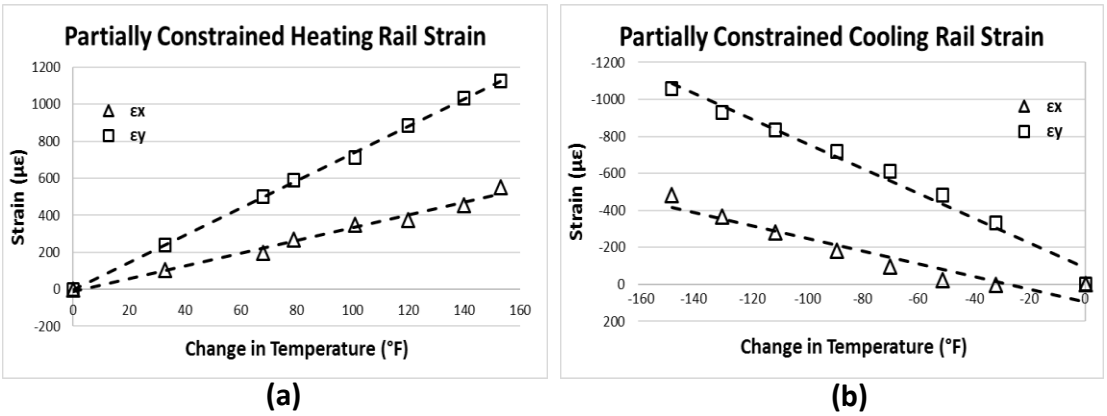

Figure 3.8: Plots of the partially constrained rail thermal strain rates with respect to temperature change for the longitudinal, ε_x, and transverse, ε_y, strain captured by the StereoDIC: (a) Thermal strains as the rail is heating up; (b) Thermal strains as the rail is cooling down

Finite Element (FE) Solutions

The experimental findings are used to validate the developed FE model numerical predictions for the partially constrained rail case. This model is comprised of only one domain, a rail segment, defined as a 3D deformable solid formed by extruding a 132 RE rail cross section to a length of 16”. The rail is meshed with 35,440 hexahedral-dominated

reduced integration elements. This is comprised of 34,080 linear hexahedral elements (C3D6RT) and 1,360 linear wedge elements (C3D6T). **Figure 3.9(a)** and **Figure 3.9(b)** show the geometry and mesh of the rail segment. This hexahedral dominated mesh is selected to accurately capture and mesh the irregular rail cross section. A thermoelastic analysis is performed on the rail segment which requires both mechanical and thermal properties to be defined. The steel properties given for the previous FE analysis in **Table 3.1** are also used for this simulation. Heat is applied to the outer surface of the rail by a surface heat flux. Through trial and error, different heat flux values are input until reaching a temperature change that matches the recorded testing temperature change. A more in-depth description of the model type can be found in **Chapter 4**.

Two model cases are developed to investigate the effect that the boundary conditions defined at the rail ends have on the strain, specifically the level of longitudinal constraint. Due to imperfections in the welded supports of the experimental specimen, the level of constraint is unknown. To confirm the assumption that the rail specimen is only partially constrained, the two extreme boundary conditions are defined for FE analysis. Initially, the rail is fully constrained longitudinally at the rail ends, allowing deformations in all other directions. Subsequently, this constraint is removed, and the rail is free to deform in all directions. In both cases, the rotations are constrained at the rail ends. The longitudinal and transverse strain in respect to temperature are extracted from element B located in the center of the rail web, as shown **Figure 3.9**. This element is located at the centroidal height of a 132 RE rail section, 3.2” from the bottom of the rail, and at mid-length of the 16” specimen, 8” from one rail end.

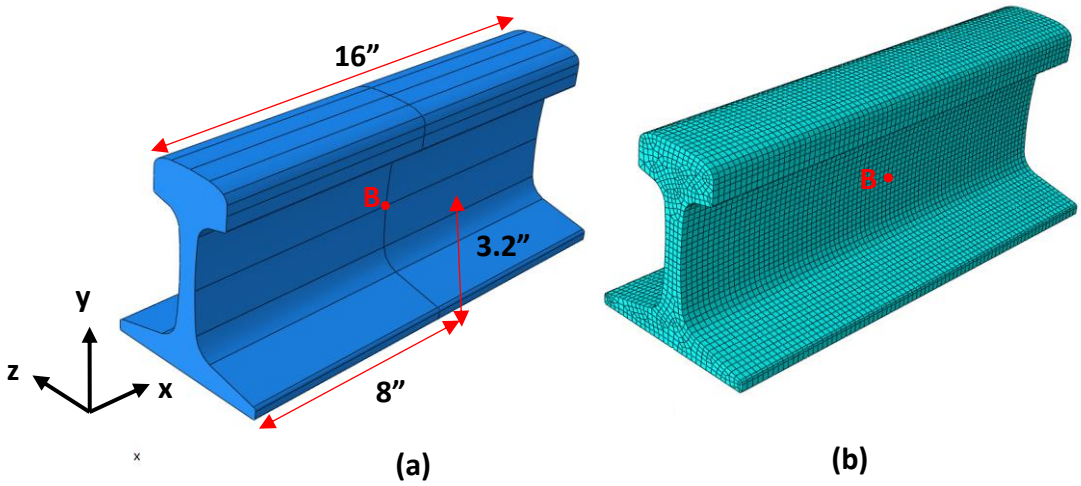

Figure 3.9: FE rail depicting element B where strain measurements are extracted: (a) Rail geometry with corresponding dimensions; (b) Rail mesh

Figure 3.10(a) and **Figure 3.10(b)** plot the longitudinal strain, ε_x, and transverse strain, ε_y, of the FE fully constrained and unconstrained rail solutions against the StereoDIC measurement results for the partially constrained rail specimen. As expected, the StereoDIC measurements for the partially constrained rail are bounded by the two FE solutions, which represent the upper and lower strain limits. Specifically, the fully longitudinally constrained FE rail and the unconstrained FE rail results bound the partially constrained rail specimen measurements for both directions of strain. Due to the eccentric thermal loading and imperfect weld boundary conditions, it appears that the StereoDIC partially constrained measurements tend to more closely follow the unconstrained FE case. Another factor tending to favor the unconstrained configuration is that the supports are inevitably heated throughout the heating procedure. This allows the supports to expand simultaneously, much like the specimen, reducing the level of longitudinal constraint on the rail.

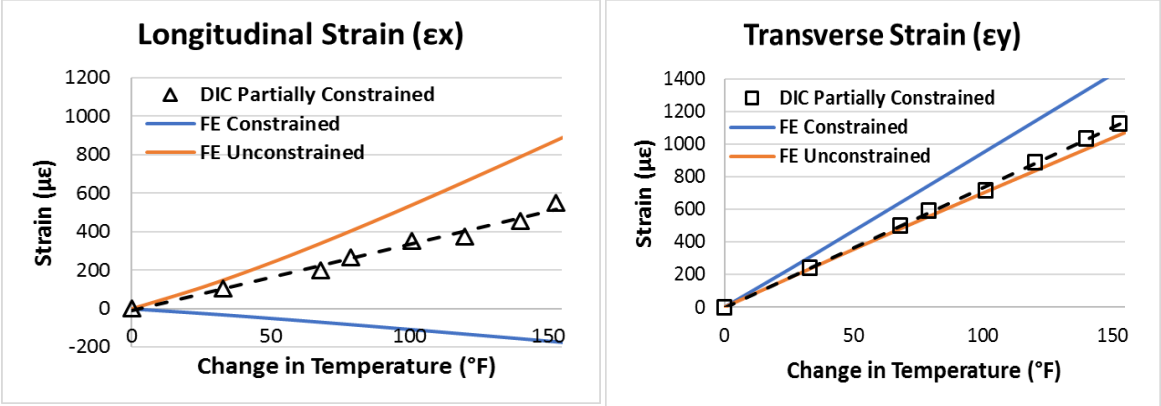

(a) (b)

Figure 3.10: Plots comparing the FE numerical results for the constrained and unconstrained support cases to the StereoDIC system measurements of the partially constrained rail with respect to temperature change at the center web: (a) Longitudinal strain, ε_x (b) Transverse strain, ε_y

To further verify the hypothesis that the rail is always free to deform transversely at the rail web, transverse strain measurements are plotted with the theoretical computation of strain. **Figure 3.11** displays the StereoDIC captured transverse strain measurements of the unconstrained rail and the partially constrained rail throughout the cooling process, compared to the theoretical computation of strain in respect to temperature change. The theoretical value of strain is calculated as a function of the thermal expansion coefficient and change in temperature. This relationship describes the linear thermal behavior as an object freely deforms.

$$\varepsilon = \alpha * \Delta T \tag{3}$$

A coefficient of thermal expansion for steel material is selected, α = 6.7*10^{-6}, and strain is determined using Equation (3) for each change in temperature increment. **Figure 3.11** displays the StereoDIC measurements for the unconstrained and partially constrained rail specimens increasing at approximately the same rate as the theoretical value of strain.

The slight differences could be a result of the coefficient of thermal expansion chosen and/or the non-uniform temperature distributions throughout the rail specimens.

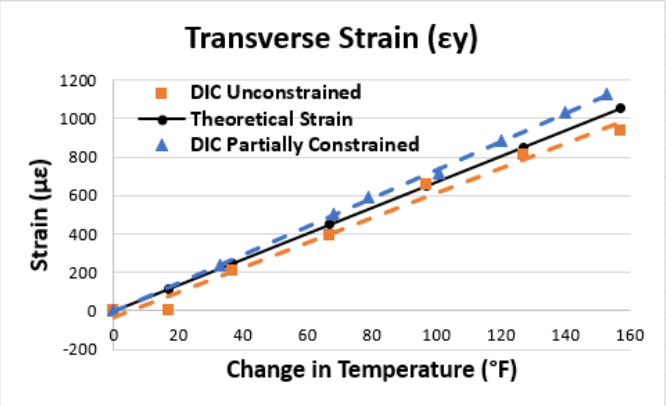

Figure 3.11: Plot of StereoDIC captured transverse strain measurements compared to the theoretical value of strain

3.3.2 Strain Testing Assessment

It is concluded that the transverse strain increases linearly with temperature in the center region of the rail web for all varying support conditions. The agreement between StereoDIC measurements, theoretical predictions, and numerical model values confirms that the specimen is essentially unrestrained in the direction transverse to the axial constraints imposed on the rail specimen. In contrast, the longitudinal strain is directly affected by the level of longitudinal constraint. Because the actual level of constraint imposed by the welded supports is unknown, StereoDIC measurements confirm that neither full constraint nor fully unconstrained boundary conditions can be used with FE modeling to predict the actual deformations. All results appear to agree with the FE solutions. However, in practice, various sources could affect the relationship

between model predictions and the StereoDIC measurements. A partial listing is given below.

- The heating source that is used for the experimental investigation does not heat the rail uniformly. This non-uniform heat distribution may lead to variation of temperatures in the web. Therefore, temperature measurements at the center point on the web are only an indication of the actual rail temperature. For such cases, the temperature field needs to be captured in subsequent work by a full-field infrared scanner.
- The temperature measurements are synchronized manually with the image acquisitions at each temperature. The temperature may vary between the first and last image acquisition at a single temperature. This is particularly true when measurements are taken in the heating phase of the test. Consequently, some level of error should probably be expected.
- While the constraining plates and welds are not directly exposed to heat, they will eventually experience some temperature increase since they are not thermally isolated from the rail specimen. This may lead to minor expansions of the supports which could, in turn, affect the level of constraint they provide to the rail.
- When comparing the FE model simulations to StereoDIC measurements, typical steel material values are assumed for the rail, whereas, the actual material properties are unknown and should be experimentally determined in future tests.

Despite the experimental differences that may have existed throughout laboratory experimentation, the StereoDIC measurements are in good agreement with the FE predictions. These tests serve as a verification and validation of the hypotheses on which the method is developed.

3.3.3 Deformation Field on Rail Head

This section presents the implementation of the StereoDIC system for initial laboratory experimentation, performed on the top of the rail head to obtain the deformation fields and shape functions for the partially constrained specimen. The rail head is manually patterned with the 0.5 mm dot size discussed in section **2.2.5**. The partially constrained specimen is thermally loaded, and measurements are captured as the rail is heating up and cooling down. The IR thermometer is used to obtain the rail head temperature which defines each thermal load step is in respect to the rail head center point. It is noted that an IR thermometer is used to determine the temperature at various locations along the rail head, but the temperature that defines each data sets solely reflect the temperature at the rail head center point. The steel supports which constrain this specimen were welded to the rail at approximately room temperature, 70°F. Therefore, while the actual RNT is unknown, it is assumed that the RNT of specimen should be approximately 70°F. These measurements are verified numerically through a FE computer simulation described in this section.

StereoDIC Measurements

The curvature observations are now quantitatively investigated with the StereoDIC system utilizing the partially constrained rail specimen. The area of interest for

this experiment is the rail head. The specimen is placed on its side, with supports engaged, so that the StereoDIC system could align along the same plane as the rail head. The adjusted setup rotates the coordinate system used in the previous testing (see in **Figure 3.12**). The 16-inch specimen is acclimated at room temperature, 71°F, when initial images are taken. Subsequently, the rail is heated to approximately 200°F using an acetylene torch along the web of the rail. In this testing procedure, the measurements are captured at 20°F temperature increments and decrements at the center point of the rail head, 8" from one end. **Figure 3.12(a)** show the out of plane deformation field, V, superimposed across the entire rail head of the partially constrained specimen as the rail is heated to a temperature of 180^{o}F (ΔT=+109^{o}F), as shown in **Figure 3.12(b)**. The V-deformation field is the displacement in the out-of-plane direction, y, defined by the coordinate system. This is selected because when the rail is set up correctly, the vertical deformation is desired, which is equivalent to the V based on the rotated coordinate system. The displacement profiles are extracted across the red line along the rail head in respect to the x position, as shown in **Figure 3.12**, relative to the center point of the rail head.

The displacement profiles are extracted by the inspector line tool from the software and are plotted for each temperature increment. A quadratic trendline is drawn through the data points to capture the average behavior. **Figure 3.13** plot the displacement with respect to the reference image taken at room temperature, T=71°F, along the inspector line throughout the heating and cooling processes of the specimen. The displacement profiles are changes in deformations due to temperature change in respect to the assumed initial undeformed shape of zero at room temperature. As the rail

temperature increases from its initial temperature to the maximum temperature, 200°F, there is an increase in the deformations, as shown in **Figure 3.13(a)**. This depicts the swelling effect of the top of the rail due to non-uniform thermal expansion. In contrast, **Figure 3.13(b)** shows that the deformations decrease as the rail temperature returns to room temperature. This depicts the shrinking effect of the rail head due to thermal contraction. While displacement increases and decreases as expected with temperature change, there are some discrepancies with the magnitude of displacement between the heating up process and the cooling down process. The heat distribution is more uniform as the specimen cools down and the rail temperature prior to measurement acquisition has a greater difference upon completion of measurement acquisition. While this test lacks synchronized temperature-displacement measurements, qualitatively this test confirms that StereoDIC implemented within the VIC-3D can accurately capture displacements as the specimen swells and shrink.

Following analysis of the displacement profiles, measurements captured during the cooling down process are individually set as the reference image in the processing software to obtain the absolute shape at each rail temperature. The y coordinate of each reference image over a -70 mm to +70 mm x-position range, relative to the center of the rail head, is extracted to obtain these unique shapes, as displayed in **Figure 3.14**. A quadratic trendline curve fits each of the shape profile to obtain an equation that describes the average behavior. **Figure 3.14(a)** displays the shape profiles at a rail temperature of 100°F along with its corresponding quadratic equation that will be used to exemplify how the curvature will be computed. **Figure 3.14(b)** plots the remaining

shape profiles prior to curve fitting, to display the irregular top of rail shape that exists throughout the thermal loading. **Figure 3.14(c)** displays only the curve fit shapes with the corresponding quadratic equations for all rail temperatures. Due to the eccentric heating method the shape is expanding at different rates throughout the rail head. It is emphasized that the shape is not primarily under consideration, but the curvature that develops throughout the thermal cycle.

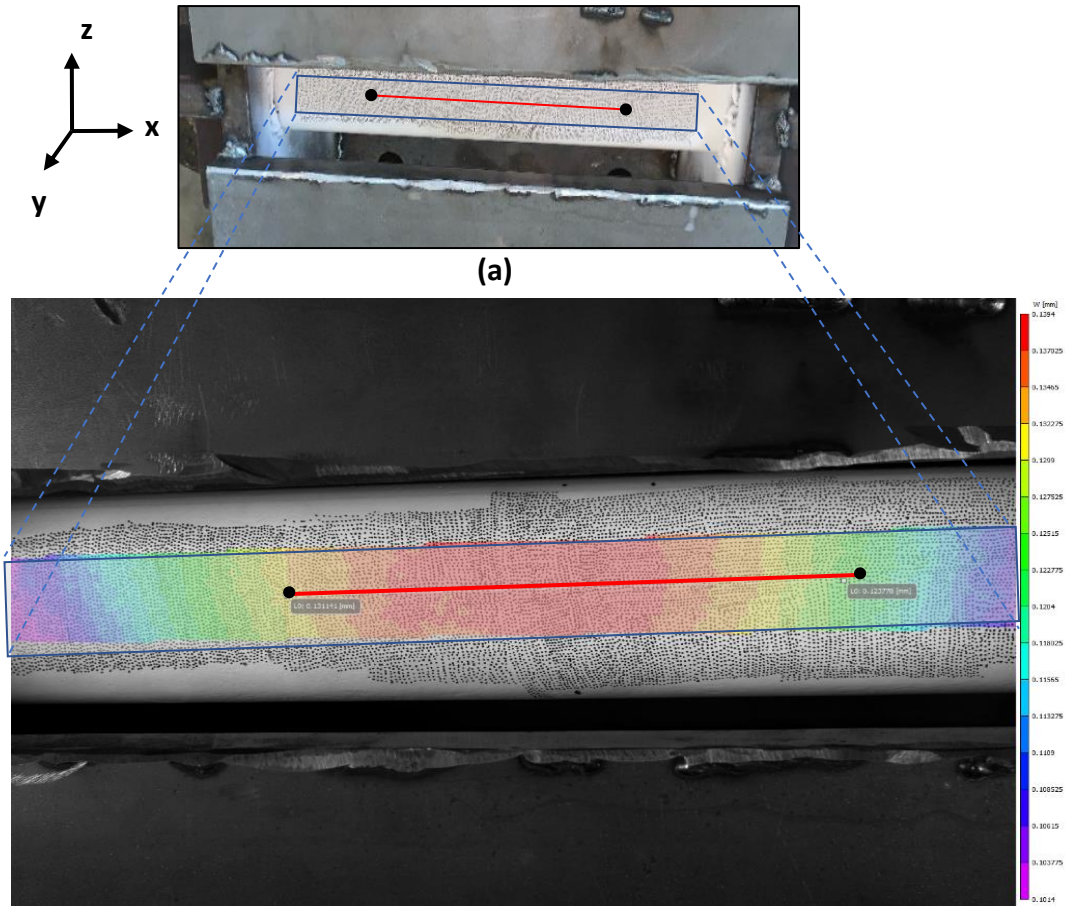

(b) Rail Head Vertical (V) Displacement Field

Figure 3.12: The displacement field of the rail head for the partially constrained specimen: (a) Specimen rail head showing the red line that measurements are acquired; (b) Color map of the displacement field superimposed on the rail

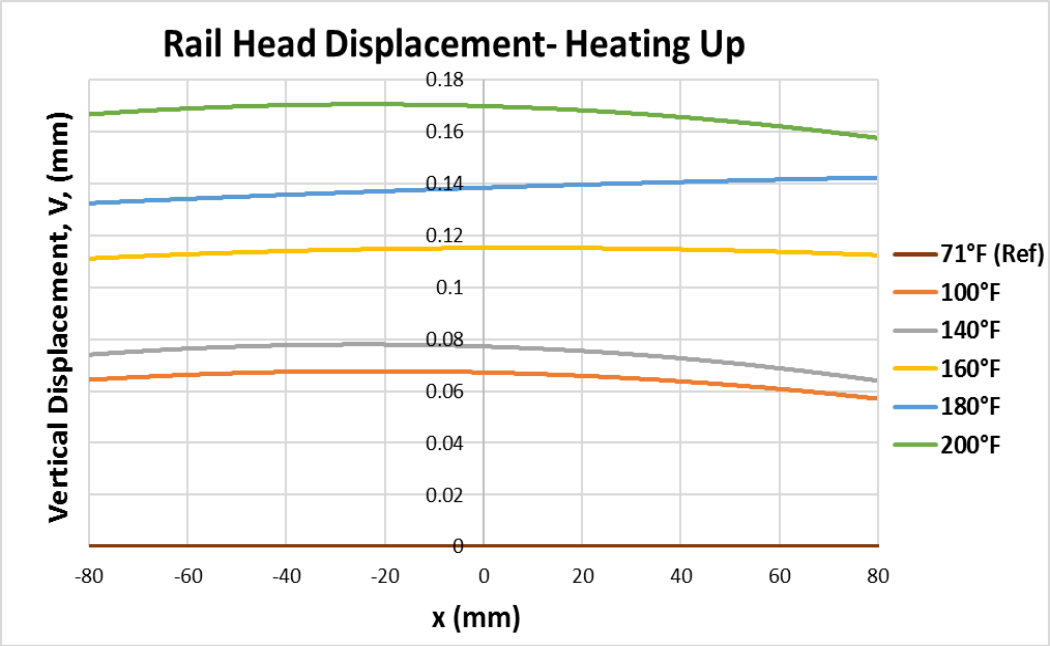

(a)

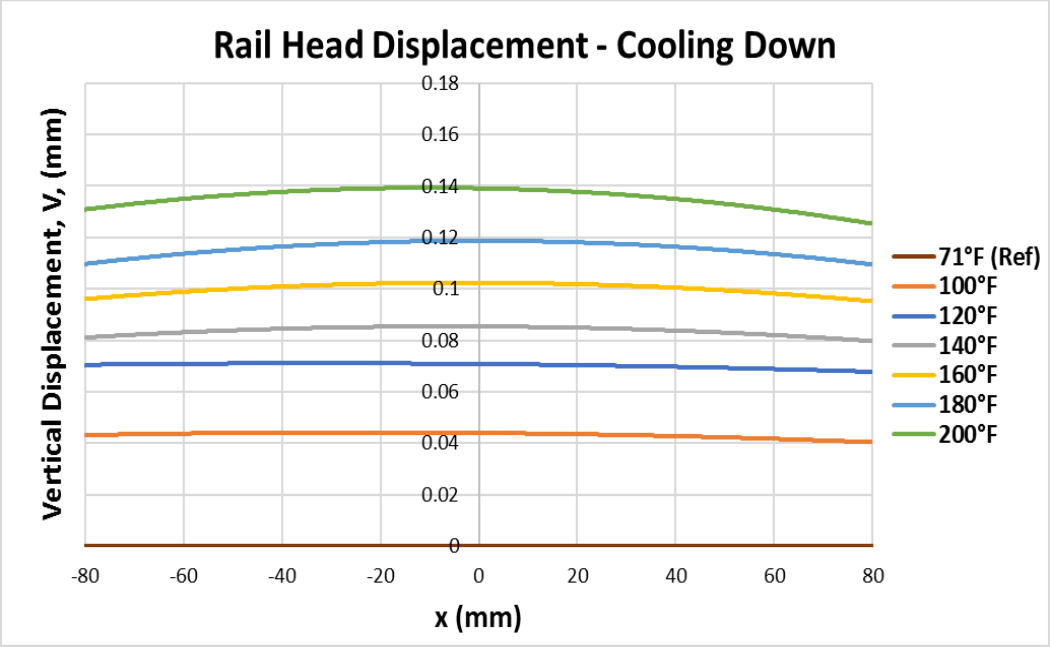

(b)

Figure 3.13: Plots of the StereoDIC acquired displacement: (a) Displacement profiles during the heating process; (b) Displacement profiles during the cooling process

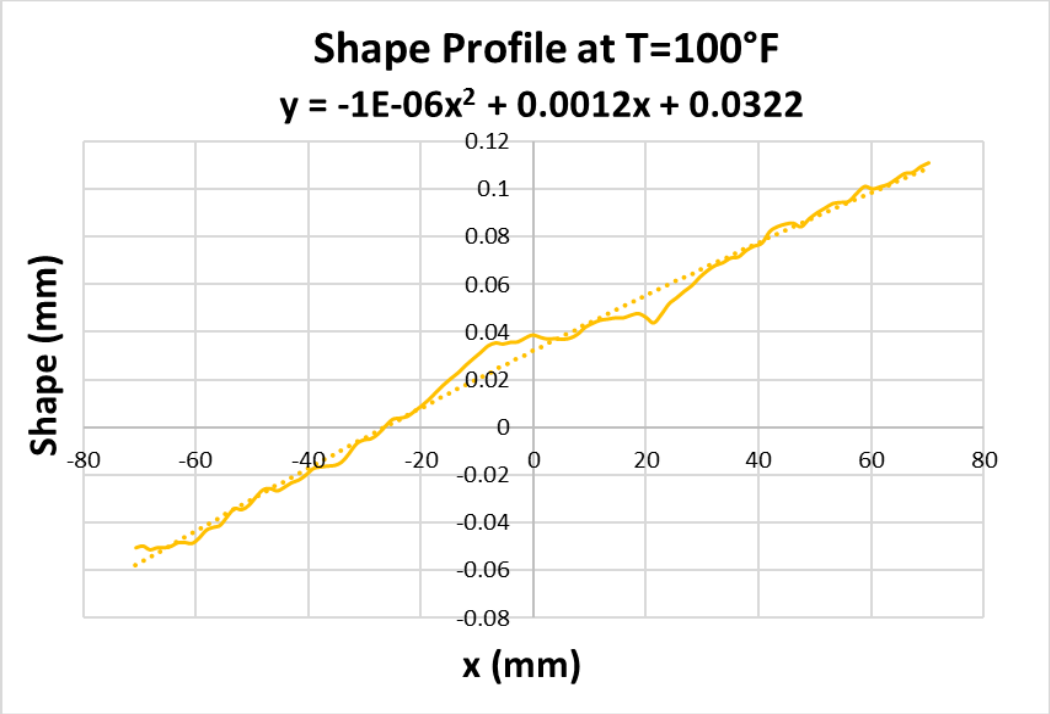
Shape Profile at T=100°F
y = -1E-06x² + 0.0012x + 0.0322
Shape (mm)
0.12
0.1
0.08
0.06
0.04
0.02
0
-0.02
-0.04
-0.06
-0.08
-80
-60
-40
-20
0
20
40
60
80
x (mm)

(a)

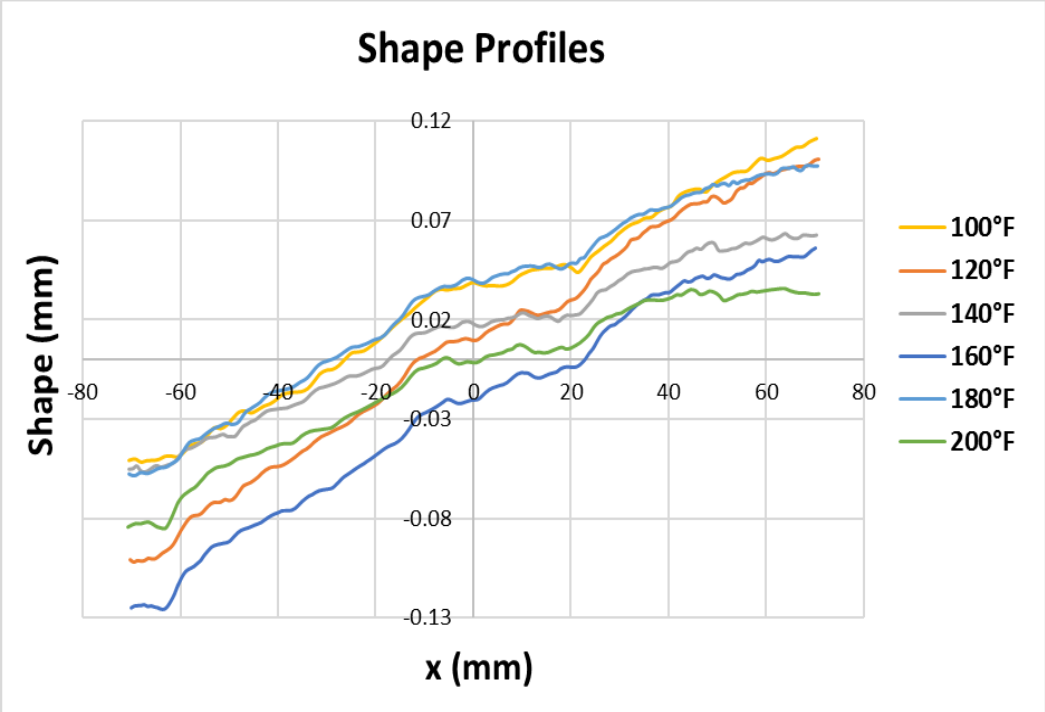
Shape Profiles
Shape (mm)
0.12
0.07
0.02
-0.03
-0.08
-0.13
-80
-60
-40
-20
0
20
40
60
80
x (mm)
100°F
120°F
140°F
160°F
180°F
200°F

(b)

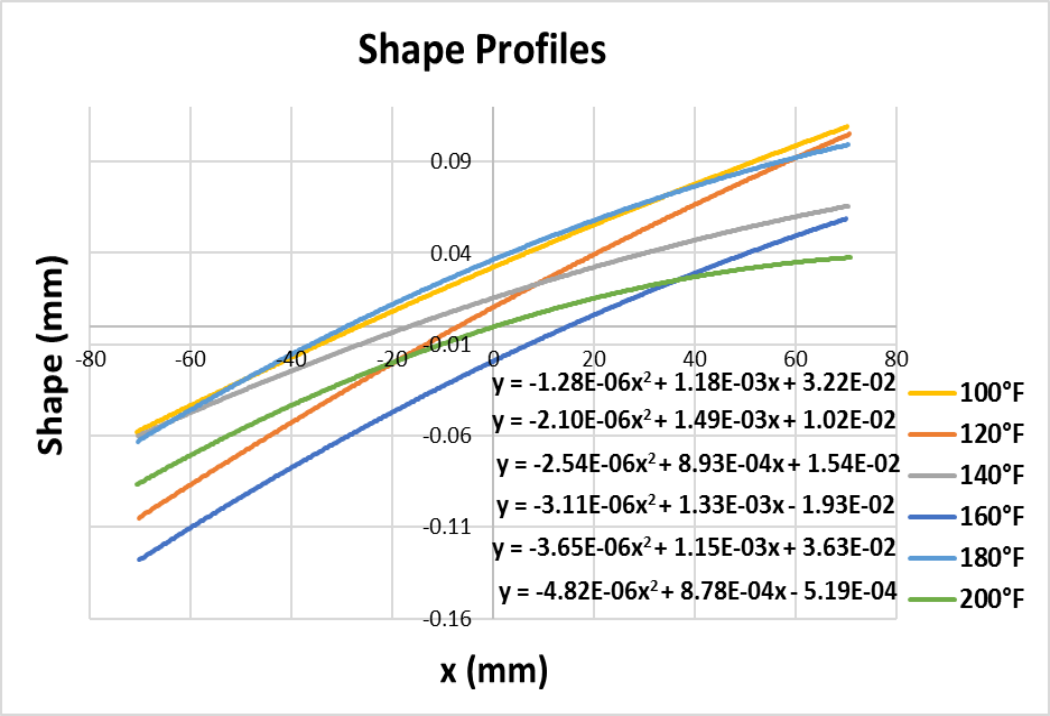

(c)

Figure 3.14: ***StereoDIC captured shape profiles along the partially constrained specimen rail head: (a) Shape profile captured at T=100°F with curve fitting and corresponding equation; (b) Absolute shape profiles at all rail temperatures; (c) Curve fit shape profiles with corresponding quadratic equation***

The curvature can now be computed using these shape profiles. After curve fitting the measurements, the second derivative represents the average curvature within the rail section under consideration. An example of the computation process is performed below:

$$y = (-1.28 * 10^{-6})x^2 + (1.18 * 10^{-3})x + 3.22 * 10^{-2} \qquad T = 100°F \tag{4}$$

$$\frac{dy}{dx} = (-2.56 * 10^{-6})x + 1.18 * 10^{-3} \quad T = 70°F \tag{5}$$

$$\frac{d^2y}{dx^2} = -2.56 * 10^{-6} \quad T = 70°F \tag{6}$$

Based on the defined coordinate system, a negative curvature is computed. It is noted that the sign of the curvature determines if the rail is in tension or compression. A negative curvature indicates the rail is in compression, and a positive curvature indicates that the rail is in tension. Addtional curvature values are calculated in the same manner using the equations obtained in **Figure 3.14(c)** for each temperature increment and are tabulated in **Table 3.2.**

Table 3.2: Computed curve fit equations and curvatures describing the StereoDIC captured shape profiles, corresponding to the known rail temperature increment

Rail Temperature [°F]	Shape Profile Curve Fitting Equation [mm]	Average Curvature [1/mm]
100	$y = -1.28*10^{-6}x^2 + 1.18*10^{-3}x + 3.22*10^{-2}$	-2.56E-06
120	$y = -2.10*10^{-6}x^2 + 1.49*10^{-3}x + 1.02*10^{-2}$	-4.20E-06
140	$y = -2.54*10^{-6}x^2 + 8.93*10^{-4}x + 1.54*10^{-2}$	-5.08E-06
160	$y = -3.11*10^{-6}x^2 + 1.33*10^{-3}x - 1.93*10^{-2}$	-6.22E-06
180	$y = -3.65*10^{-6}x^2 + 1.15*10^{-3}x + 3.63*10^{-2}$	-7.30E-06
200	$y = -4.82*10^{-6}x^2 + 8.78*10^{-4}x - 5.19*10^{-4}$	-9.64E-06

It can then be concluded that the imposed constraints induce measurable out of plane deformations along the rail head. With an increase in temperature, there is an increase in the magnitude of curvature, which assumes that the rail is in compression and the RNT is below the measured temperature. Thus, it possible to compute the curvature in the rail for multiple temperature and then estimate the RNT as the temperature at which the curvature vanishes.

Finite Element (FE) Solutions

Experimental findings are then compared with FE model predictions for the partially constrained rail case. This model is comprised of only one domain, a rail segment,

defined as a 3D deformable solid formed by extruding a 132 RE rail cross section to a length of 16”. The rail is meshed with 35,440 hexahedral-dominated reduced integration elements. This is comprised of 34,080 linear hexahedral elements (C3D6RT) and 1,360 linear wedge elements (C3D6T). **Figure 3.15** shows the geometry and mesh of the rail segment. A general statics model type is chosen for this study which requires only mechanical properties to be defined. Typical steel material properties are selected to define the rail component given in **Table 3.1**. A static analysis uses predefined temperature fields to subject the rail to temperature change. A predefined temperature field is used to initially define a rail temperature of 70°F, the assumed experimental RNT. Subsequently, the longitudinal constraints defined at the rail ends are then activated at this temperature, defining the RNT as 70°F. The predefined temperature field is then modified to 200^{o}F and an amplitude definition is used to discretize the time steps into temperature increments that simulate the experimental temperature readings. This 200°F temperature represents the maximum rail temperature that deformation measurements are captured by the StereoDIC system. A more in-depth description of the model type can be found in **Chapter 4**. Shape deformations are extracted along the center line of the rail head, path A-A, as shown in **Figure 3.15(a)**.

Figure 3.16 displays the FE vertical shape deformation profiles in respect to the position along the rail, x, relative to the center position. These profiles depict the deformed rail head shape for different rail temperatures, in respect to the initial undeformed shape at the RNT or T=70°F. Curve fitting is applied to all shape profiles and the quadratic equation is displayed to describe the average behavior of the entire rail

section. It is found that as the rail increases in temperature, the vertical deformations increase linearly in response. This is a finding that is clearer in the cooling down process of the StereoDIC measurements, as opposed to the heating up process.

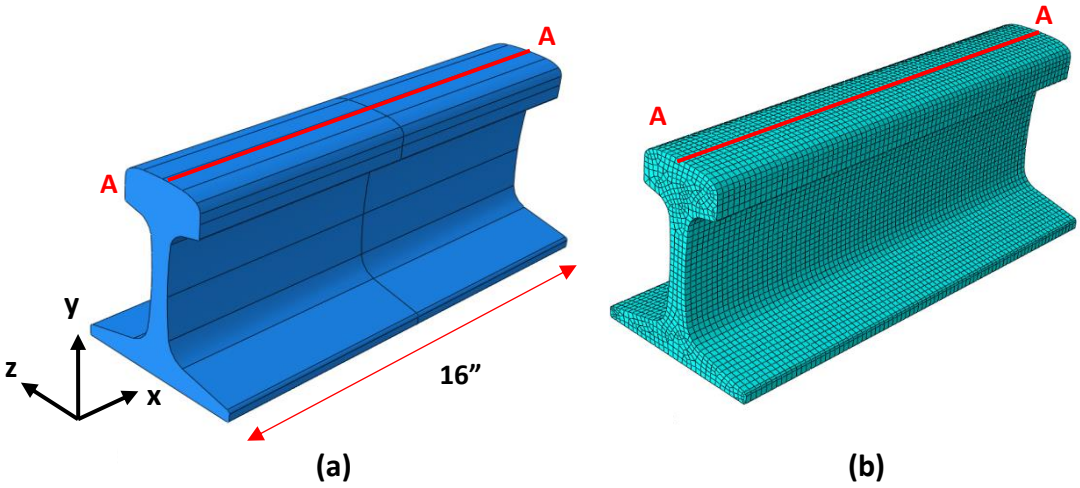

Figure 3.15: FE rail depicting path A-A at which shape measurements are extracted: (a) Rail geometry with corresponding dimensions; (b) Rail mesh

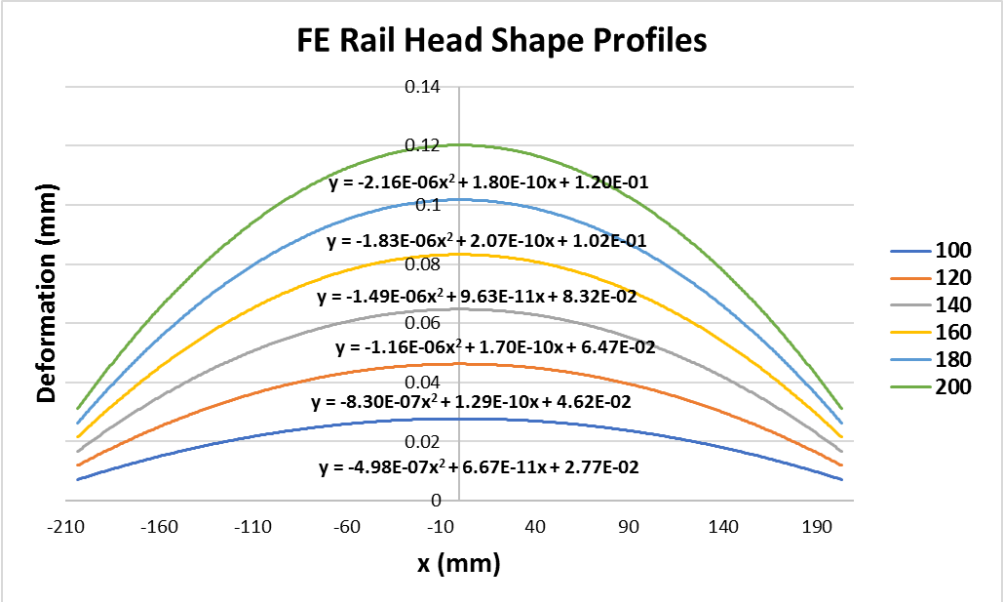

Figure 3.16: Plots of the FE simulated shape profiles along the rail head of a constrained rail

The shape profiles of the FE measurements are in reference to the undeformed RNT shape which reflects a perfectly flat rail head with no geometric irregularities that exist in the experimental rail specimen shown in **Figure 3.14(b)**. The curvature of the FE rail can be computed by taking the second derivative of the each of the shape profile quadratic equations. This curvature describes the average curvature over the entire rail segment. Each rail temperature is plotted in respect to curvature for comparison of the FE numerical solution and the captured StereoDIC measurement results in **Figure 3.17**. Linear regression is applied to both data sets with fits defined by a linear equation and the R^2 parameter. The R^2 parameter indicates that the linear fit adequately represents the StereoDIC measurement results and perfectly represents the FE numerical solutions. The y-intercept is then used to estimate the RNT. The StereoDIC measurement system estimates an RNT of 63.13°F and the FE model predicts an RNT of 70.14°F, indicating that there is reasonably good agreement between model predictions and experimental data.

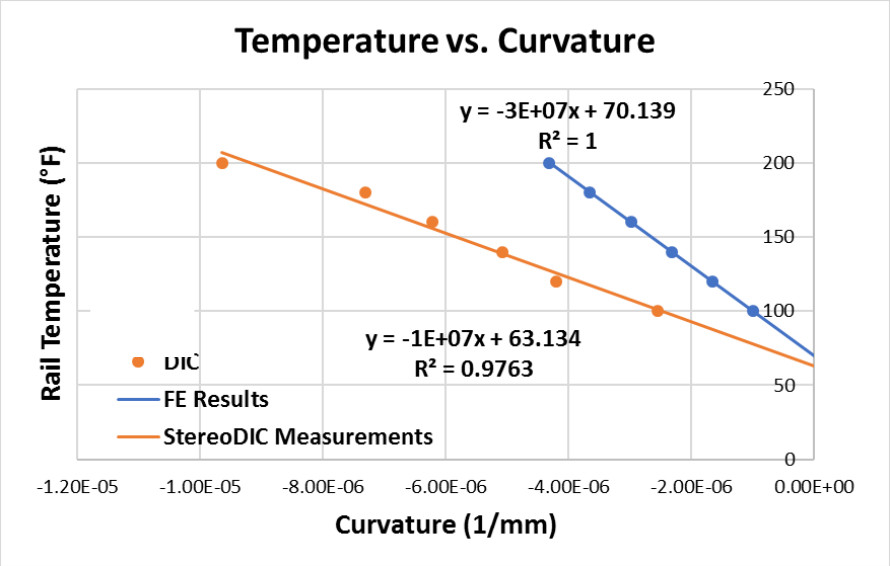

Figure 3.17: Plot comparing temperature-curvature relationships for FE solutions and StereoDIC results (lines extended to intersect y-axis)

3.3.4 Deformation Testing Assessment

It is concluded that the proposed StereoDIC system accurately captures deformations along the rail head. The shape profiles can then be used to compute curvatures that are used to accurately estimate the RNT. A FE computer simulation is developed for validation. Results from both FE predictions and experimental measurements are in good agreement, but various experimental sources could cause the difference found with the measurements. In addition to the sources of error found throughout strain testing discussed in section **3.3.2**, the following factors may contribute differences between FE predictions and StereoDIC measurements.

- The rail specimen used for the experimental measurements is considered only partially constrained longitudinally, whereas the rail in the FE model is fully constrained longitudinally.
- The longitudinal stiffness that the supports impose at rail ends may not be uniform due to imperfections in the welds and the steel supports. Additionally, the support configuration along the rail head includes two steel plate strips, while the bottom of the rail includes only one large base plate (see **Figure 3.3**). This may induce a non-uniform stiffness distribution along the rail ends between the rail head and rail base, causing non-uniform deformations.
- The heating source that is used for experimental testing fails to heat the rail uniformly. This non-uniform heat distribution led to temperature variations along the rail head. Therefore, temperature measurements at

the rail head center point that define each data set are only an indication of the rail temperature at this point, not the entire rail head. The temperature field measurement system used in future work should be capable of accurate full-field temperature measurements so that improved estimates for the RNT can be obtained.

- The FE model assumes an RNT of 70°F because this is approximately the rail temperature at which the supports were welded to the rail specimen, whereas, the actual RNT is unknown and the StereoDIC measurement system is employed to accurately estimate it.
- The FE solution trendline describes the average behavior of the shape deformation profiles along the entire length of the rail segment. The StereoDIC measurement system used in these studies is capable of acquiring measurements for a shorter portion of the rail. If measurements are to be obtained over the entire rail, then the StereoDIC system setup must be modified so that the entire length of the rail is imaged for data analysis.

Some of these differences are a result of the FE simulation representing a perfect system, which is impractical for laboratory experimentation, while others could be minimized with refinement of laboratory procedures and specimen setup. Despite the various sources of error, measured shape profiles along the rail head are used to accurately estimate the RNT. This test serves as a verification and validation of the hypotheses on which the method is developed.

3.4 RNT Measurement Method Development

In view of the observations and investigations discussed in the preceding sections, the proposed method for measuring RNT and the state of stress in the rail is formulated. The proposed method is based on the deformation and strain measurements taken at known temperatures within a naturally occurring, or induced, thermal cycle (e.g. 24 hours) which may or may not include the RNT. It is noted that, at any given temperature, the curvature of the rail head is uniquely determined by shape measurements without the need of a stress-free reference shape. In view of the linear relationship between temperature, T, and curvature at the top of the rail over the ties, k, two curvature measurements, k_1 and k_2, at two distinct temperatures, T_1 and T_2, define a line

$$T = RNT + [(T_2 - T_1)/(k_2 - k_1)]k \tag{7}$$

Thus, the recorded temperature can be plotted as a function of curvature measurements, as shown in **Figure 3.18(a)**. The y-intercept (zero curvature) represents an estimate of the RNT. The proposed method, thus, is a reference-free method. The strain measurements acquired after temperature has changed by ΔT are in reference to an arbitrary baseline temperature that most likely is not the RNT, and, thus, only the slope $\Delta T/\Delta\varepsilon_y$ of the temperature-strain relationship can be established (dashed line in **Figure 3.18(b)** with baseline temperature assumed 0°F). However, with the RNT already computed, the temperature-strain relationship can be uniquely defined and plotted as a line (solid line in **Figure 3.18(b)**) with a Y-intercept at the RNT and slope as defined by the strain measurements at different temperatures.

$$T = RNT + (\Delta T/\Delta\varepsilon_y)\varepsilon_y \quad (8)$$

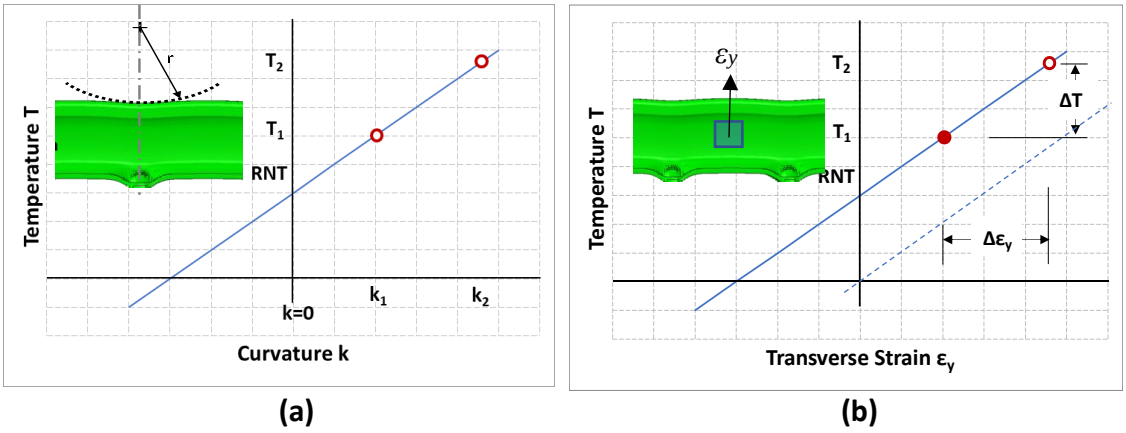

Figure 3.18: Method procedure steps: (a) Step 1 – Estimate the RNT from curvature data along the rail head about the anchoring points (b) Step 2 – Use the RNT from Step 1 and acquired strain data to establish the unique temperature-strain relationship

The longitudinal stress at a specific temperature can now be computed analytically and in a straightforward manner based on plane stress conditions. Plane stress is a two-dimensional state of stress and can be defined as the state where the nonzero stress components act in one plane only (Kelly 2015). This assumption is typically made for thin bodies, such as the rail web (see **Figure 3.19**) which assumes $\sigma_z = 0$.

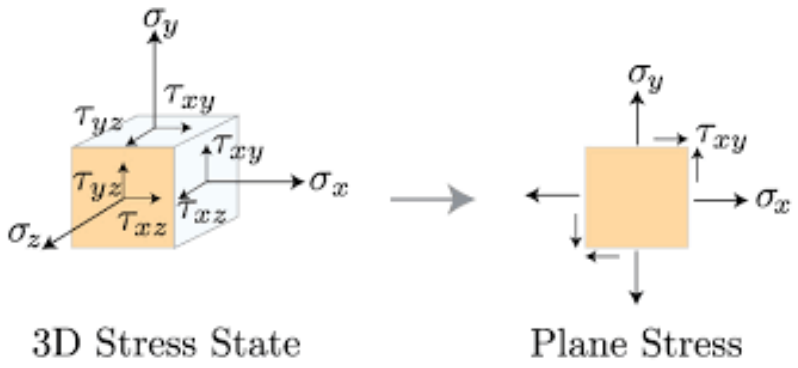

Figure 3.19: Diagram depicting a 3D stress state transitioning to the plane stress state where $\sigma_z = 0$ (Boston University Mechanical Engineering 2019)

In this case the constitutive relationship is expressed as:

$$\begin{Bmatrix} \varepsilon_x \\ \varepsilon_y \\ \gamma_{xy} \end{Bmatrix} = \begin{bmatrix} 1 & -\nu & 0 \\ -\nu & 1 & 0 \\ 0 & 0 & 1+\nu \end{bmatrix} \begin{Bmatrix} \sigma_x \\ \sigma_y \\ \tau_{xy} \end{Bmatrix} + \begin{Bmatrix} \sigma_x \\ \sigma_y \\ \tau_{xy} \end{Bmatrix}_0 \quad (9)$$

The normal strain components, ε_x and ε_y are therefore expressed as:

$$\varepsilon_x = \frac{\sigma_x}{E} - \frac{\nu\sigma_y}{E} + \varepsilon_{x0} \quad (10)$$

$$\varepsilon_y = -\frac{\nu\sigma_x}{E} + \frac{\sigma_y}{E} + \varepsilon_{y0} \quad (11)$$

Where ε_{x0} = ε_{y0} are the initial thermal strain in the longitudinal and transverse direction.

Subtracting ε_x from ε_y yields:

$$\varepsilon_x - \varepsilon_y = \sigma_x \frac{(1+\upsilon)}{E} - \sigma_y \frac{(1+\upsilon)}{E} + (\varepsilon_{x0} - \varepsilon_{y0}) \quad (12)$$

Assuming the initial strains are zero, $\varepsilon_{y0} = \varepsilon_{x0} = 0$,

$$\sigma_x \frac{(1+\upsilon)}{E} = \left(\varepsilon_x - \varepsilon_y\right) + \sigma_y \frac{(1+\upsilon)}{E} \quad (13)$$

Solving for longitudinal stress, $\sigma_{x,}$

$$\sigma_x = \left(\varepsilon_x - \varepsilon_y\right) \frac{E}{(1+\upsilon)} + \sigma_y \quad (14)$$

And thus, the longitudinal stress can be estimated using Equation (14) for any temperature as a function of acquired thermal strain measurements and material properties.

Chapter 4. Computer Models of Rail System

Computer simulations investigating the effects of the typical boundary conditions and thermal loadings of a rail segment are conducted to identify characteristic deformation patterns that provide insight to the type of data that needs to be collected in order to estimate the RNT and longitudinal stress in the rail. To this end, commercial software Abaqus is used to develop FE thermoelastic models to compute deformations at critical areas of interest. This chapter introduces the standard baseline model of a rail system used in the computer simulations of this work (baseline model analysis is presented in section **5.1**). The models developed for experimental testing are a simplified model of the full-scale model described in this chapter. The models used in the parametric studies are derivatives of the baseline model and any specific details are discussed in the corresponding sections. The parts of a physical rail system, and the functions and simplifications that are made for the development of the computer models are presented. In-depth descriptions are given of each of the model components along with geometry and meshing aspects, mechanical and thermal material properties, and their integration in the rail system. The mechanical and thermal boundary conditions and loadings applied to the rail system are also presented.

4.1 Physical System

A track system consists of five major components: rail, tie plate, fastener system, tie, and ballast shown in **Figure 4.1**.

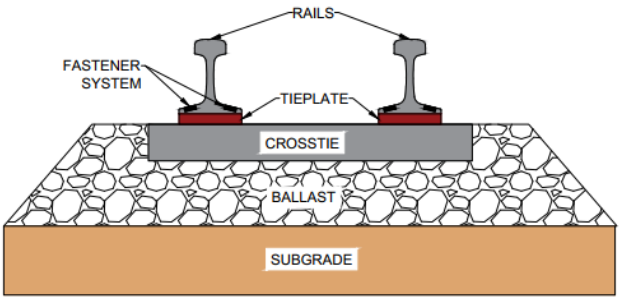

Figure 4.1: Simplified track system diagram

The rail in track is the primary focus in these computer simulations. All additional track components modeled in these simulations are considered solely for the purpose they serve in supporting the rail. Tie plates are the steel plates placed between the rail and tie to provide a seating area for the rail. While their main function is to support the rail and transmit loadings to the ties, they also assist in fastening the rail to the tie. The rail fastener system is a group of components whose main function is to secure the rail segments to the ties. By fastening the rail to the ties, the system is preventing rail vertical uplift, along with horizontal and lateral movement (Agico Group 2019). The fastener system components may include, but are not limited to, a rail anchor, rail spike, rail pad, washer, rail insulator, rail shoulder, etc. The multi-component fastener system and its geometry are simplified in these models to one single part that restrains vertical, horizontal, and lateral movement. Ties support the rail and serve as a flexible and elastic medium between the rail and the ballast, absorbing and transmitting the train loads to

the substructure (White 1984). Additionally, the tie prevents lateral track displacement and longitudinal rail movement when coupled with the rail fastener system. This elastic support and lateral and longitudinal constraint are simplified to the boundary conditions defined at the bottom surface of the tie plate component. The ballast is the start of the substructure layer and functions to support the overall track system. It must provide both strength and rigidity to sustain the loads it may encounter, as well as provide an elastic foundation for the track (White 1984). This component is also simplified to the boundary conditions located at the bottom surface of the tie plate component. The subgrade is not considered.

4.2 Model Solver Types

Different model solvers are used to subject the rail to temperature changes. A static analysis is performed with a general statics model solver and a thermoelastic analysis is performed with a coupled-temperature displacement model solver. These model solvers are described in the following sections.

4.2.1 General Statics

The general static stress analysis is used when inertia effects can be neglected, the problem may be linear or nonlinear, and time-dependent material effects can be ignored (Dassault Systèmes Simulia Corporation n.d.). The model is solved with the direct method equation solver and user solver default matrix storage. The Full Newton solution technique is utilized and the default load variation with time is set to ramp linearly over the step. Initial, minimum, and maximum time increments are set at 0.1, 1E-6, and 0.1,

respectively. These increments are used to discretize the temperature changes. This model type typically provides the fastest computational time for linear analysis and involves defining the boundary conditions, predefined fields and load cases. This is a simplistic approach at computing the strain and deformation effects due to a thermal loading. For the purposes of the model required for this problem, the following material properties must be defined: (i) modulus of elasticity, (ii) Poisons ratio, and the (iii) coefficient of thermal expansion.

4.2.2 Coupled Temperature-Displacement

A coupled temperature-displacement model is also developed that performs a thermoelastic analysis, through a nonlinear calculation, that simultaneously solves for the displacements and temperature (Dassault Systèmes Simulia Corporation n.d.). Thermal and mechanical boundary conditions are required for this solver. The backwards difference scheme is used to integrate temperatures, and the coupled system is solved using the Full Newton solution technique (Dassault Systèmes Simulia Corporation n.d.). An unsymmetrical matrix storage equation solver is required with an instantaneous load variation with time. The steady state or the transient response can be solved for. The time step increment sizes set for the initial, minimum, and maximum, are 0.1, 1E-6, and 0.1, respectively. These increments are used to discretize the thermal loading. A maximum allowable temperature change per increment is also required and is set to 50°F. This method requires defining additional thermal and mechanical material properties including: (i) specific heat, (ii) conductivity, (iii) density, (iv) modulus of elasticity, (v) Poisson's ratio, and the (vi) coefficient of thermal expansion.

4.3 Model Components

The FE models consist of three major track domains, i.e., the rail, tie plate, and fastener system, while the tie and ballast are modeled through boundary conditions defined at these track domains. The geometry and mesh attributes detailed here are for the standard baseline model that is primarily used for this thesis which is based on the current configuration of the Indoor Testing Track found at USC. Throughout the parametric studies performed in **Chapter 5**, different geometries and mesh attributes are used and not detailed in this section.

4.3.1 Rail

The rail component is modeled as a 132 RE AREMA standard rail cross section and extruded to a length of 180” to simulate the rail currently found in the testing bed at the USC Railway Testing Facility. The rail is defined as a 3D deformable solid discretized into 35,640 linear hexahedral elements of type C3D8RT with reduced integration. A finer mesh was tested but produced approximately the same results at the critical areas of interest as the coarser mesh. The cross-section geometry, FE mesh, and table with the geometric properties are shown in **Figure 4.2**.

4.3.2 Tie Plate

The tie plate is dimensioned 6” x 8.5” and represents the rail-tie interface. These dimensions are chosen based on a 132 RE rail cross section, for which the rail base width is 6”, and the typical rail seat length for concrete ties, approximately 8.5”. The tie plate is assumed rigid and is modeled as a 3D deformable shell, with rigid body conditions tying all translations to the reference point located at the tie plate center. The tie plate is

discretized into 5,208 linear quadrilateral S4R elements with reduced integration. The location of the tie plate is found at B shown in **Figure 4.3(c)**

4.3.3 Fastener System

The fastener system is simulated to represent the transfer of forces to the rail, shown in **Figure 4.3(a)** as the physical component and **Figure 4.3(b)** as the Pandrol 'e' Clip**.** Due to the uniqueness and complexity of the design of the clip, the fastener system is simplified as a plate through which the clip transfers the forces on the rail. The length and width dimensions are 3.75" x 1.25"; the rail contact area of the fastener. This component is also modeled as a 3D deformable shell, with a rigid body conditions tying all translations to the reference point found at the center of the shell. This component is discretized into 456 linear quadrilateral elements of type S4R with reduced integration. The location of the fastener is found at A shown in **Figure 4.3(c)**.

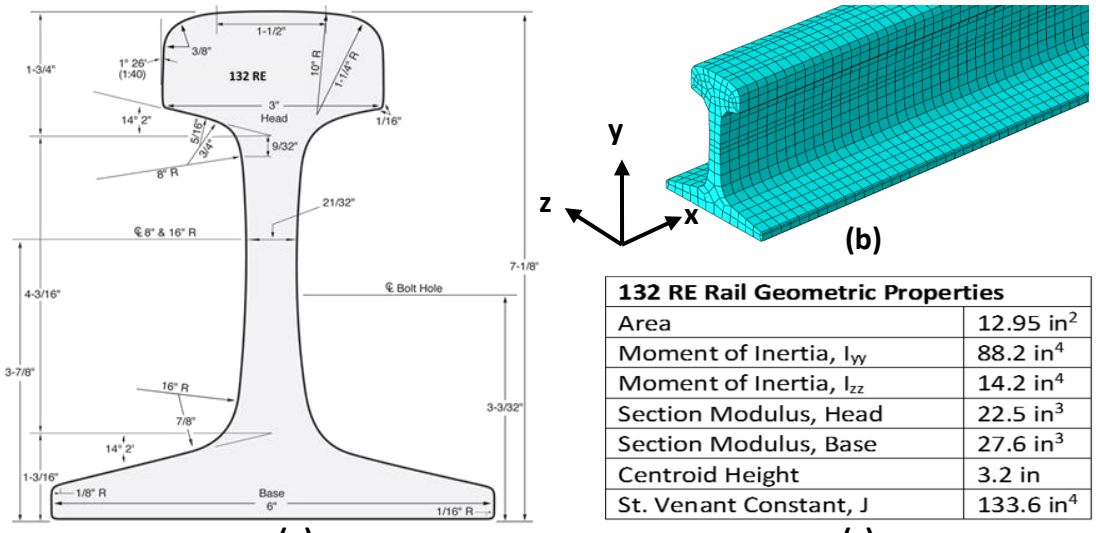

132 RE Rail Geometric Properties	
Area	12.95 in^2
Moment of Inertia, I_{yy}	88.2 in^4
Moment of Inertia, I_{zz}	14.2 in^4
Section Modulus, Head	22.5 in^3
Section Modulus, Base	27.6 in^3
Centroid Height	3.2 in
St. Venant Constant, J	133.6 in^4

(c)

Figure 4.2: 132 RE rail cross section: (a) Geometry (Harmer Steel Co. 2014); (b) FE mesh; (c) Geometric properties (Orringer, Morris and Jeong 1986)

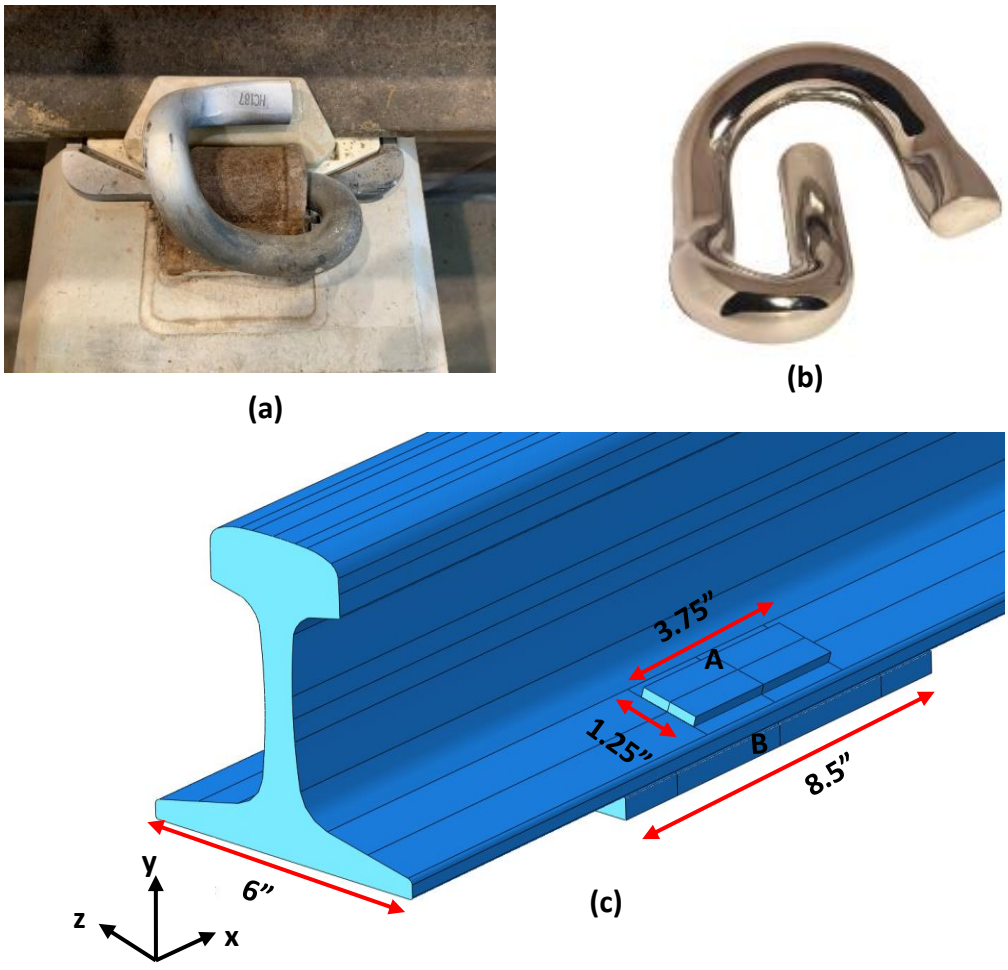

Figure 4.3: Tie plate and fastener system: (a) Physical component locations; (b) Physical Pandrol e-clip (Pandrol USA 2019); (c) FE model with displaying Point A as the clip location and Point B as the tie plate location (shell element thicknesses are scaled up by 5 for display purposes)

4.3.4 Track Configuration

The FE baseline track configuration represents the existing track configuration found in the Railway Testing Facility. This configuration includes 9 tie locations over the 180” segment. Ties are spaced 20” center-on-center between two ties. The ends however, are 10” from the first tie location, half of the tie spacing. The tie support locations are considered as the center location of the tie plate. The FE track configuration is depicted in **Figure 4.4**.

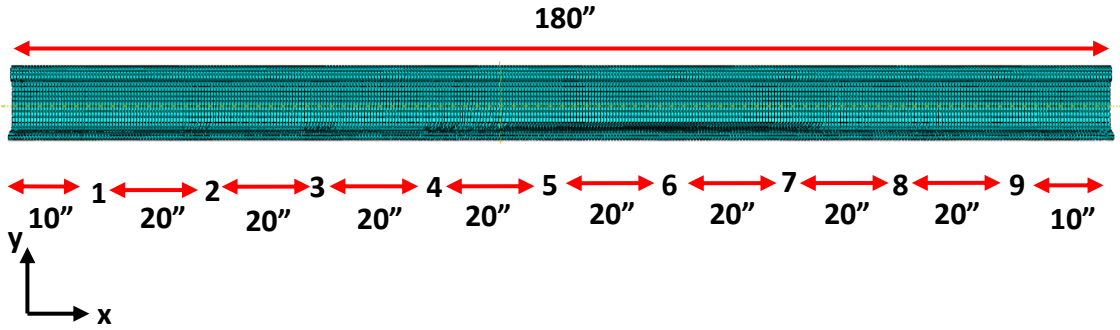

Figure 4.4: FE model track configuration with corresponding dimensions (tie support locations are labeled in black)

4.4 Materials

All components are assigned the required mechanical and thermal properties to perform either a static or thermoelastic analysis in Abaqus/Standard. Typical steel properties are selected and used to define the model components. Only the rail component is subjected to the thermal loading, therefore it is the only component defined with thermal material properties. The tie plate and the fastener component are defined with only elastic steel properties. **Table 4.1** lists all the steel material properties defined.

Table 4.1: Steel material properties defined in FE models

	Property	**Value**
Steel	Modulus of Elasticity (psi)	29×10^{6}
	Poisson Ratio	0.3
	Thermal Expansion Coefficient (in/in/°F)	6.7×10^{-6}
	Specific Heat (Btu/(lb-°F))	0.122
	Conductivity (Btu/s*°F*in)	7.18×10^{-4}
	Density ($lbf*s^2/in^4$)	730×10^{-6}

4.5 Boundary Conditions

Coupled temperature-displacement models require both mechanical and thermal boundary conditions, while the general statics model only require the mechanical boundary conditions. The mechanical natural boundary conditions are the prescribed displacements (U_o) defined at the rail ends, tie plates, and fastener systems. The thermal boundary conditions required for the rail component include an initial temperature (T_o) and heat flux (q_o). The temperature and deformation fields can then be computed and analyzed given these prescribed conditions. The models created consider a single side of a track system and are centered around the rail component. Parametric studies incorporate various mentioned track system components to decipher the necessary components. The boundary conditions and connections between components are described in the following sections.

4.5.1 Connection to Crossties and Ballast

Throughout this study, the tie plate component is defined to simplify the track structure beneath the rail. The material properties represent the tie plate itself, while the geometric design is specific to a rail size and tie width. The boundary conditions and springs defined on the tie plate are simulating the functions of the ties and ballast. The FE models developed investigate two different tie plate boundary conditions: tie plates with springs (TPS), or tie plates vertically constrained (TPC). These boundary conditions are simplified to their 2D form, shown in **Figure 4.5.** The mechanical boundary conditions defined at the reference point located at the centroid of the plate are to simulate effects of the tie. One of the ties functions is to prevent lateral and longitudinal displacement.

This is simulated by constraining x and z displacements at the reference point of the tie plate. All parametric model variations define this constraint.

4.5.1.1 Tie Plate Constrained (TPC)

This approach represents a simplification of the effects that the ties and ballast have on the allowable vertical movement. In the TPC case, vertical translations are fully constrained at the reference point of the tie plate. In addition to this boundary condition, the x and z displacements are also fixed at this reference point, to simulate additional support by the tie component. This support condition is assuming that the rail is completely tied to the ground surface during installation, as shown in **Figure 4.5(a**).

4.5.1.2 Tie Plate Springs (TPS)

The tie plate spring (TPS) condition considers the effects of the elastic track structure by simplifying their connection to the system through springs. This is performed by attaching vertical springs to the nodes on the bottom surface of the tie plate and connecting them to the ground surface. The ground surface can be defined as a fixed plane beneath the spring. The required stiffness is dependent on the track configuration tie spacing, S_{tie}, and the General Track Modulus, K_{track}. Utilizing the Timoshenko Beam Theory, the spring stiffness, K_s can then be calculated as follows: (Timoshenko and Langer 1932)

$$K_s = K_{track} * S_{tie} \tag{15}$$

A resilient tie plate type is initially selected indicating a General Track Modulus of 4,000 psi (RailTEC - University of Illinois at Urbana-Champaign n.d.) and the track configuration

utilizes a 20” center-on-center tie spacing. These two values can then be directly inputted into this equation to compute a spring stiffness of 80,000 lb/in. This stiffness is evenly distributed amongst 9 vertical springs, placed equidistance apart relative to the center, on the tie plate rigid body as shown in **Figure 4.5(b)** below.

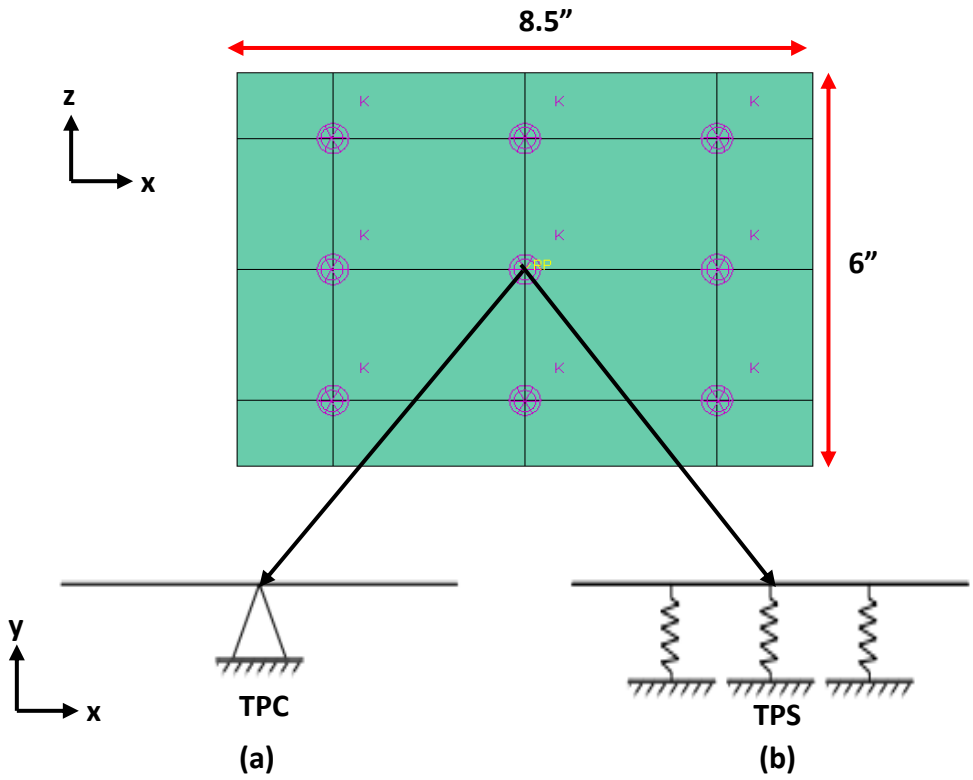

Figure 4.5: FE tie plate boundary condition cases: (a) 2D depiction of the TPC case; (b) 2D depiction of TPS case showing 3 of the 9 springs, additional springs are not shown because they exist in the z plane but are shown on the FE tie plate as purple circles with K notation

4.5.2 Rail to Tie Plate Connection

The tie plate component is found directly under the rail component. Two model variations are initially investigated to determine the necessity of the fastener system in FE models. Models denoted with a 1, after TPS, integrate the fastener system into the track system, while models denoted with a 0, do not include this component.

Incorporation of the fastener system led to definition of different contact properties described below.

4.5.2.1 Contact Definition with Fastener System

In addition to preventing uplift between the rail and tie plate, the fastener system also generates a normal force that prevents the rail from sliding along the tie plate surface, therefore, creating a longitudinal rail constraint. When the fastener system is incorporated, a surface-to-surface interaction is defined between the rail-tie plate interface, comprised of a normal and tangential behavior. The tangential behavior defines a penalty friction formulation with a friction coefficient, $\mu = 0.7$ (Elert n.d.). This friction coefficient defines typical steel-on-steel contact for dry conditions. The normal behavior defines a hard contact surface, allowing for separation between the surfaces.

4.5.2.2 Contact Definition without Fastener System

When the fastener system is not incorporated, the assumption can then made that the horizontal force generated at the rail-tie plate interface remains less than friction, therefore, the surface-to-surface interaction is no longer necessary. A tie constraint is then deemed adequate to couple all degrees of freedom between the rail-tie plate interface. The bottom surface of the rail is tied to the top surface of the tie plates, excluding shell element thickness.

4.5.2.3 Fastener System Connection to Rail

The fastener system's main function is to fasten the rail to the tie and to prevent uplift and lateral and longitudinal movement. An interaction property is created to define

the surface-to-surface contact between the bottom of this component and the parallel rail surface along the bottom flange where it is anchored. This surface-to-surface contact considers both the normal and the tangential response and is identical to the rail-tie plate contact behavior. The tangential behavior adopts a penalty friction formulation with a friction coefficient of 0.7 (Elert n.d.) to represent steel-on-steel contact for dry conditions. This satisfies the system's function of preventing longitudinal and lateral movement. The normal behavior assumes hard contact between the surfaces and allows for separation. This ensures that the rail base can freely deform vertically until reaching the maximum uplift defined by the position of the fastener system.

4.5.3 Fastener System Connection to Tie Plate

As the rail is anchored to the ties, the fastener system imposes a vertical clipping force on the rail surface, in addition to the constraint defined by its position. A contact surface is defined to connect the bottom surface of the fastener system to the rail. The other end of the fastener is connected to the tie plate using connector elements. Depicted **Figure 4.6**, a basic axial connection type is selected to define a vertical spring from the center reference point of the fastener system to the tie plate beneath it. Connector elements are selected as opposed to simple spring elements to impose the initial clipping force developed as the fastener system anchors the rail to the ties. The Pandrol USA 'e' Clip is selected in this study with a load-deflection response curve shown in **Figure 4.7** (Pandrol USA 2019). Assuming a nominal toe load of 2,750 lbs, the corresponding clip toe deflection is 7/16" and the spring stiffness is then computed as 6,285.71 lb/in.

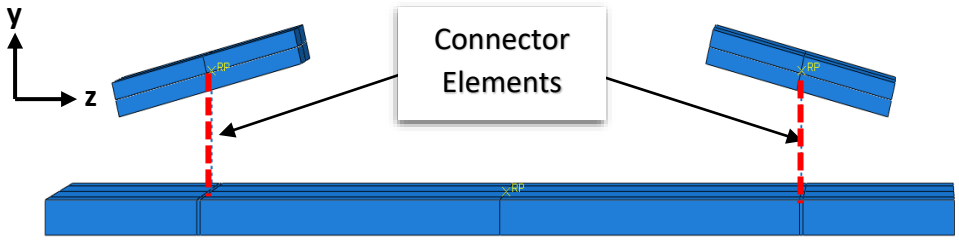

Figure 4.6: FE depiction of the axial connector elements used to connect the fastener system from its center reference point to the tie plate through a pre-compressed spring (shell element thickness is scaled up by 5 for display purposes)

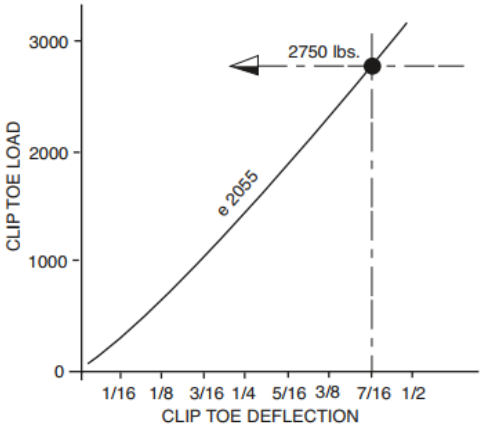

Figure 4.7: Pandrol 'e' clip toe load as a function of clip toe deflection (Pandrol USA 2019)

To impose an initial clipping force on the rail, axial connector elements are used to define pre-compressed springs. The connector element stiffness, K_c, is calculated as:

$$K_c = \frac{F_{tl}}{L - L_{ref}} \tag{16}$$

where F_{tl} is the e-clip nominal toe load, K_c is the spring stiffness, L is the initial length of the connector, and L_{ref} is a reference length. The initial length between the fastener and

the tie plate is determined as 0.178", and, therefore, to achieve a toe load of 2,750 lbs, the reference length is computed as L_{ref}= 0.256".

4.5.4 Boundary Conditions at Rail Ends

Different boundary conditions defined at the rail ends are investigated to determine the effects of the level of longitudinal constraint on deformation and strain measurements. All cases consider fully constrained rotations at the rail end faces. The following rail end boundary condition cases are investigated: fully constrained, unconstrained, and elastically constrained. The 2D boundary condition depiction is shown in **Figure 4.8**.

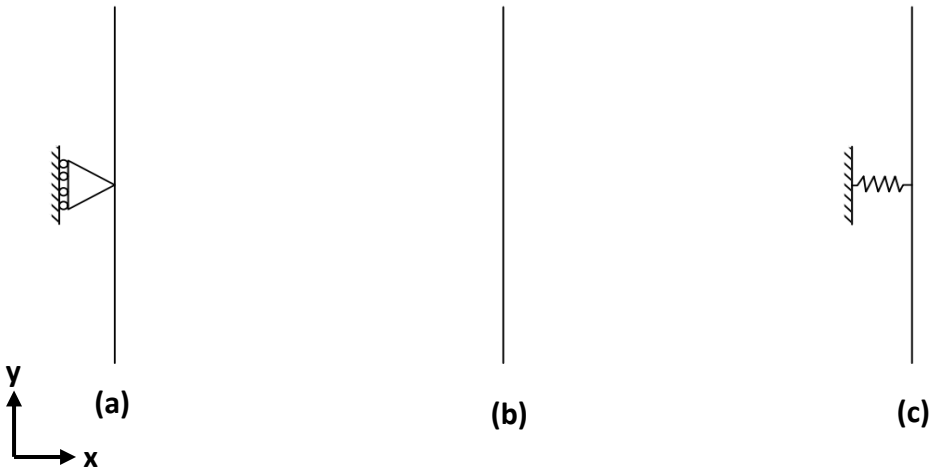

Figure 4.8: 2D depiction of rail end boundary condition cases: (a) Fully constrained longitudinally; (b) Unconstrained; (c) Elastically constrained case defined by a spring

The fully constrained case prevents the rail from deforming longitudinally, x, as shown in **Figure 4.8(a).** This support condition is defined for the entire rail end surfaces. However, the rail is still free to deform in the plane of the end face (y and z directions).

The unconstrained case allows the rail to freely deform in all directions, as shown in **Figure 4.8(b).** In the elastically constrained case, linear springs are designed to restrain the longitudinal expansion of the rail, as shown in **Figure 4.8(c)**. In this case, the face at either end of the rail is assumed rigid. To achieve this, an additional 3D, thin, shell component is created at the rail ends that matches the rail cross section. A rigid body definition is used to associate translations at any point to the translation and rotations of the reference point, located at the centroid of the cross section. A longitudinal spring is then connected to the reference point of the rail shell and attached to a fixed horizontal ground surface. The stiffness, K, of the spring represents the axial stiffness of the rail in the far field calculated as a function of the cross-sectional area, A, the elastic modulus of steel, E, and a length parameter, L, as

$$K = \frac{AE}{L} \tag{17}$$

Partial constraint is then imposed by springs with a stiffness of K = 2.09*10^6 lb/in, assuming a cross sectional area, A = 12.95 in^2, modulus of elasticity, E = 29*10^6 psi, and length, L = 180". This simulates the infinite extents at either end of the rail that remain thermally unloaded. A surface-to-surface contact interaction is defined to tie the rigid rail shell to either end of the rail. The interaction is defined as a hard contact in the normal direction, and as frictionless contact in the tangential direction. In the interaction module, the shell element thickness is excluded, and the slave surface (rail) is adjusted to remove overclosure. At the reference point of this node, all translations, other than the longitudinal direction, along with all rotations, have been constrained. It is noted that the

applied constraints in the y and z directions do not prevent the translations of the rail component itself. However, they keep the rail end plates in place to properly engage and prevent the expected longitudinal expansion of the rail.

4.5.5 Thermal Boundary Conditions

Thermal boundary conditions are required for thermoelastic analysis; this entails defining the Dirichlet Boundary Condition (natural) and the Neumann Boundary Condition (essential). The Dirichlet Boundary Condition requires defining an initial temperature. The rail component is defined with an initial temperature of 0°F, also considered the RNT because it is assumed that at this arbitrary temperature, the rail is stress-free. The Neumann Boundary Condition requires an initial rate of heat transfer or heat flux. Initially no heat flux is applied to the model, and the rail is assumed thermally unloaded.

4.6 Load Conditions

The analysis type used determines the type of loading condition applied to the rail. In a statics analysis, a predefined temperature field is used to achieve the desired temperature fluctuations. Whereas, in a thermoelastic analysis, a surface heat flux is defined to subject the rail to a thermal loading.

4.6.1 Loading the General Static Model

In a statics analysis, a predefined temperature field is defined for the entire volumetric body of the rail. This temperature field value is based off the temperature changes observed in laboratory testing and dependent on the thermoelastic analysis temperature change imposed. Generally, an initial predefined field temperature of 0°F is defined, then

in the consecutive step, the predefined field is modified to the desired temperature. When running the General Static model, the following steps are defined:

1. *Initial Step:* This is the first step that Abaqus requires. While no analysis is completed throughout this step, it is typically used to define interactions, boundary conditions, and/or predefined fields before applying any loads. All surface interactions and/or tie constraints defined for the rail-fastener or rail-tie plate interface are activated in this initial step. The mechanical boundary conditions are applied: longitudinal constraint at the rail ends, lateral and longitudinal constraint at the tie plate reference points, and vertical constraint at the tie plates, dependent on if a TPC or TPS support condition is used. A predefined temperature field of 0°F is defined through direct specification, constant throughout the entire rail body.
2. *Thermal Loading:* At this step, the boundary conditions are propagated, and the rail is heated by modifying the predefined temperature field to a newly selected temperature. This temperature is applied to the entire rail component for various amplitudes per model. If only one temperature value is required, then this temperature is assigned a ramp amplitude loading. If data regarding the progression of temperature change is required, the loading can be discretized into time steps. For example, if a predefined temperature field of 100°F is applied, a tabulated amplitude loading could be defined for the load step, shown in: **Table 4.2**. With this tabulated loading, at time increment 0.5, half of the load amplitude

would be applied, 50°F, and these deformations are also computed in addition to deformations at 100°F.

Table 4.2: Amplitude loading

Time Step	Amplitude
0	0
0.5	0.5
1.0	1.0

4.6.2 Loading the Coupled Temperature-Displacement Model

In the coupled temperature-displacement model, a surface heat flux is used to apply the thermal loading to the entire outer rail surface, neglecting only the rail end faces and the bottom of the rail. The magnitude and region applied for this heat flux are varied throughout the parametric studies (see section **5.3**) depending on the desired temperature change. The surface heat flux value is selected based on the temperature change recorded in the lab. In the lab, the small-scale prototypes reached temperature changes of around 150°F. Through trial and error, different heat flux values are inputted until reaching temperature changes around this value. Because smaller volumes of rail are heated in the initial small-scale prototype tests, it is expected that the full-scale rail system will incur smaller temperature changes with the same heat intensity. A heat flux value of 50 (BTU/ in^2/s) is selected because this produces temperature changes in the rail web region of 120°F. All surface heat fluxes defined had a uniform distribution and an instantaneous amplitude loading unless discretized otherwise. When running the Coupled Temperature-Displacement model, the following steps are defined:

1. *Initial Step:* This is the first step that Abaqus requires. While no analysis is completed throughout this step, it is typically used to define interactions, boundary conditions, and/or predefined fields before applying any loads. All surface interactions and/or tie constraints defined for the rail-fastener or rail-tie plate interface are activated in this initial step. The mechanical boundary conditions are applied: longitudinal constraint at the rail ends, lateral and longitudinal constraint at the tie plate reference points, and vertical constraint at the tie plates, dependent on if a TPC or TPS support condition is used. The thermal boundary conditions are applied defining an initial zero temperature boundary condition and zero heat flux value.
2. *Thermal Loading:* In this step, the mechanical boundary conditions are engaged, and the thermal boundary conditions are deactivated. This step entails thermally loading the rail through a surface heat flux applied to the outer rail surface, neglecting only the bottom surface of the rail and outer rail ends.

Chapter 5. Parametric Studies

Parametric studies are conducted to investigate the impact of boundary conditions, analysis types, heating/cooling methods, rail geometry, tie spacing, and track stiffness have on the deformations and stress levels in rail. The key outputs for these studies are two-fold. The first set of outputs pertain to the shape and curvature profiles extended along the rail head and base flange. The rail shape profiles are extracted from Abaqus and curvature profiles are computed using the deformed shape profiles. Two regions of interest along these profiles are explored including between two consecutive ties or in the immediate region of the anchoring point. These outputs are used to investigate the type of deformations that should be expected in the rail subjected to a thermal loading. For the purposes of this study, *global flexure* is defined as typical beam flexure, where the *entire rail section* experiences bending about the neutral axis. This exists when bending stresses cause tension in the top fibers and compression in the bottom fibers of the rail, or vice-versa. *Local flexure* is defined as bending that exists in only a *part of the rail section*, for example the rail head, and is due to a nonuniform thermal expansion, and the corresponding stresses are in addition to the axial stress due to uniform thermal expansion. Local flexure may appear as bending that occurs between successive ties or about the anchoring point along either the rail head or base flange path. The rail head

and base are both analyzed as a means of determining which path produces the more measurable deformations for the proposed technology. All parametric studies are reference the baseline model that is presented first in this section. The in-depth Abaqus model description of the baseline model is detailed throughout **Chapter 4**.

5.1 Baseline Model

This baseline model is developed in Abaqus and considers the current track configuration and components of the indoor testing track found at USC. **Table 5.1** summarizes the characteristics of this track system for FE analysis. This baseline model is used as a reference to quantify and describe the behavior of these measurements, prior to altering these characteristics for the subsequent parametric studies. The shape profiles are initially extracted at the rail head and rail base, along paths A-A and B-B, respectively (see **Figure 5.1**). The curvature profiles are computed based on the deformed shape profiles. The longitudinal and transverse stain results are extracted from element A, (see **Figure 5.2**). The element selected is located at a distance 80" along the rail and at a height of 3.2" from the bottom surface of the rail; the centroidal height of a 132 RE rail cross section. Note that the location of this element is modified for different tie spacings and rail sizes, but still exists generally at the centroidal axis of the rail web and at the center point between the 4^{th} and 5^{th} tie location. This baseline model uses a surface heat flux value of 50 which produces uniform rail temperatures of 110°F, 93°F, and 116°F, along the rail head, rail base, and rail web, respectively.

Table 5.1: Summary of baseline model characteristics

Parameter	Value
Rail Size/Length	132 RE/180”
Number of Ties	9
Tie Spacing	20” (center-on-center)
Rail End Boundary Conditions	Longitudinally Constrained (x) Fixed Rotations
Tie Plate Support Type	Tie Plate Spring (y) Longitudinally/Laterally Constrained (x, z)
Tie Plate Type	Resilient Tie Plate General Track Modulus: 4,000 psi
Fastener System Inclusion	No
Analysis Type	Thermoelastic Analysis
Thermal Loading	Uniform Surface Heat Flux
Thermal Loading Surface Area	Entire outer rail surface, except for rail ends and bottom rail surface

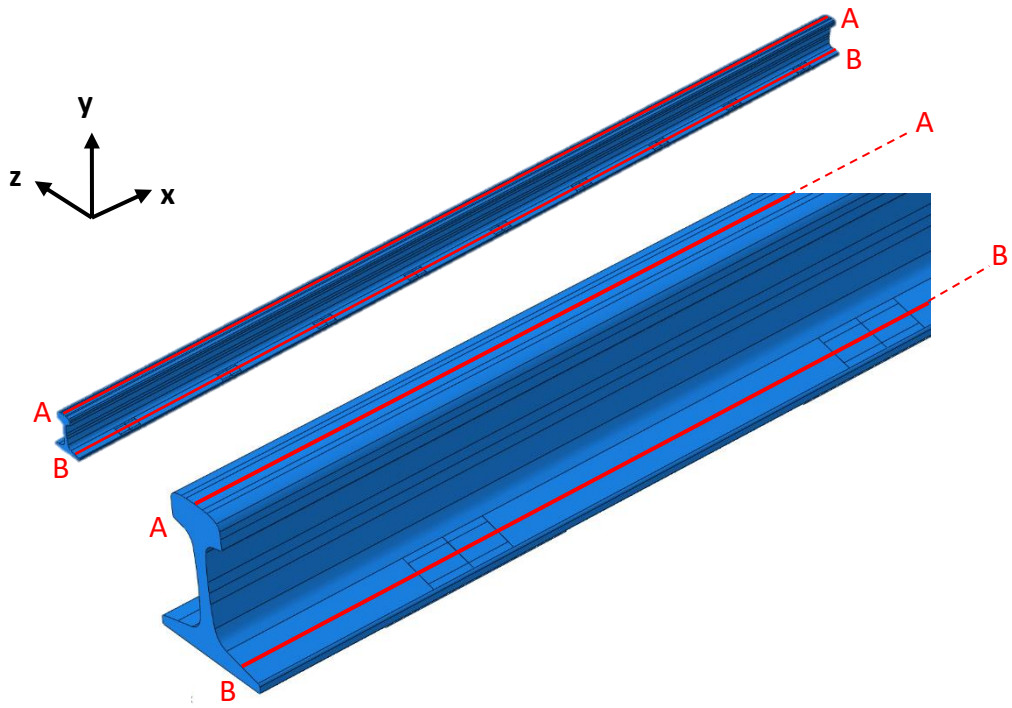

Figure 5.1: FE rail segment illustrating the paths that shape profiles are extracted along for analysis. Path A-A follows the center line of the rail head and Path B-B follows the center of the base flange.

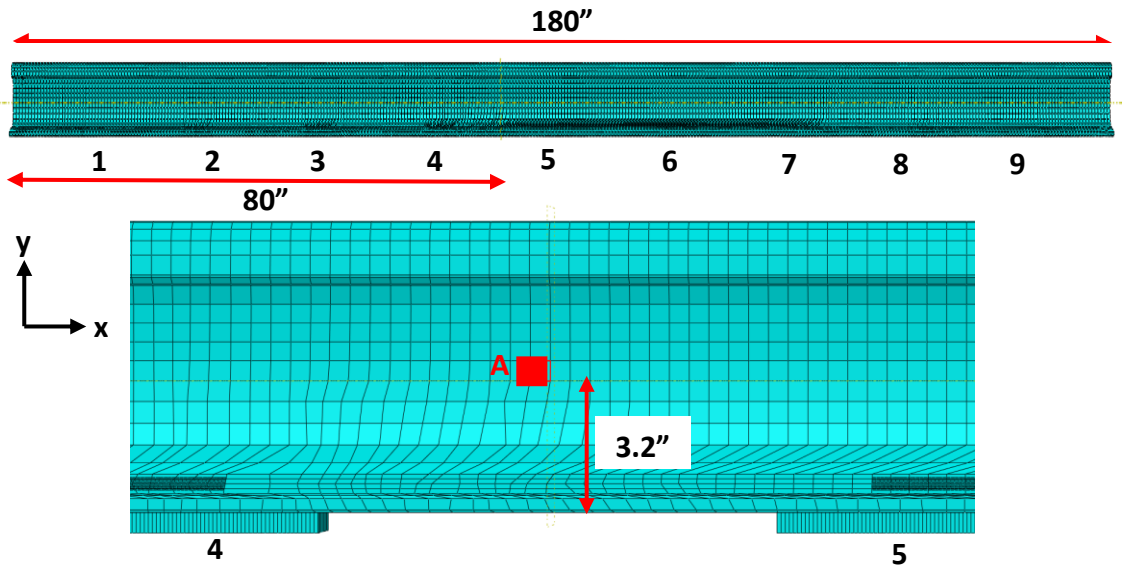

Figure 5.2: FE element A (red square) that is used to extract all longitudinal and transverse strain and stress measurements. The tie support locations are numbered in black along the rail.

5.1.1 Deformation Output – Baseline Model

The methodology for RNT estimation and stress computation assumes that non-uniform vertical expansion occurs throughout the duration of a thermal cycle between successive ties due to the boundary conditions that constrain the rail. **Figure 5.3** displays the shape and curvature profiles along the rail head and base. The shape profiles are depicted alongside the FE deformed rail shape for visualization. The rail head shape profile depicted in **Figure 5.3(a)** shows deformations ranging between approximately 175 µm and 178 µm at a rail head temperature of 110°F. While these deformations are well above the lower limit of accuracy for the StereoDIC system, the 3 µm change in deformation is relatively small and may be pose challenges concerning eliminating noise in captured measurements. The global maxima and minima of this profile exist at the center points between consecutive ties and at the anchoring points, as expected. The

shape profile along the rail base depicted in **Figure 5.3(b)** shows deformations ranging between approximately 14.5 μm and 22.6 μm at a rail base temperature of 93°F. In contrast to the rail head, this 8 μm change in deformation is larger and more desirable for minimizing potential problems with noise, but the deformations are much smaller and may be below the lower limit of accuracy of the StereoDIC system. The global maxima develop at the center points between two successive ties, while global minima develop at the edges of the rail seats. Alongside the deformed shape, the effects of the rigid rail seats are much more evident in the rail base due to this region being in the immediate region of the supports. Whereas along the rail head, only the anchoring points at the center of the rail seat can be clearly seen because of its distance away from the supports. At the anchoring point along the rail base, local maxima of approximately 21.0 μm develop. Therefore, the global maxima for both the rail head and base regions develop between two successive ties as opposed to about the anchoring point. In **Figure 5.3(c)**, the curvature profile along the rail head ranges between $-7.8*10^{-6}$ (1/in) to $4.6*10^{-6}$ (1/in). In the rail seat regions, the curvature values decrease, and local maxima of $2.6*10^{-6}$ (1/in) develop at the anchoring points. In contrast, between two successive ties, a more uniform behavior exists that allows the curvature to fully maximize without restraint from the rail seat conditions. In **Figure 5.3(d)**, the curvature profile along the rail base ranges between $-2.0*10^{-4}$ (1/in) to $2.0*10^{-4}$ (1/in). In the rail seat regions, the curvature decreases to approximately zero due to the rigid constraint that exists, while between two successive ties, local maxima of $-1.5*10^{-5}$ (1/in) develop.

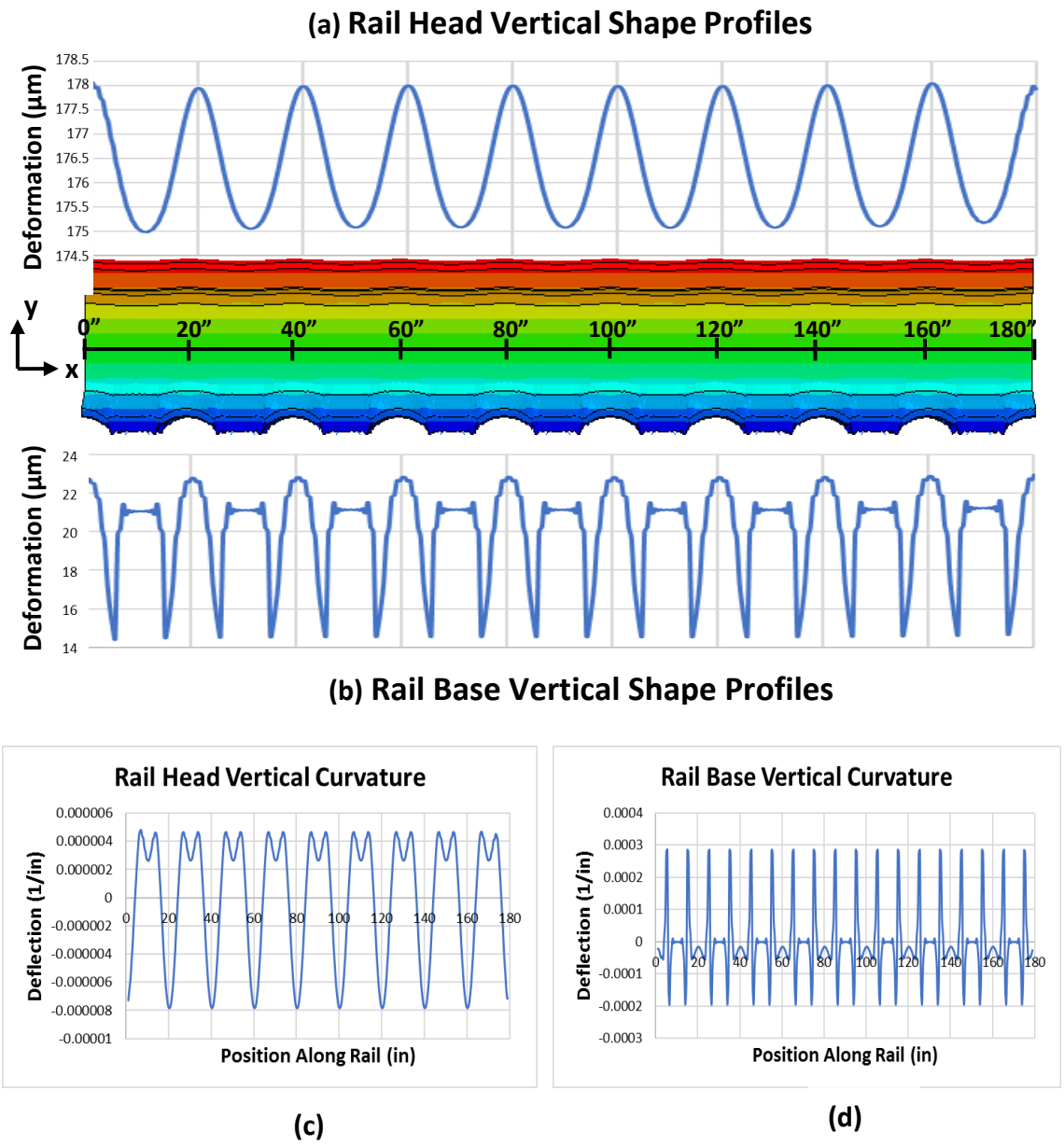

Figure 5.3: Baseline mode FE vertical deformation results with corresponding rail deformed shape (uniformly scaled at 10^3): (a) Rail head shape profile at T=110°F; (b) Rail base shape profile T=93°F; (c) Rail head curvature profile at T=110°F; (d) Rail base curvature profile at T=93°F

Therefore, the more advantageous region to capture shape deformations and curvature computations along the rail head and/or base is between two successive ties as opposed to about the anchoring points. This region produces more uniform

measurements that will yield a computed average curvature that is more accurate and representative of the data, upon curve fitting the shape deformations. Additionally, while the rail base is in the immediate region of the rigid constraints creating larger changes in deformations, these shape deformations are well below the rail head shape deformations. Therefore, the rail head path A-A appears to be the primary path for subsequent analyses. Nevertheless, parametric studies still investigate both the rail head and base paths for further exploration.

5.1.2 Strain Output – Baseline Model

Following the analysis on the rail head and base deformation profiles, the longitudinal and transverse strains are investigated. The proposed methodology also assumes that throughout a thermal cycle, the rail can freely deform in the transverse direction in the rail web region, while longitudinally, the strain depends directly on the level of constraint. The opposite relationship exists for stress, transversely the rail is considered stress free at this location while longitudinally, significant thermal stresses develop relative to temperature change. Strains are extracted from element A at the center cross section of the rail web between two successive ties as depicted in **Figure 5.2**. **Figure 5.4** displays the transverse and longitudinal stress and strain at element A for the baseline model.

Figure 5.4(a) plots the longitudinal and transverse stress in respect to temperature change. At a rail web temperature of 116°F, the FE computed transverse and longitudinal stress at this element are σ_Y = 0.13 ksi and σ_X = 22.9 ksi, respectively. The longitudinal thermal stress is significant and negative, decreasing linearly with

temperature change, indicating that the rail is in compression. Relative to the significant longitudinal stress, the transverse direction of stress is small and can be assumed stress free. **Figure 5.4(b)** plots the longitudinal and transverse strain in respect to temperature change. Relative to the transverse strain, the longitudinal strain is minimal and can be considered negligible. This is expected due to the longitudinal constraint defined by the boundary conditions in this model simulation. **Figure 5.4(c)** displays the transverse strain increasing linearly from (0°F, 0 $\mu\varepsilon$) to approximately (116°F, 1010 $\mu\varepsilon$). It appears that at this location, transversely the strain is not affected by the imposed boundary conditions and can freely deform. While relative to the transverse strain the longitudinal strain can be considered zero. **Figure 5.4(d)** displays the longitudinal strain decreasing from (0°F, 0 $\mu\varepsilon$) to approximately (116°F, -12.7 $\mu\varepsilon$).

An analysis is performed to investigate why the longitudinal strain is slightly negative as opposed to zero. Data is extracted along a vertical line depicted as path C-C in **Figure 5.5** at the center cross section of the rail at a distance (D) = 80", the center between two successive ties. Additional data is extracted at D=78" and D=76" to observe the changes of the strain distribution at rail cross sections closer to the support. **Figure 5.5(a)** and **Figure 5.5(b)**, plot the y-coordinate of the rail as a function of the longitudinal strain and stress at these three locations. Only a portion of the height of the rail is shown (2.5" to 6.5" from the bottom of the rail) to focus this analysis on the web region. **Figure 5.5(a)** shows that the actual point of zero longitudinal strain is closer to a height of 6", as opposed to at centroidal axis, 3.2" from the bottom of the rail. This suggests that bending is occurring in this region of the rail in addition to axial. In **Figure 5.5(b),** the negative

stress values indicate compression. It is also observed that at cross sections closer to the support, the flexure effects are decreasing, and the axial effects are predominant. Therefore, this bending is a result of the boundary conditions found at the tie supports, which are causing this negative strain at the centroid to occur. However, while this negative strain exists, it is negligible relative to the transverse strain, and can be considered zero.

(a)

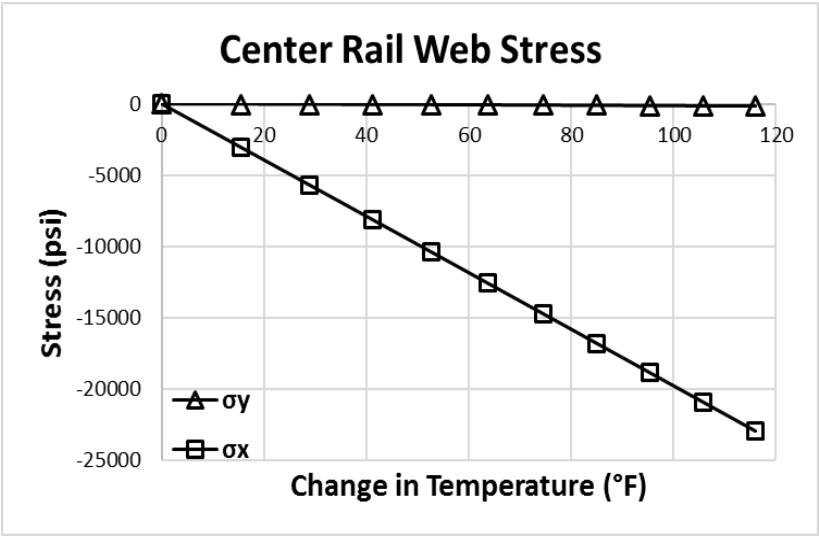

(b)

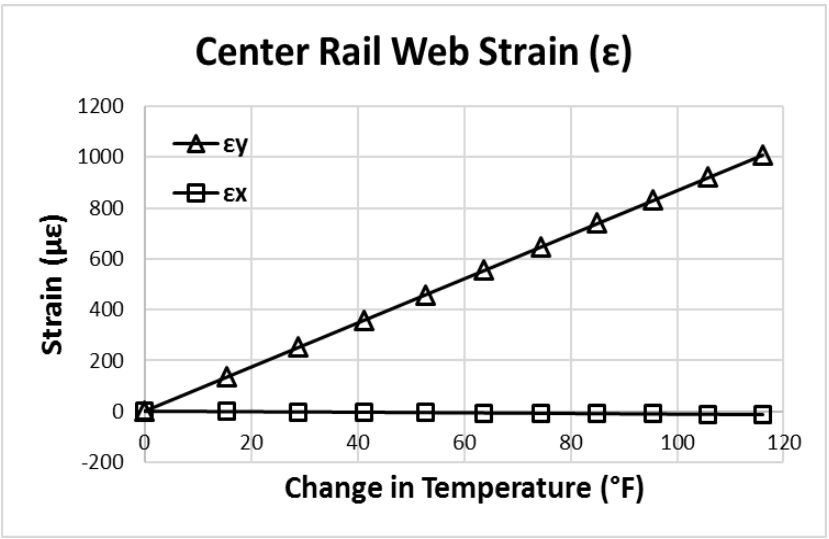

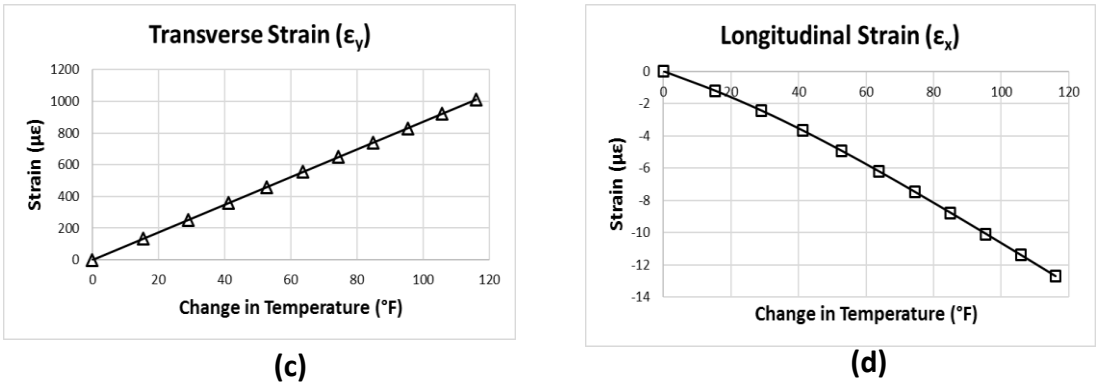

Figure 5.4: Plots of the baseline model data extracted at element A in respect to temperature change: (a) Transverse and longitudinal stress; (b)Transverse and longitudinal strain; (c) Transverse strain; (d) Longitudinal strain

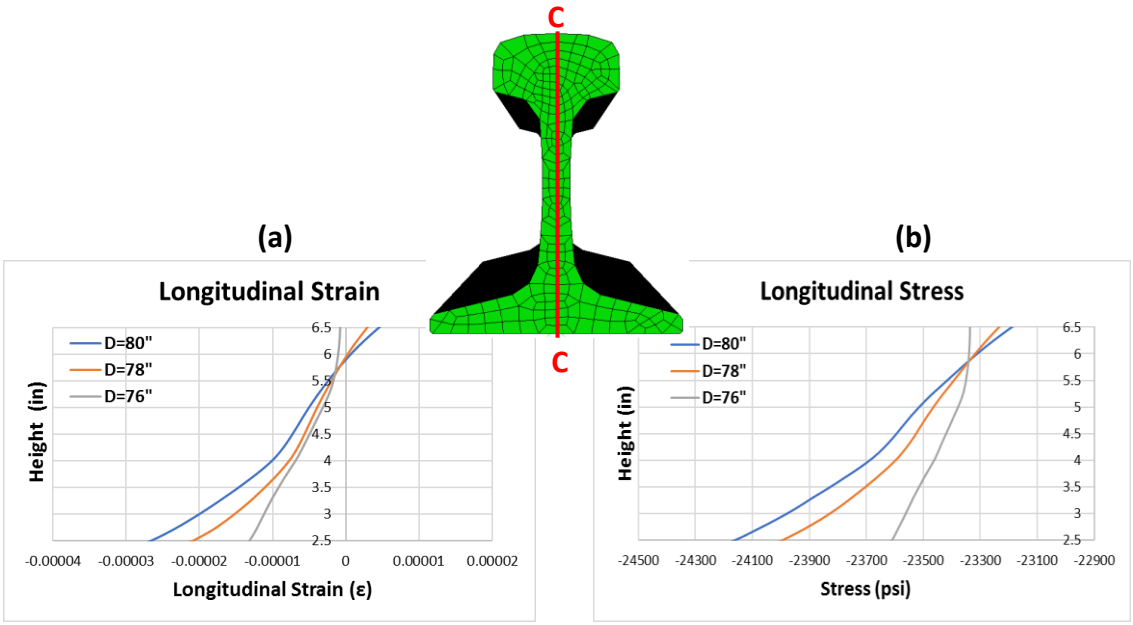

Figure 5.5: Plots of the FE analysis regarding the negative measurements acquired along path C-C at a rail temperature change of ΔT=120°F: (a) Longitudinal strain profile; (b) Longitudinal stress profile

5.1.2.1 FE Negative Strain in View of Experimental Measurements

The acquired longitudinal strain data captured by the StereoDIC system is then considered for the partially constrained specimen. In **Figure 5.6(a)**, the longitudinal strain profile at different rail temperatures is depicted. The non-uniform temperature

distribution influence on strain is evident in the variations of shape that exist in the profiles at different rail temperatures. Instead of maintaining a constant shape that increases in magnitude with temperature increase, different regions on the rail expand at different rates as the heat propagates throughout the rail cross section. This confirms that the eccentric thermal loading technique influences the potential bending of the rail between supports. Additionally, in **Figure 5.6(b)**, the strain profile along the rail web is plotted at the rail mid-length, 8”, and at a cross section closer to the support at 6”. These two profiles appear to be overlapping one another at similar strain values, while slightly different behavior in the profiles exists with these two sections, due to the eccentric thermal loading. The relationship between these two profiles indicates that the fabricated supports are not inducing much bending in the web region of the rail. This is expected because this specimen is considered partially constrained at the entire cross section, so the rail can expand at similar rates along its length, in contrast to the FE simulation that acquires measurements between supports where the rail is constrained only at its base.

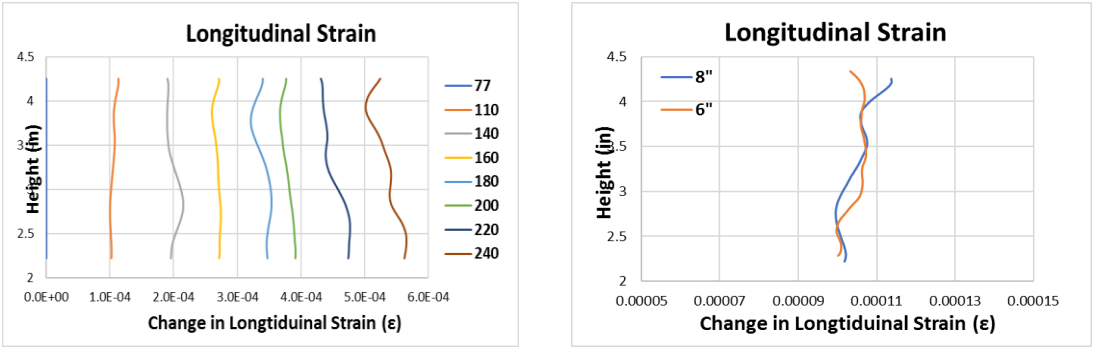

Figure 5.6: Plots of StereoDIC captured ε_x along a vertical line through the rail web: (a) Longitudinal strain profile at a cross section for different temperatures; (b) Longitudinal strain profile at different cross sections distances for T=110°F

5.2 Effects of Boundary Conditions

This initial parametric study is critical in determining the effects that the boundary conditions have for the studies to follow. Three different boundary conditions are investigated for this parametric study:

(i) the way the rail ends are supported,

(ii) the way the tie plates are supported, and

(iii) the effects of the fastener system

The combinations of the various boundary conditions led to the analysis of seven cases. To uniquely identify each combination, a model ID is assigned to each model. The general format is RailBC-TiePlateBC#. RailBC takes the values C=Constrained, P=Partially constrained (elastically constrained) and F=Free (unconstrained). TiePlateBC takes the values TPC = vertical constrained supports and TPS= vertical spring supports. The # symbol takes the value of 0 or 1, depending if the fastener system is included (#=1) or not (#=0). **Table 5.2** summarizes the model types with their corresponding Model ID. The rail is modeled for thermoelastic analysis and follows the baseline model described in section **5.1**.

Table 5.2: Model IDs with their corresponding boundary conditions

Model ID	Rail End BC	Tie Plate Support	Fastener System
C-TPR0	Constrained	Tie Plate Constrained	No
C-TPS0	Constrained	Tie Plate Spring	No
C-TPS1	Constrained	Tie Plate Spring	Yes
P-TPR0	Partially Constrained	Tie Plate Constrained	No
P-TPS0	Partially Constrained	Tie Plate Spring	No
F-TPR0	Free	Tie Plate Constrained	No
F-TPS0	Free	Tie Plate Spring	No

5.2.1 Fastener System Study

The effects of the inclusion of the fastener system are initially investigated by comparing the following models: C-TPR0, C-TPS0, and C-TPS1, which simulate the three different boundary conditions located at the anchoring points. These models are a derivative of the baseline model modifying only the boundary conditions at the anchoring points. An analysis is performed on the rail head and base shape deformation and curvature profiles, along with the rail web longitudinal and transverse strain values.

5.2.1.1 Deformation Output – Fastener System

It is presumed that local flexure is induced due to the boundary conditions defined throughout a thermal loading. This first study analyzes the differences in the shape and curvature profiles upon variation of the boundary conditions defined at the anchoring point, more specifically, the inclusion of the fastener system. Model IDs denoted with a 1 include the fastener system and 0 do not include the fastener system. **Figure 5.7** displays the shape and curvature profiles along the rail head and base of the constrained rail to compare the different anchoring point boundary condition cases.

In **Figure 5.7(a)** and **Figure 5.7(b)**, the shape and curvature profiles along the rail head path A-A are displayed. In **Figure 5.7(a)**, the shape profiles are insignificantly affected by the anchoring point boundary condition and follow the baseline model results. When the fastener system is employed, the deformations tends to be less uniform throughout the profile. This is due to the spring connection allowing some unsymmetrical uplift in the anchoring point regions. In contrast, the deformations of the two models without the fastener system are identical. This trend is also prevalent in the curvature

profiles. In **Figure 5.7(b)**, the curvature profile along the rail head is minimally affected by the anchoring point boundary condition. When the fastener system is employed, slight variations exist that are very small and are considered negligible. Overall, the inclusion of fasteners has insignificant effects on the shape and curvature profiles along the rail head region.

In **Figure 5.7(c)** and **Figure 5.7(d)**, the shape and curvature profiles along the rail base path B-B are displayed. The effects of the fastener component are more evident along the rail base path due to this region being in the immediate region and apparent intersection with the fastener system. **Figure 5.7(c)** shows that all shape profiles produce the same global maxima and minima that exist with the baseline model at the center between successive ties and at the edges of the rail seats. The difference in profiles exists within the rail seat region because this is also where the fastener system is defined. When the fastener system is not included, both models produce an identical behavior and local maxima of approximately 21.0 μm develop in the rail seat regions. When the fastener system is included, the local maxima decrease approximately 3-4 μm within the fastener region. This decrease is not constant throughout all fastener system regions because of the unsymmetrical uplift that the elastic springs allow. However, because the global maxima and minima are not affected by the inclusion of the fastener system, the difference in the shape profile is considered insignificant. In **Figure 5.7(d)**, the curvature profile along the rail base is also not significantly affected by the anchoring point boundary conditions. Slight differences exist due to the unsymmetrical uplift, but these differences are considered negligible. Overall, the inclusion of the fastener systems has

insignificant effects on the deformed shape and curvature profiles along the rail base region.

5.2.1.2 Strain Output – Fastener System

Following the rail head and base deformation analysis, the effects that inclusion of the fastener system have on the rail web thermal strains between consecutive ties are investigated. Throughout a thermal loading it is assumed that at this location, transversely, the rail is not affected by the level of constraint imposed by the boundary conditions, while longitudinally, the strain depends directly on this level of constraint. All data is extracted from element A at the center cross section of the rail web between two successive ties. **Figure 5.8** plots the transverse and longitudinal strain at this element for the models under investigation (C-TPR0, C-TPS0, C-TPS1).

Figure 5.8(a) displays the transverse strain for all models increasing linearly with temperature change at the same rate as the baseline model. This confirms that at this location, the transverse strain is not affected by the level of constraint defined at the anchoring point. In **Figure 5.8(b)**, the longitudinal strain displays slight variations with the model that includes the fastener system. The models that do not include the fastener system have longitudinal strains that decrease at the same rate as the baseline model to (116°F, -12.7 $\mu\varepsilon$), while the model that includes the fastener system strains decreases to (116°F, -11.5 $\mu\varepsilon$). The slight difference in the C-TPS1 model may be due to the tie plate and fastener system connection with the rail (see section **4.5.2**). Models that do not include the fastener system, fully tie the rail to the tie plate, whereas, the model that includes the fastener system, a surface-to-surface contact interaction is defined between

the rail interface with the tie plate and fastener system. This interaction defines a tangential frictional surface which decreases the level of longitudinal constraint at the anchoring point, leading to a decrease in the strain. However, the longitudinal strain in all models is very small compared to the transverse strain and can therefore be considered negligible.

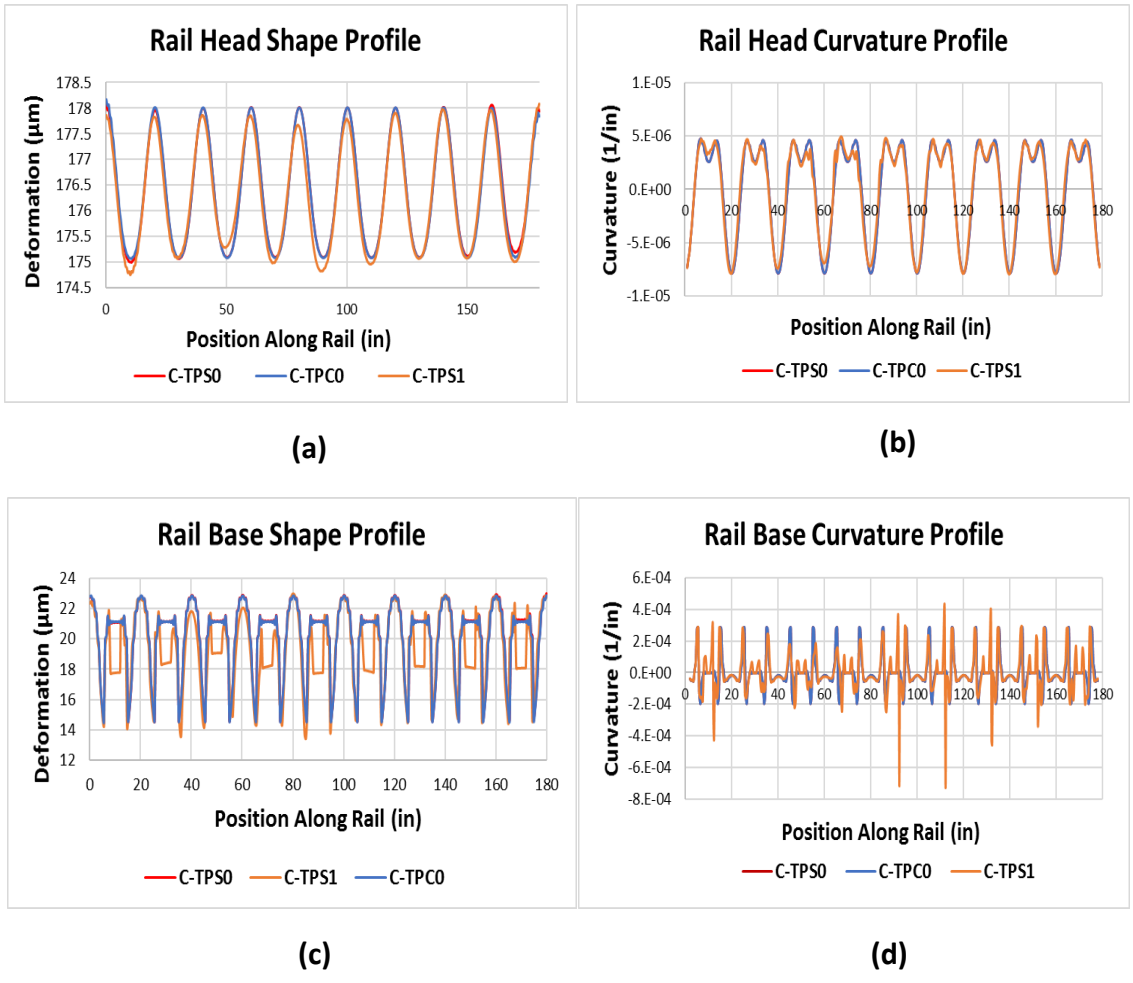

Figure 5.7: Plots of FE deformations with respect to position along the rail to investigate the effects of including the fastener system: (a) Rail head shape profiles; (b) Rail head curvature profiles; (c) Rail base shape profiles; (d) Rail base curvature profiles

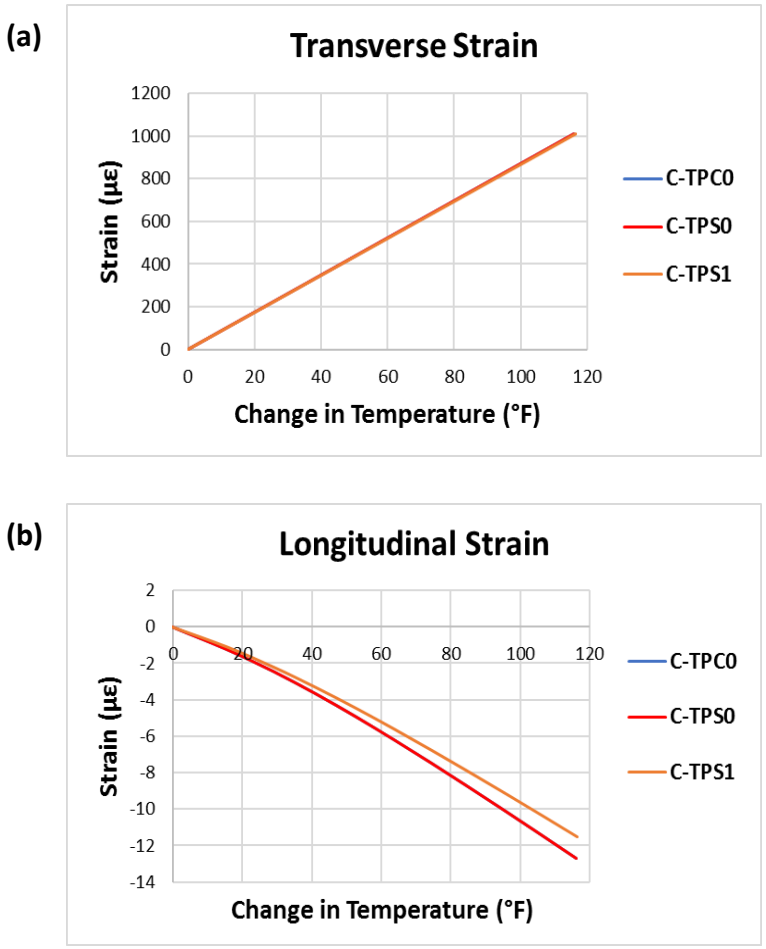

Figure 5.8: Plots of FE strains with respect to temperature change to investigate the effects of including the fastener system: (a) Transverse strain; (b) Longitudinal strain

5.2.2 Rail Boundary Conditions Study

Throughout a thermal loading, the effects of the boundary conditions defined at the rail ends and at the tie plate supports are investigated by comparing the following models: C-TPR0, C-TPS0, P-TPR0, P-TPS0, F-TPR0, and F-TPS0 (see **Table 5.2** for model details). The rail end boundary conditions considered are the longitudinally constrained (C), partially constrained (P), and free (F) rail ends. The tie plate support conditions considered are the tie plate constrained support (TPC) and a tie plate spring support (TPS).

The baseline model only modifies the boundary conditions for this study. An analysis is performed on the rail head and base shape and curvature profiles, along with the rail web longitudinal and transverse strain values.

5.2.2.1 Deformation Output – Boundary Conditions

The thermal deformations that develop due to the defined boundary conditions are initially investigated along the rail head path A-A. **Figure 5.9(a)** and **Figure 5.9(b)** display the shape and curvature profiles for the models with TPS supports and all levels of rail end constraint (C-TPS0, P-TPS0, and F-TPS0), and **Figure 5.9(c)** and **Figure 5.9(d)** display the shape and curvature profiles for the models with TPC supports and all levels of rail end constraint (C-TPC0, P-TPC0, and F-TPC0). **Figure 5.9** displays only a portion of the entire 180-inch rail length to focus this analysis on solely the center five tie support locations (40” to 140”) to ignore the unrealistic rail end effects. This is done because in the field the minimum length of a CWR segment is 4,800” (Federal Railroad Administration 2019), whereas this segment under analysis is much shorter and the rail end effects can therefore be ignored. Future experimental procedures also plan to capture measurements between the center tie support locations of the full-scale prototype to ignore these effects.

In **Figure 5.9(a),** the models with TPS supports and varying rail end constraints (C-TPS0, P-TPS0, and F-TPS0) are shown for analysis regarding the rail head deformed shape profiles with elastic tie supports. The shape deformations are affected by the level of rail end constraint in the following manner: the lower the level of constraint, the higher the rail head deformations. The unconstrained and partially constrained support conditions

produce global flexure in the rail and the local effects are not evident. The parabolic profile shape of these two cases have a global maximum that decreases with an increase in the level of constraint. The unconstrained and partially constrained support cases have a global maximum of 1950 µm and 580 µm, respectively. This is expected due to the elastic springs beneath the rail that allow the rail to extend vertically. In contrast, the constrained case induces local flexure between two successive ties that is also found with the baseline model, more clearly shown in **Figure 5.7(a).** The curvature behavior similarly follows the trend observed in the shape profiles. In **Figure 5.9(b)**, the curvature increases when there is a decrease in the level of rail end constraint. The curvature profile of the constrained case has the same peaks observed in the baseline model, while the unconstrained and partially constrained support cases have curvature peaks constantly changing throughout the rail. As the unconstrained and partially constrained support profiles near the center tie support, they are approaching the curvature values produced in the constrained case, but never fully converge to the constrained case behavior.

In **Figure 5.9(c),** the models with TPC supports and varying rail end constraints (C-TPC0, P-TPC0, and F-TPC0) are shown for analysis regarding the rail head deformed shape profiles with constrained tie supports. Unlike the TPS support models, the TPC support is fully constraining the vertical expansion at the tie locations, resulting in a different deformation behavior. In these models, the deformations are affected by the level of rail end constraint in the following manner: the lower the level of rail end constraint, the larger deformations are in the rail ends, away from the center tie location. The constrained case induces local flexure between two successive ties identical to the

constrained TPS support behavior and baseline model. The unconstrained and partially constrained support cases produce local flexure, unlike the TPS support models, with initially larger changes in deformation because of the decrease in the level of rail end constraint. As these two cases approach the three center tie locations, they fully converge to the shape profile of the constrained case. The curvature behavior similarly follows the trend observed in the shape profiles. In **Figure 5.9(d)** it is shown that a decrease in the level of rail end constraint, causes differences in the initial changes in curvature in the rail end regions. The curvature profile of the constrained case has the same peaks observed in the baseline model, while the unconstrained and partially constrained support cases have curvature peaks changing throughout the rail. As the unconstrained and partially constrained support cases approach the center tie support, both profiles fully converge to the constrained case curvature profile.

After analysis of the rail head, the thermal deformations that develops due to the defined boundary conditions are investigated along the rail base flange path B-B. The shape and curvature profiles are displayed in **Figure 5.10(a)** and **Figure 5.10(b)** for the models with TPS supports and all levels of rail end constraint (C-TPS0, P-TPS0, and F-TPS0), and **Figure 5.10(c)** and **Figure 5.10(d)** for the models with TPC supports and all levels of rail end constraint (C-TPC0, P-TPC0, and F-TPC0). **Figure 5.10** displays only a portion of the entire 180-inch rail length to focus this analysis on solely the center five tie support locations (40” to 140”) to ignore the unrealistic rail end effects.

In **Figure 5.10(a),** the models with TPS supports and varying rail end constraints (C-TPS0, P-TPS0, and F-TPS0) are shown for analysis regarding the rail base shape profiles

with elastic tie supports. The shape and curvature profiles along the rail base flange similarly follow the trends found along the rail head. The shape deformations are affected by the level of rail end constraint in the following manner: the lower the level of constraint, the larger the deformation values. The unconstrained and partially constrained support cases produce global flexure in the rail and the local effects between two successive ties are not evident. The parabolic profile shapes for these two cases have a global maximum that decreases with an increase in the level of constraint. The unconstrained and partially constrained support cases have a global maximum of 1800 μm and 426 μm, respectively, slightly lower than the rail head maximum values. This is expected due to the being in the immediate region of the elastic springs beneath the rail that allow the rail to extend vertically. In contrast, the constrained case produces local flexure between successive ties that is found in the baseline model, more clearly shown in **Figure 5.7(c).** The curvature profiles similarly follow the trend observed in the shape profiles. In **Figure 5.10(b)**, the curvature profiles vary between the different rail end constraint cases, but differences are relatively small compared to the differences observed along the rail head. The curvature profile of the constrained case has the same peaks observed in the baseline model, while the unconstrained and partially constrained cases have curvature peaks changing throughout the rail. As the unconstrained and partially constrained cases near the center tie location, they are approaching curvature values found with the constrained case, but never fully converge to this case.

In **Figure 5.10(c),** the models with TPC supports and varying rail end constraints (C-TPR0, P-TPR0, and F-TPR0) are shown for analysis regarding the rail base deformed

shape profiles with constrained tie supports. Unlike the TPS support models, the TPC support is fully constraining the vertical deformations at the tie locations, resulting in a different shape profile behavior. In these models, the shape profile is affected by the level of rail end constraint in the following manner: the lower the level of constraint, the larger the deformations are in the rail ends, away from the center tie location. The constrained case induces local flexure between two successive ties, identical to the constrained TPS support behavior and baseline model. The unconstrained and partially constrained support cases produce local flexure, unlike the TPS support models, with differences that exist only in the rail end regions. As the unconstrainted and partially constrained support cases near the center tie location, they fully converge to the constrained case shape profile. In **Figure 5.10(d)**, the curvature profile is approximately the same for all constraint cases. The curvature for all TPC support cases is identical to the curvature behavior of the constrained TPS support case and the baseline model.

It can be concluded that the rail head and rail base flange produce the same shape and curvature profile trends, except with the differences in values. The constrained rail end conditions produce identical shape and curvature profiles for the TPS and TPC supports. Therefore, if the rail is fully constrained longitudinally at the rail ends, the tie plate support condition does not affect the shape or curvature measurements. When observing the TPS support models, the unconstrained and partially constrained rail end support cases produce global flexure along the rail, and the local effects are no longer evident, and thus, the deformations are not practical. In contrast, when observing the TPC supports, the unconstrained and partially constrained rail end conditions produce local

flexure between two successive ties. The shape and curvature profiles initially vary from the constrained case in the rail end regions, but as the center tie location is approached, both cases fully converge to the behavior of the constrained TPC rail. Therefore, if the rail is fully constrained vertically at the tie supports and measurements are captured at the center region of the rail, the level of rail end constraint does not affect the shape and curvature results.

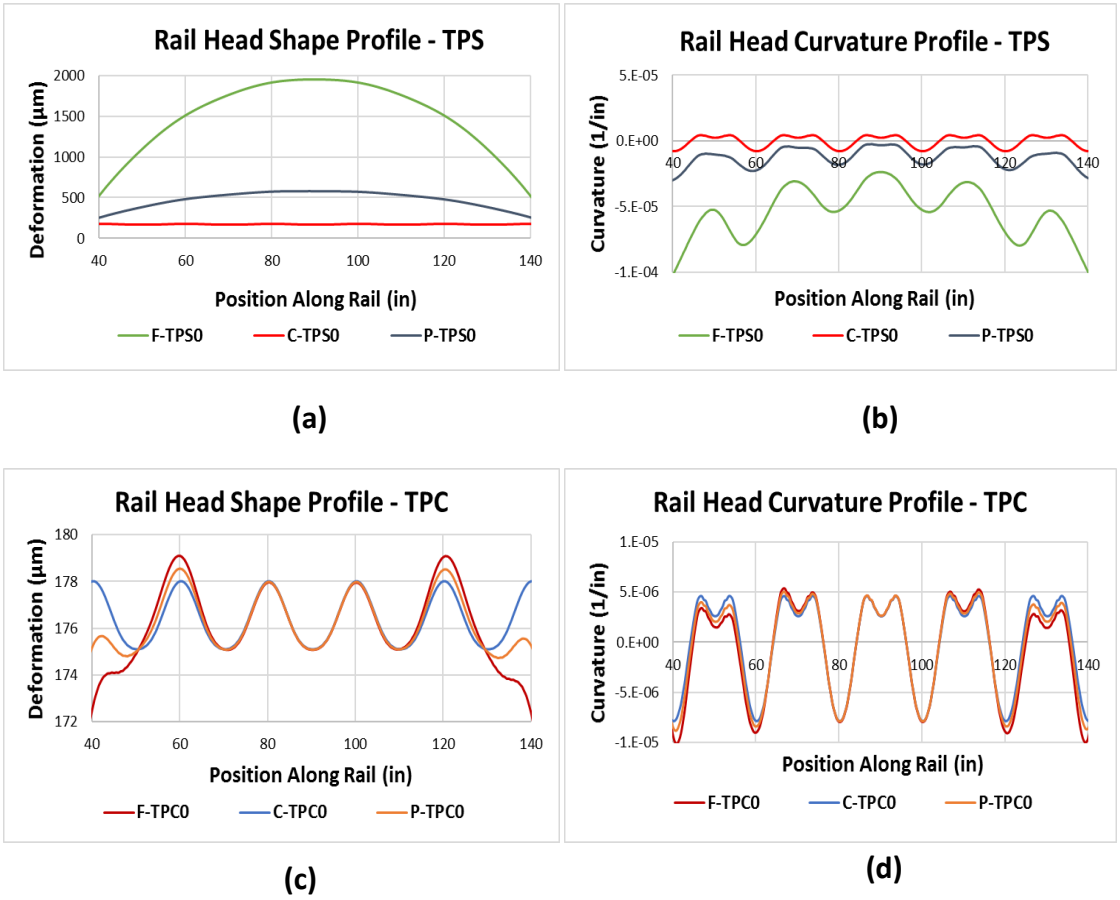

Figure 5.9: Plots of FE deformations with respect to position along the rail to investigate the effects of boundary conditions along the rail head: (a) Shape profiles with TPS supports; (b) Curvature profiles with TPS supports; (c) Shape profiles with TPC supports; (d) Curvature profiles with TPC supports

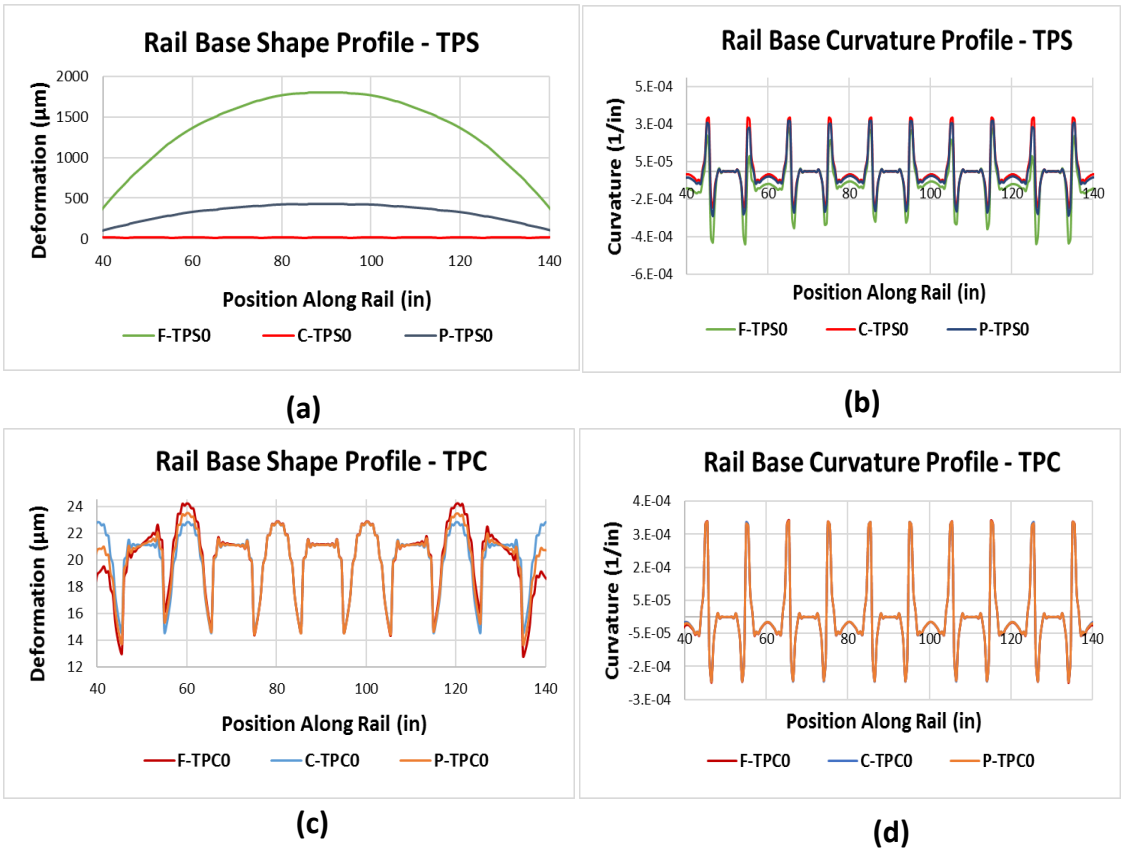

Figure 5.10: Plots of FE deformations with respect to position along the rail to investigate the effects of boundary conditions along the rail base: (a) Shape profiles with TPS supports; (b) Curvature profiles with TPS supports; (c) Shape profiles with TPC supports; (d) Curvature profiles with TPC supports

5.2.2.2 Strain Output

Following the rail head and base deformation analysis, the effects of boundary conditions on the rail web thermal strains are investigated. Throughout a thermal loading it is assumed that at the center web region between consecutive ties, transversely, the rail is not affected by the level of constraint imposed by the boundary conditions, while longitudinally, the strain depends directly on this level of constraint. All data is extracted from element A at the center cross section of the rail web between two successive ties. **Figure 5.11** plots the transverse and longitudinal strain at this element for all TPS and TPC

support models with the varying levels of rail end constraint (C-TPS0, C-TPC0, P-TPS0, P-TPC0, F-TPS0, F-TPC0).

Figure 5.11(a) displays the transverse strain for all models increasing linearly with temperature change at the same rate as the baseline model with minimal differences. The insignificant differences are exhibited with the F-TPS0 and P-TPS0 models but are small and considered negligible. This confirms that at this location, the transverse strain is not affected by the level of constraint at the rail ends or at the tie supports. **Figure 5.11(b)** displays differences in longitudinal strain dependent on the defined boundary conditions. All TPC support models (C-TPC0, F-TPC0, P-TPC0) produce identical strains found with the baseline model for all rail temperatures regardless of the rail end constraint. In contrast, the TPS support models produce different longitudinal strain values per the level of rail end constraint. The unconstrained case (F-TPS0), produces longitudinal strains that increase with temperature to approximately (116°F, 133 $\mu\varepsilon$). The partially constrained case (P-TPS0) produces a behavior that is bounded by the other two TPS rail end constraint cases. The longitudinal strains increase with temperature to approximately (116°F, 20 $\mu\varepsilon$). Finally, the fully constrained case (C-TPS0) and all TPC support models produce longitudinal strains that decrease with temperature to approximately (116°F, -12 $\mu\varepsilon$); the behavior that exists with the baseline model. Therefore, with an increase in the rail end level of longitudinal constraint, there is an increase in the longitudinal strain for the TPS support models, while the TPC support longitudinal strain is not affected by the rail end level of longitudinal constraint

(a)

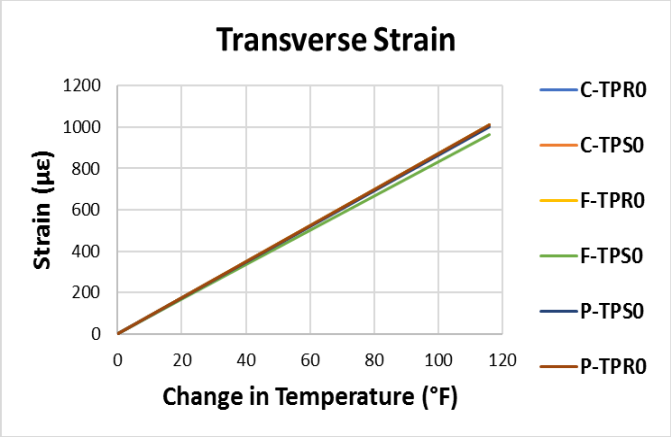

(b)

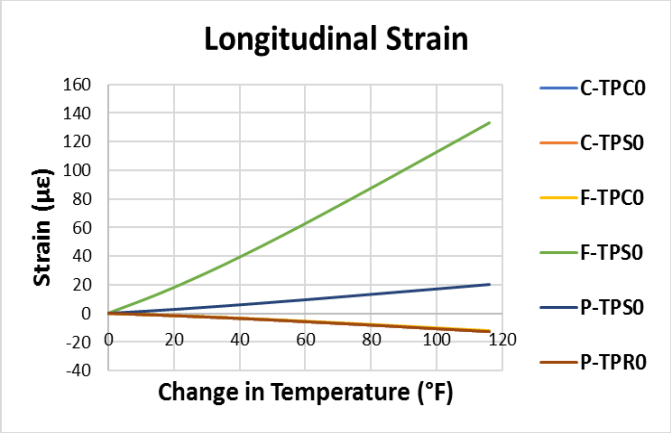

Figure 5.11: Plots of FE strains with respect to temperature change to investigate the effects of boundary conditions: (a) Transverse strain; (b) Longitudinal strain

The strain and deformation profiles are in agreement with each other, because at this location between the 4th and 5th tie support, the TPC deformation profiles have converged to the constrained case, thus, identical strains for all cases. In contrast, at this same location, the TPS deformation profiles can expand more in both directions with a decrease in the level of constraint, thus, an increase in strain. In conclusion, the transverse strain is not affected by the level of constraint imposed by either of the defined boundary conditions. Additionally, the TPS support models confirm the second hypothesis that different levels of longitudinal constraint at the rail ends, impact the longitudinal strain

found at a center rail web element. Whereas, when the rail is perfectly constrained vertically at the tie support locations, the longitudinal strain is not affected and follows the behavior of the constrained rail end case. It is also observed, however, that the longitudinal strain in all constrained and partially constrained models is very small compared to the transverse strain and can be considered negligible. In the unconstrained case, while longitudinal strains may not be considered negligible, they are still small relative to the transverse strain and these support conditions are impractical.

5.2.3 Discussion and Conclusions of the Rail Boundary Conditions Parametric Study

Upon completion of the boundary condition studies, the following conclusions are made:

- The shape and curvature along the rail head and rail base flange show similar trends. While the rail head produces larger shape deformations, the rail base produces higher changes in deformations.
- Inclusion of the fastener system produces negligible differences in shape, curvature, and strain in the rail head, base, and web, thus, the fastener system could be omitted.
- Shape and curvature measurements are not affected by either (i) the tie plate support when the rail is fully constrained longitudinally at the rail ends, or (ii) by the level of longitudinal constraint at the rail ends, provided that the rail is fully constrained vertically at the tie supports.

- The unconstrained and partially constrained rail end cases with TPS supports produce global flexure along the rail, while the TPC supports produce local flexure between two successive ties.
- The transverse strain is not affected by the level of constraint at the rail ends or at the tie plate support locations.
- The TPS support models confirm that different levels of longitudinal constraint effect the longitudinal strain produced at the rail web. In contrast, the longitudinal strains that develop in TPC models are not affected by the level of constraint at the rail ends.
- The longitudinal strain for all practical models is very small compared to the transverse strain and can be considered negligible.

In conclusion, future construction of the indoor testing track prototype system must either fully constrain the rail longitudinally at the ends or fully constrain the rail vertically at the tie supports to obtain a realistic track system that adequately simulates the constraints found on a full-length CWR in the field. If this level of constraint is ensured, in the central rail web region the longitudinal strain can always be considered negligible, while the transverse strain is significant and not dependent on these boundary conditions.

5.3 Effects of Thermal Loading Method

Various thermal techniques are being considered to guide how the rail specimen will be heated for future laboratory testing procedures. Throughout this study different heating methods are investigated. Initially a preliminary study is conducted to investigate

the differences that exist between performing a static analysis as opposed to a thermoelastic analysis. Following the preliminary study, the effects of heating different surface areas on the rail are investigated through thermoelastic analyses. Lastly, an additional study is performed for a deeper exploration of a trend observed in the preliminary and primary study regarding the heating surface area. The baseline model is modified to reflect the different analysis types and heating surface areas used throughout this study.

5.3.1 Preliminary Study – Analysis Type

This preliminary study is conducted to investigate the differences that exist between performing a static analysis or a thermoelastic analysis by using different Abaqus model solvers. A statics analysis uses the general statics solver and defines predefined temperature fields to subject the rail to temperature change. This analysis does not capture the effects of heat flow throughout a rail cross section because the predefined temperature fields heat the entire volumetric body simultaneously, as shown in **Figure 5.12(a).** Due to the simplicity of this approach, it is used as a benchmark for the subsequent thermoelastic analyses. A coupled temperature-displacement model solver is used for thermoelastic analysis. This analysis applies a surface heat flux to the outer rail surface. In this case, the surface heat flux is applied to the entire outer rail surface, neglecting only the rail end faces and the bottom rail surface. This is to simulate the regions of the rail that are directly exposed to the sun as it heats CWR in the field. This technique captures the non-uniform heat flow effects as heat travels throughout the rail cross section during a thermal cycle, as shown in **Figure 5.12(b)**. This study initially

compares the shape and curvature profiles at similar temperatures along the rail head and base, followed by strain analysis at the center rail web.

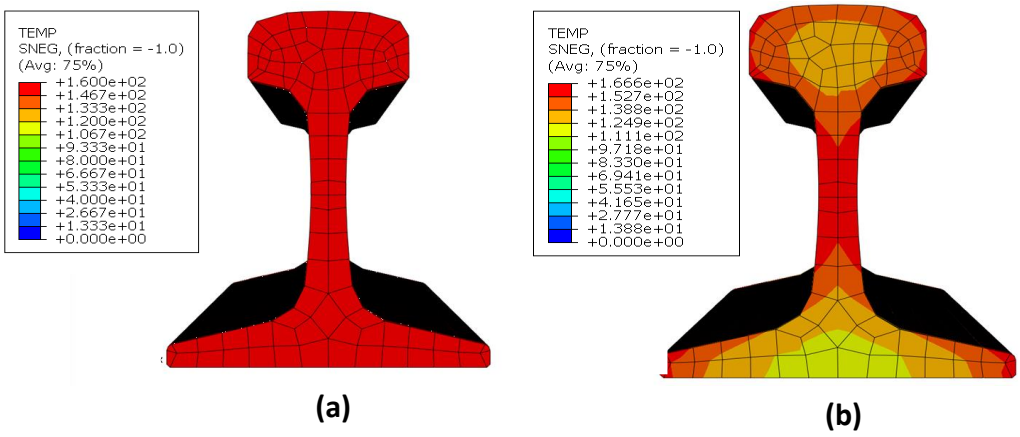

Figure 5.12: FE visualization of analysis types with temperature field superimposed on rail cross section: (a) Predefined temperature field technique; (b) Surface heat flux technique

5.3.1.1 Deformation Output – Analysis Type

In the thermoelastic analysis a surface heat flux (HFL) is applied to the outer surface of the rail to impose the thermal loading. The baseline model is considered, which uses a heat flux value of 50 (BTU/ in2/s), producing a uniform temperature along the rail head path A-A and base path B-B of 109.5°F and 92.8°F, respectively. The rail head and base deformed shape profiles are extracted for analysis and curvature profiles are computed. Subsequently, the statics model is run with two iterations. Initially, a predefined temperature field (PDF) defines a rail temperature of T = 109.5°F, and the rail head shape profile is extracted. Following this, the predefined temperature field is modified to a rail temperature of T = 92.8°F, and the rail base shape profile is extracted. The two iterations are completed so that the two model types could then be compared with similar temperatures, accordingly. Curvature profiles are then computed from the

shape profiles. **Figure 5.13** plots the rail head and base shape and curvature profiles for both heating types.

In **Figure 5.13(a)** and **Figure 5.13(c)**, the PDF and HFL techniques deformed shape profiles are displayed for analysis along the rail head and base . It is evident that the PDF technique produces slightly higher shape deformations and changes in deformations compared to the HFL technique. The rail head shape profiles range between 182.8 µm and 186.2 µm for the PDF technique, a 4 µm change in deformation, and 175 µm and 178 µm, a 3 µm change in deformation, for the HFL technique. The rail base deformed shape profiles range between 15.3 µm and 26.2 µm for the PDF technique and 14.5 µm and 22.6 µm for the HFL technique. The PDF technique produces higher deformations which are expected because the entire volumetric body of the rail is reaching the defined temperature simultaneously. In contrast, a non-uniform heat distribution exists in the rail cross section when the HFL technique is used. This causes the outer fibers of the rail head and base to reach higher temperatures than the inner fibers of the rail head and base. These lower temperatures are because the heat has yet to propagate throughout the inner regions of the rail cross section, thus, lower deformations are produced. **Figure 5.13(b)** and **Figure 5.13(d)** display the curvature plots for the rail head and base, respectively, that similarly reflect the trend found in the shape profiles. The PDF technique produces slightly higher curvatures and changes in curvature compared to the HFL technique. It can then be assumed that an increase in the heating surface area or volume causes higher shape deformations and curvatures.

5.3.1.2 Strain Output – Analysis Type

Following the rail head and base deformation analysis, the effects that heating analysis type have on the strain in the rail web region are investigated. All data is extracted from element A at the center rail web between two successive ties. In this analysis the surface heat flux value of 50 (BTU/ in2/s) is maintained, resulting in a 116°F rail web temperature change. This load step defines a 0.1-time step to extract strain measurements from 10 temperature increments throughout the thermal loading. The PDF technique defines a rail temperature of 120°F. This load step also defines a 0.1-time step to extract strain measurements for 10 temperature increments throughout the thermal loading.

Figure 5.14 plots the transverse and longitudinal strain at element A for comparison of the PDF and HFL techniques. **Figure 5.14(a)** displays the transverse strain for all models increasing linearly with temperature change at the same rate as the baseline model. This confirms that at this location the transverse strain is not affected by the heating analysis technique. In **Figure 5.14(b)** displays slight variations in the longitudinal strain between the heating techniques. The PDF technique produces slightly smaller longitudinal strains compared to the HFL technique which follows the baseline model results. However, all longitudinal strains are very small compared to the transverse strain and can be considered negligible for both techniques. Therefore, the transverse and longitudinal strain are not affected by the heating analysis type.

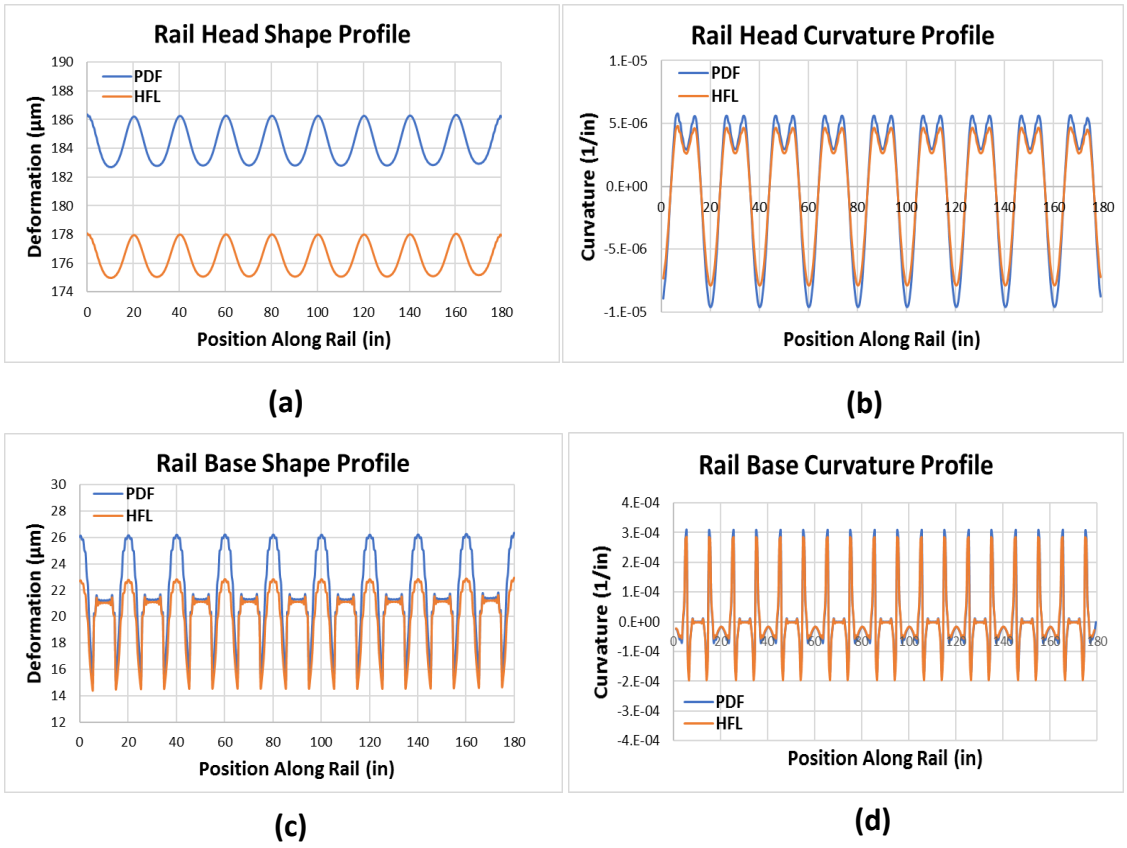

Figure 5.13: Plots of FE deformations with respect to position along the rail to investigate the effects of the thermal analysis type: (a) Rail head shape profiles; (b) Rail head curvature profiles; (c) Rail base shape profiles; (d) Rail base curvature profiles

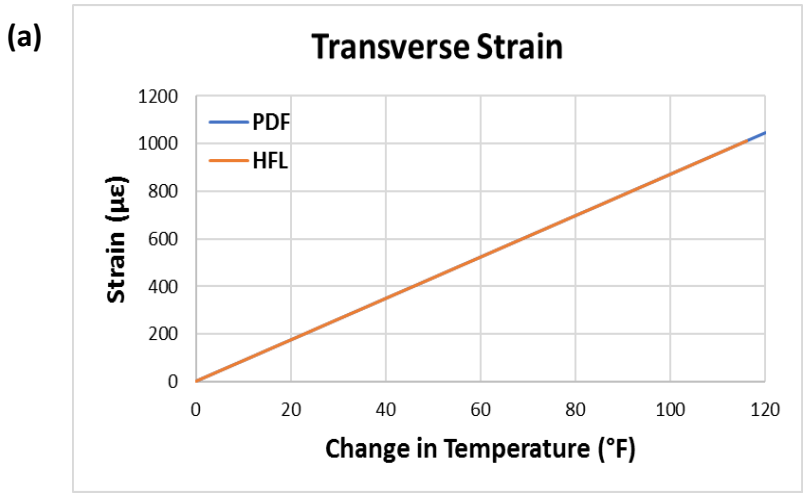

(b)

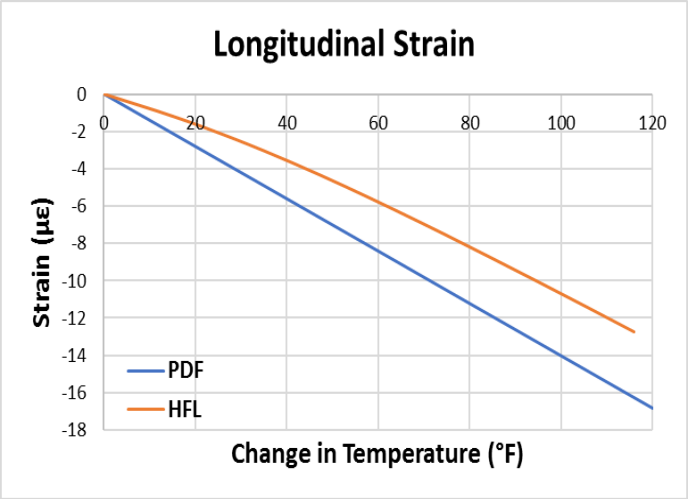

Figure 5.14: Plots of FE strains with respect to temperature change to investigate the effects of the thermal analysis type: (a) Transverse strain; (b) Longitudinal strain

5.3.2 Primary Parametric Study – Heating Surface Area I

This study investigates the difference in the surface area that the heat flux is applied to. This is to observe the different potential surfaces to heat the rail experimentally. The surface heat flux area used in the previous study, which covers the entire outer rail surface, neglecting only the rail ends and the rail bottom surface, is used for comparison in this study and is denoted as “uniform”. Additional heating surface areas pertain to the heating strips currently found in practice. Heating strips are used in the industry to thermally induce rail expansion, such as for rail destressing procedures. While many different sizes and lengths can be fabricated, the heating strip used in this research is 1” wide with negligible thickness. A heating strip that is found in the USC Railway Testing Facility. To simulate this, a surface heat flux is applied along the center line of the rail head and the center of the web with a 1” width and 180” length (spanning the entire rail component). This study modifies the baseline model to investigate the following heating

surface areas: uniform heating, top and side strip heating, top strip heating, and side strip heating. Varying magnitudes of heat flux are used per heating surface area type to produce similar temperature values in the rail head and base regions for comparison and are summarized in **Table 5.3** below. These heat fluxes are selected through trial and error. Average temperatures of 53°F and 28°F are selected for the rail head and base temperature, respectively. The single top strip or side strip heating techniques required higher heat fluxes and longer computation times to reach temperatures in the areas of interest and therefore governed in selection of these rail temperatures.

Table 5.3: Surface heat flux and temperature values for the corresponding heating area

Rail Head		
Heating Area	**Heat Flux (BTU/ in^2/s)**	**Temperature (°F)**
Uniform	41.25	54.5
Top/Side Strip	151	52.75
Top Strip	480	48.75
Side Strip	20.5	52
Rail Base		
Heating Area	**Heat Flux (BTU/ in^2/s)**	**Temperature (°F)**
Uniform	52.8	29
Top/Side Strip	30.5	27.25
Top Strip	60.5	29.4
Side Strip	46.5	29.5

5.3.2.1 Deformation Output – Heating Surface Area I

The impact that the heating surface area has thermal deformations is investigated along the rail head path A-A and base path B-B. **Figure 5.15** plots the shape and curvature profiles along the rail head and base for the four different heating surface areas: uniform, top strip and side strip, top strip, and side strip.

In **Figure 5.15(a)** and **Figure 5.15(c)**, the deformed shape profiles along the rail head and base are displayed for analysis. The shape deformations along the rail head and base are affected by the heating surface area in the following manner: overlooking the side strip heating method, an increase in the heating surface area causes an increase in the deformations and changes in deformations, similar to the preliminary study which found an increase in the heat volume and area causes an increase in deformations and changes in deformations. Thus, the deformations decrease in magnitude in the following order: uniform heating, top and side strip heating, and top strip heating. This is expected because a larger heating surface area causes more regions along the rail cross section to heat simultaneously, and therefore, vertically expand causing higher deformations. The side strip heating method is an exception to this trend. The side heating strip is located at the thinnest cross-sectional region of the rail and produces the highest deformations and changes in deformations. Therefore, at the rail web, a smaller volume of the rail is required to heat up, with a higher heat flux magnitude, before inevitably pushing the rail head and base up. In contrast, the other heating surface area methods are applied to thicker sections of rail and therefore, are producing smaller deformations because larger sections of the rail must be heated prior to inducing the flexure-like deformations. In **Figure 5.15(b)** and **Figure 5.15(d)**, the curvature profiles along the rail head and base are displayed. The rail head curvature profiles follow the same trend found with the shape profiles: an increase in the heating surface area, typically increases the curvatures, except for the side heating strip method. In contrast, the rail base curvature profiles appear to be approximately the same for all four heating surface area methods.

This study suggests that heating thinner sections of the rail may be more advantageous because it will cause higher deformations in both the rail head and base to emerge. The only shortcoming of this method is that higher heat flux values are required to reach the similar rail head and base temperatures compared to the methods that cover larger surface areas. In conclusion, this study resulted in two findings: (i) the region at which the heat source is applied, affects the deformations. A thinner cross section, such as the web, will produce larger deformations as opposed to a thicker cross section because heat is propagating throughout this region at a faster rate and (ii) typically, an increase in the heating surface area will also increase the deformed shape and curvature profiles. Therefore, heating methods should be concentrated on the center rail web region, but an increase in the heating surface area is also beneficial.

5.3.2.2 Strain Output – Heating Surface Area I

Following the rail head and base deformation analysis, the effects that heating surface area methods have on the strain in the rail web region are investigated in **Figure 5.16**. The magnitude of heat flux applied with the corresponding heating surface area is summarized in **Table 5.4** below. Heat flux values are parametrically chosen until reaching similar maximum temperatures of 116°F at element A located at the center of the rail web. For strain analysis, identical rail web temperatures between heating surface area methods is not as critical due to the linear relationship found between strain and temperature change. **Figure 5.16** plots the transverse and longitudinal strain at element A for comparison of the heating surface area methods.

Table 5.4: Surface heat flux value with the corresponding heating surface area method

Heating Method	Heat Flux (BTU/ in^2/s)
Uniform	50
Top and Side	200
Top	1600
Side	500

Figure 5.16(a) displays the transverse strain of all models increasing linearly with temperature change at the same rate as the baseline model. This confirms that at this location, the transverse strain is not affected by the heating surface area method. **Figure 5.16(b)** displays slight variations in the longitudinal strain between the heating surface area methods. An increase in the heating surface area and the closer proximity the heating surface area is to the rail web, produce slightly higher magnitudes of longitudinal strain. However, all longitudinal strains are very small compared to the transverse strain and can be considered negligible for all heating surface area methods. Therefore, the transverse and longitudinal strain are not affected by the heating surface area method.

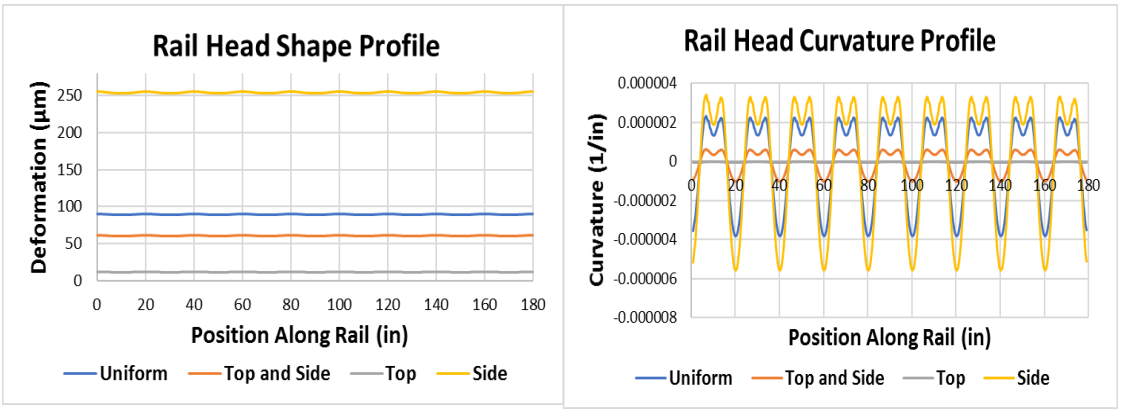

(a) **(b)**

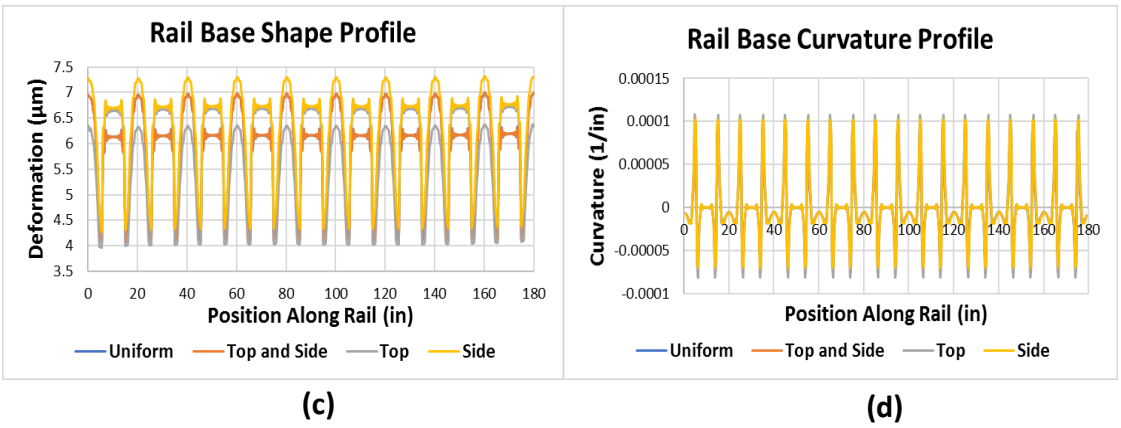

(c) (d)

Figure 5.15: Plots of FE deformations with respect to position along the rail to investigate the effects of the heating surface area technique: (a) Rail head shape profiles; (b) Rail head curvature profiles; (c) Rail base shape profiles; (d) Rail base curvature profiles

(a)

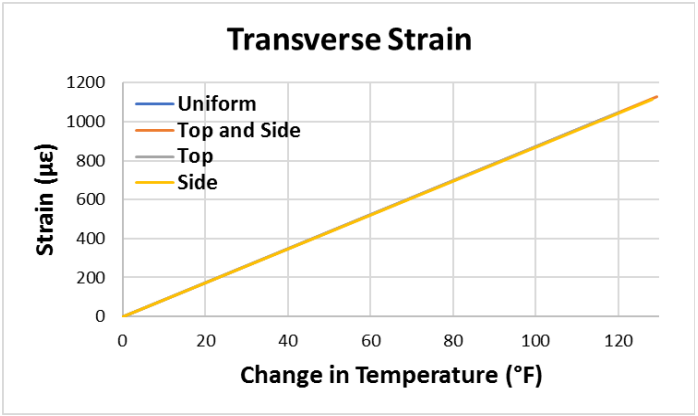

(b)

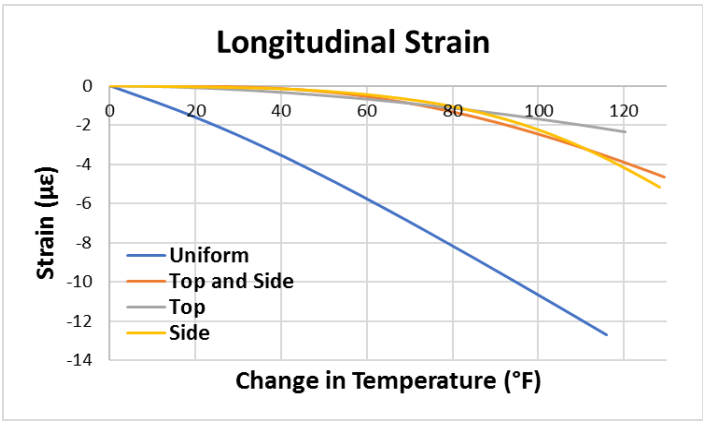

Figure 5.16: Plots of FE strains with respect to temperature change to investigate the effects of the heating surface area technique: (a) Transverse strain; (b) Longitudinal strain

5.3.3 Secondary Study – Heating Surface Area II

The previous studies confirm that the heating method influences the deformed shape and curvature profiles in two ways: the thickness of the region that the heat source is being applied to and the amount of surface area or volume being covered. Heating the bottom surface of the rail with a surface heat flux has yet to be observed. While the bottom flange of the rail is relatively long, it does contain a thinner cross-sectional region near the flange ends in comparison to the rail head. With the trend forming that an increase in the heating surface area/volume may lead to an increase in deformations and higher changes in deformations, an additional study is performed.

This study compares the effect of using the uniform heating surface area previously described in the primary study, which includes the entire outer rail surface except for bottom surface, to the entire outer rail surface including the bottom surface. Both methods do not heat the rail ends as direct exposure to the ends is impractical in the field due to the continuity of CWR, as well as in the laboratory if the prototype rail ends are constrained. Thus far, the changes in deformation along the rail head have been small which may lead to issues with noise in measurements with the proposed instrumentation, despite the deformations being well above its lower limit of accuracy. Therefore, it is desirable to find a parameter that may increase this change. This study is performed along only the rail head. The baseline model is used and a heat flux value of 50 (BTU/ in2/s) is applied for both heating surface areas. This flux produced a constant temperature along the rail head of 111.5°F and 109.5°F, for the heating method that includes the bottom surface, and the heating method that does not include the bottom

surface, respectively. This slight difference in temperature is not expected to produce differences in results. The rail head shape profiles are extracted along path A-A for comparison.

In **Figure 5.17**, the two models with varying heating surface areas are shown for analysis regarding the rail head shape deformations. The deformed shape is affected by the heating surface area in the following manner: with an increased heating surface area, there is an increase in the deformations and change in deformations. The shape profile that does not include the bottom surface produces deformations ranging between 175 µm and 178 µm, a 3 µm difference. In contrast, the shape profile that includes the rail bottom surface produces deformations ranging between 212 µm and 217 µm, a 5 µm difference. It can then be concluded that inclusion of the bottom rail surface produces higher deformations. This study confirms the trend that an increase in the heating surface area causes an increase in the change in deformation.

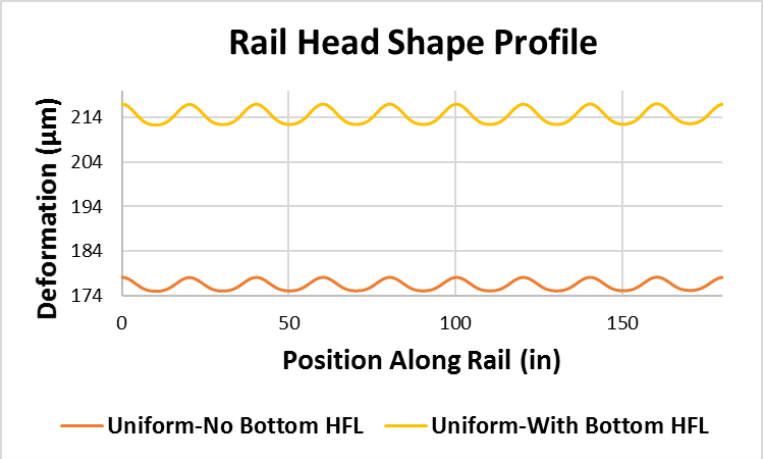

Figure 5.17: Plots of FE shape profiles along the rail head to investigate different heating surface areas

5.3.4 Discussion and Conclusions of the Thermal Loading Method Parametric Study

Upon completion of the analysis type and heating surface area method studies, the following conclusions can be made:

Preliminary Study – Analysis Type

- The thermoelastic analysis is the more practical approach because it considers the effects of heat flow throughout a rail section. However, the static analysis is adequate because it produces deformations similar to the thermoelastic analysis.
- The transverse strain is not affected by the analysis type.
- The longitudinal strain in both analyses is very small compared to the transverse strain and can be considered negligible.

Primary Study and Secondary Study – Heating Surface Area Methods

- Typically, an increase in the heating surface area will produce higher shape deformations and curvatures.
- The side heating strip is an exception to the above trend. This method proves that the region at which the heat source is applied affects the deformations. By heating a thinner volume, such as the rail web, will result in higher deformations in comparison to a thicker section, such as the rail head.
- The single top strip or side heating strip method require a much higher surface heat flux value. A decrease in the heating surface area, indicates a necessary increase in the heat flux to obtain similar temperature changes at the regions of interest.

- Inclusion of the bottom surface in the heating surface area method produces higher deformations and changes in deformations.
- The transverse strain is not affected by the heating surface area method.
- The longitudinal strain for all heating surface areas is very small compared to the transverse strain and can be considered negligible.

It is concluded that it is advantageous to either apply heat to thinner cross sections of the rail or to larger surfaces areas on the rail to induce larger deformations. Additionally, the thermoelastic analysis is the more practical approach for the purposes of this research because it considers the effects of heat flow throughout a rail section. However, while the static analysis is much more unrealistic because it assumes complete temperature uniformity within a rail section, it is still an adequate approach because deformations are very similar to the thermoelastic analysis. Therefore, both analysis types will continue to be used throughout this thesis.

5.4 Effects of Rail Size

Different AREMA rail sizes are explored to investigate the impact that the rail geometry has on the deformations along the rail head and base and the transverse and longitudinal strains at the rail web. The following cross sections are sketched and imported to develop modified versions of the baseline model: 115 RE, 132 RE, and 136 RE. The cross-sectional geometric properties are presented in **Table 5.5** and the dimensions for the 115 RE and 136 RE are found in **Figure 5.18** below. Because the rail base in the 115 RE section is 5.5”, the tie plate component is resized. The component is

dimensioned 5.5” x 8.5” for the 115 RE rail section to account for this change in base dimension. The initial tie plate is dimensioned 6” x 8.5”, to match the rail base dimension of 6” for the 132 RE and 136 RE sections. In this study, the static analysis is used to produce the same rail temperature for all rail cross sections. This is to eliminate any effects that non-uniform temperature distributions and different temperatures in the areas of interest may have on the results to obtain purely the effects that the geometry has on thermal deformations. Each model is run twice, defining first a predefined temperature field of 115°F for the rail head data, and then 90°F for the rail base data.

Table 5.5: Rail size geometric properties (Orringer, Morris and Jeong 1986)

Rail Cross Section	**115 RE**	**132 RE**	**136 RE**
Area (in^2)	11.25	12.95	13.35
Moment of Inertia, I_{yy} (in^4)	65.60	88.2	94.90
Moment of Inertia, I_{zz} (in^4)	10.40	14.2	14.50
Section Modulus, Head (in^3)	18.0	22.5	23.78
Section Modulus, Base (in^3)	22.0	27.6	28.3
Centroid Height (in)	2.98	3.2	3.35
St. Venant Constant, J (in^4)	97.90	133.6	148.20

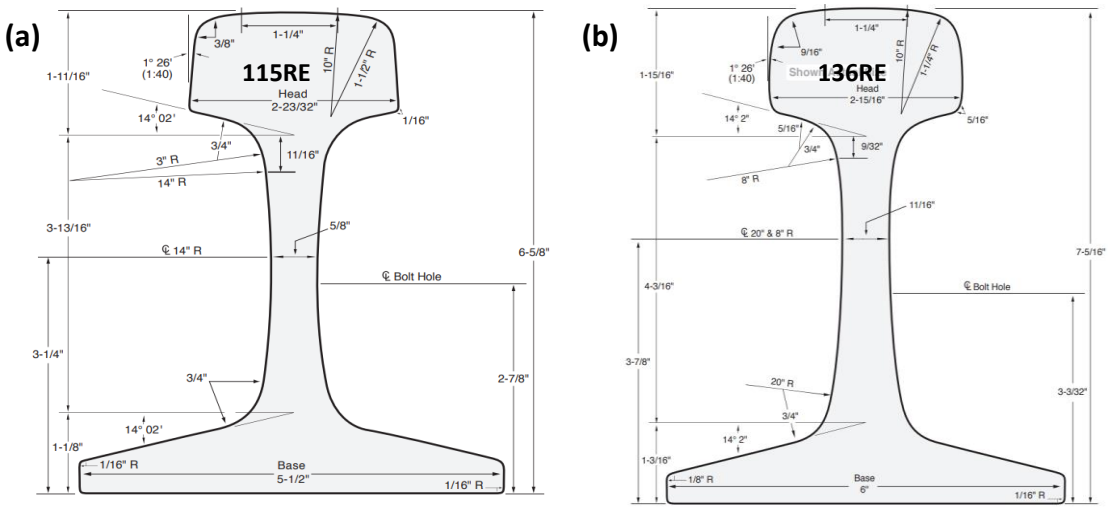

Figure 5.18: Rail cross sections: (a) 115 RE; (b) 136 RE (Harmer Steel Co. 2014)

5.4.1 Deformation Output – Rail Size

The shape and curvature profiles are analyzed to determine the impact that the rail geometry has on the thermal deformations. **Figure 5.19** plots the vertical shape and curvature profiles along the rail head path A-A and base path B-B for the 115 RE, 132 RE, and 136 RE rail cross sections.

In **Figure 5.19(a)** and **Figure 5.19(c)**, the shape profiles along the rail head and base are shown. The rail head and base produce the same shape deformation trend. The deformed shape is affected by the rail size in the following manner: with a decrease in rail size, there is a decrease in the deformations. Thus, the deformed shape profiles decrease in the following order: 136 RE, 132 RE, and 115 RE. The 136 RE and 132 RE deformed shape profiles display more similar deformation values; this is expected because these cross sections are more alike compared to the 115 RE. A change in deformation of 3 μm is maintained for all rail sizes along the rail head profile, whereas only slight differences exist along the rail base profile. In **Figure 5.19(b)** and **Figure 5.19(d)**, the curvature profiles along the rail head and base are shown. Only small differences exist between curvatures for different rail sizes, thus, these differences are considered negligible for both regions.

5.4.2 Strain Output – Rail Size

Following the vertical deformation analysis, the effects of rail geometry on the rail web thermal strains are investigated. All data is extracted from element A located at the centroid in the rail web between successive ties. Element A is modified for each rail size as different centroidal heights exist for the different cross sections. The element selected is located at a distance 80” along the rail, the center between the 4^{th} and 5^{th} tie support

locations, and at the centroidal height listed in **Table 5.5** for the corresponding rail sizes. **Figure 5.20** plots the transverse and longitudinal strain at this element for all rail sizes.

Figure 5.20(a) displays the transverse strain of all models increasing linearly with temperature change at the same rate as the baseline model. This confirms that at this location, the transverse strain is not affected by the rail size. **Figure 5.20(b)** displays slight variations in the longitudinal strain for the cross sections. This is due to the geometric properties pertaining to the web thickness for each rail cross section. All longitudinal strains are very small compared to the transverse strain and can be considered negligible. Therefore, the transverse and longitudinal strain are not affected by the rail geometry.

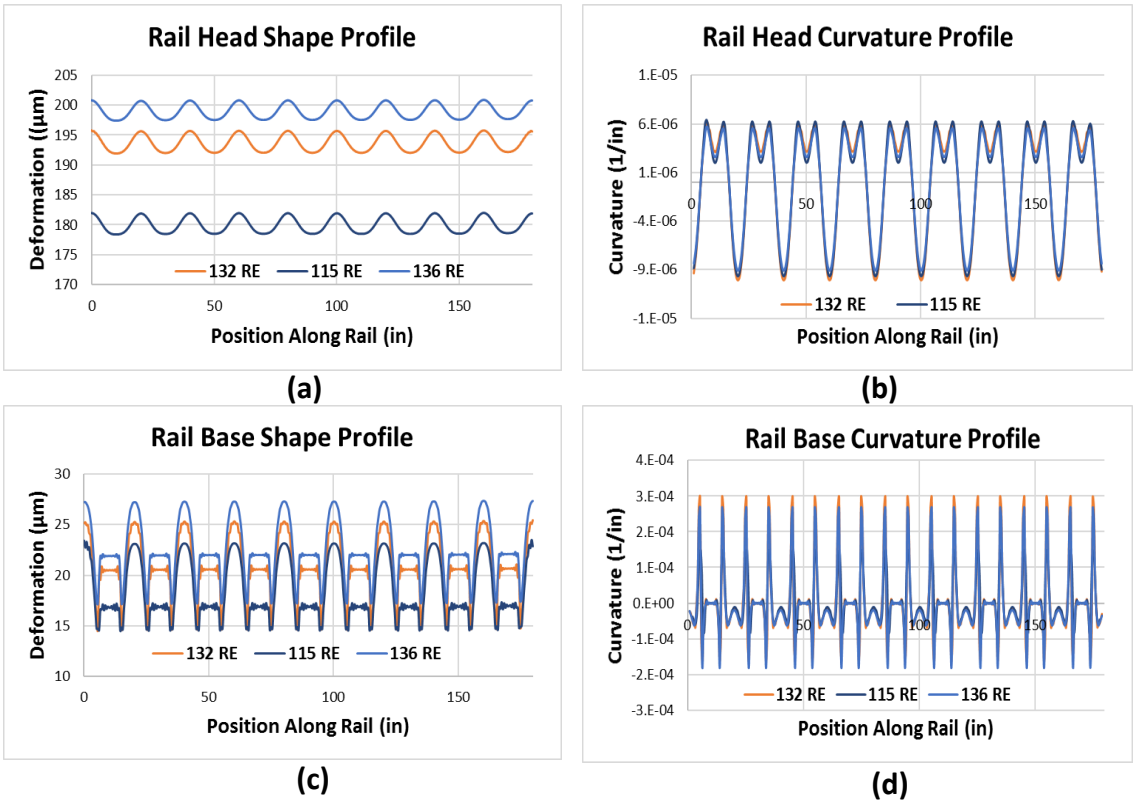

Figure 5.19: Plots of FE deformations with respect to position along the rail to investigate the effects of rail size: (a) Rail head shape profiles; (b) Rail head curvature profiles; (c) Rail base shape profiles; (d) Rail base curvature profiles

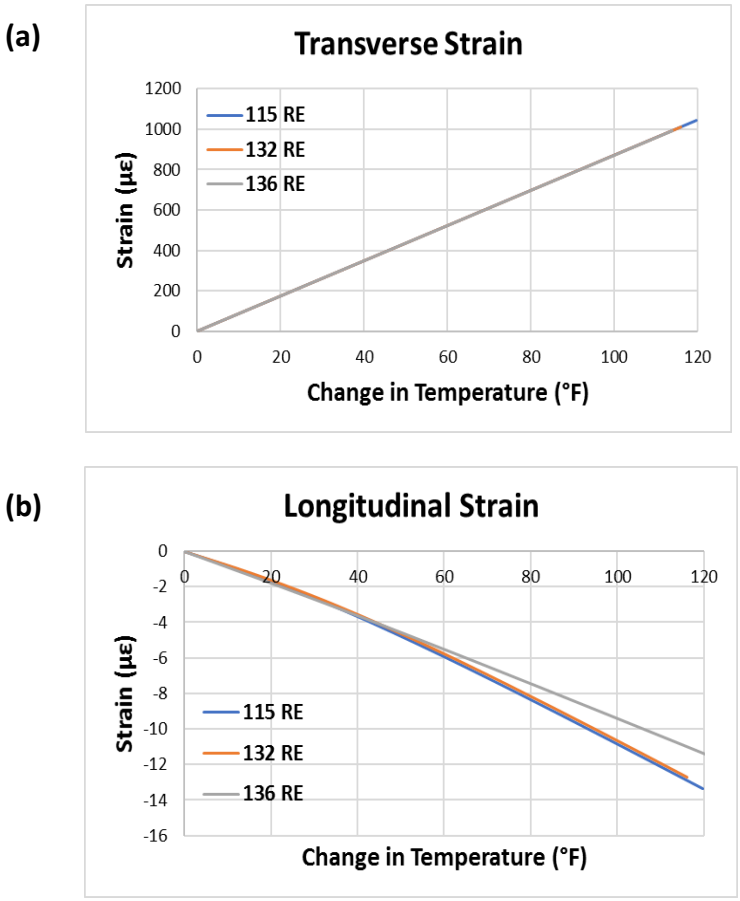

Figure 5.20: Plots of FE strains with respect to temperature change to investigate the effects rail size: (a) Transverse strain; (b) Longitudinal strain

5.4.3 Discussion and Conclusions on the Rail Size Parametric Study

Upon completion of this rail size study, the following conclusions can be made:

- An increase in rail size causes an increase in deformed shape profiles.
- The rail head change in deformation is constant for all rail sizes.
- The curvature appears to be approximately the same for all rail sizes in both the rail head and base regions.
- The transverse strain is not affected by the rail size.

- The longitudinal strain for all rail sizes is very small compared to the transverse strain and can be considered negligible.

Because all rail sizes produce rail head deformations well above the lower limit of accuracy of the StereoDIC system and the strain fields are insignificantly affected by this parameter, this study confirms that the proposed instrumentation and methodology can be simply implemented on a track system with any rail size.

5.5 Effects of Tie Spacing

The AREMA manual states that the acceptable range for concrete tie spacing is between 20”- 30” center-on-center. Concrete ties are the tie type found in the USC Railway Testing Facility, therefore, these two spacing extremes are investigated. In this study, the baseline model is modified to reflect these two different tie spacings. It is noted that due to the change in tie spacing, the spring stiffness at the tie plate must be adjusted. The tie plate stiffness is a function of the tie spacing and general track modulus. Using the baseline model, a general track modulus of 4,000 psi is selected indicating a resilient tie plate type. The modified spring stiffness for the 30” spacing is directly calculated as 120,000 lb/in. The spring stiffnesses for each tie spacing are summarized in **Table 5.6** below.

Table 5.6: Tie plate spring stiffness computed per defined tie spacing

Tie Spacing	General Track Modulus	Spring Stiffness
30”	4,000 psi	120,000 lb/in
20”	4,000 psi	80,000 lb/in

5.5.1 Deformation Output – Tie Spacing

The shape and curvature profiles are analyzed to determine the impact that the tie spacing has on the rail thermal deformations. **Figure 5.21** plots the deformed shape and curvature profiles along the rail head path A-A and base path B-B. The 20" and 30" tie spacings are then compared. It is noted that the deformation and curvature peaks are located at different positions but still exist generally between two successive ties or about the anchoring point for both tie spacings.

In **Figure 5.21(a)** and **Figure 5.21(c)**, the deformed shape profile along the rail head and base are displayed, respectively. It is shown that the rail head and base produce a similar shape deformation trend. The deformed shape is affected by the tie spacing in the following manner: with an increase in tie spacing, there is an increase in the deformations and changes in deformations. The 30" tie spacing produces shape profiles ranging between 175 µm to 180 µm, a 5 µm difference, and 14.3 µm to 24.3 µm, a 10 µm difference for the rail head and base, respectively. The 20" tie spacing produces shape profiles ranging between 17 5µm to 178 µm, a 3 µm difference, and 14.5 µm to 22.6 µm, an 8 µm difference, for the rail head and base, respectively. While this increase in the change in deformation may seem minimal, the increase in this value will minimize the proposed technology challenges associated with noise. In **Figure 5.21(b)** and **Figure 5.21(d)**, the curvature profiles along the rail head similarly follows the trend found with the shape profiles. The rail head curvature is affected by the tie spacing in the following manner: with an increase in tie spacing, there is an increase in the curvature and change in curvature values, whereas the rail base seems to produce similar curvature values.

5.5.2 Strain Output – Tie Spacing

Following the rail head and base deformation analysis, the effects of tie spacing on the rail web thermal strains are investigated. All data is extracted from an element at the center cross section of the rail web between two successive ties. For the 20” spacing element A is located at a length 80” along the rail, and for the 30” spacing this element is located at a length 120” along the rail; generally, the center distance between the 4th and 5th tie support locations are chosen. **Figure 5.22** plots the transverse and longitudinal strain for both tie spacings.

Figure 5.22(a) displays the transverse strain for both models increasing linearly with temperature change at the same rate as the baseline model. This confirms that at this location the transverse strain is not affected by the tie spacing. **Figure 5.22(b)** displays a slight variation in the longitudinal strain between the tie spacings, but both models generally follow the same decrease in strain as the baseline model. All longitudinal strains are very small compared to the transverse strain and can be considered negligible. Therefore, the transverse and longitudinal strain are not affected by the tie spacing.

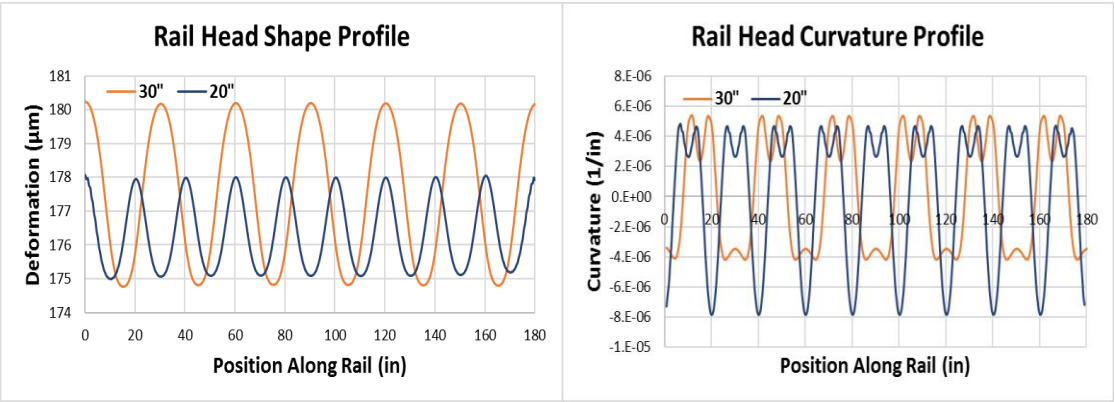

(a) **(b)**

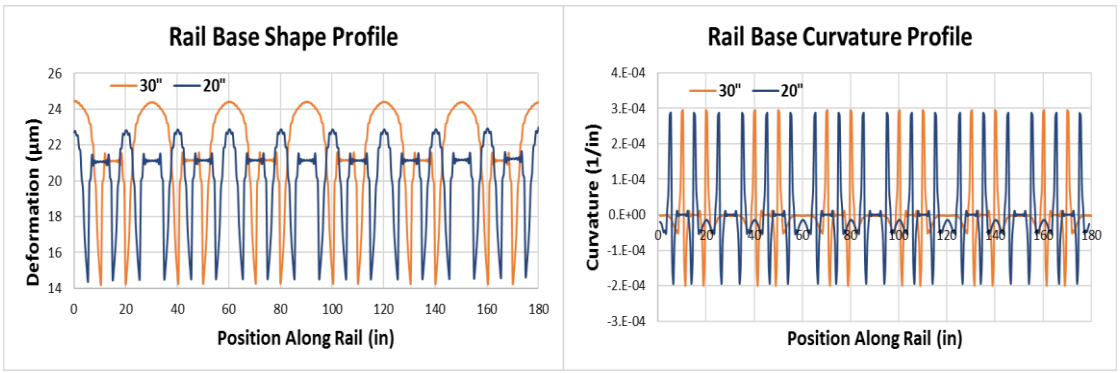

Figure 5.21: Plots of FE deformations with respect to position along the rail to investigate the effects of tie spacing: (a) Rail head shape profiles; (b) Rail head curvature profiles; (c) Rail base shape profiles; (d) Rail base curvature profiles

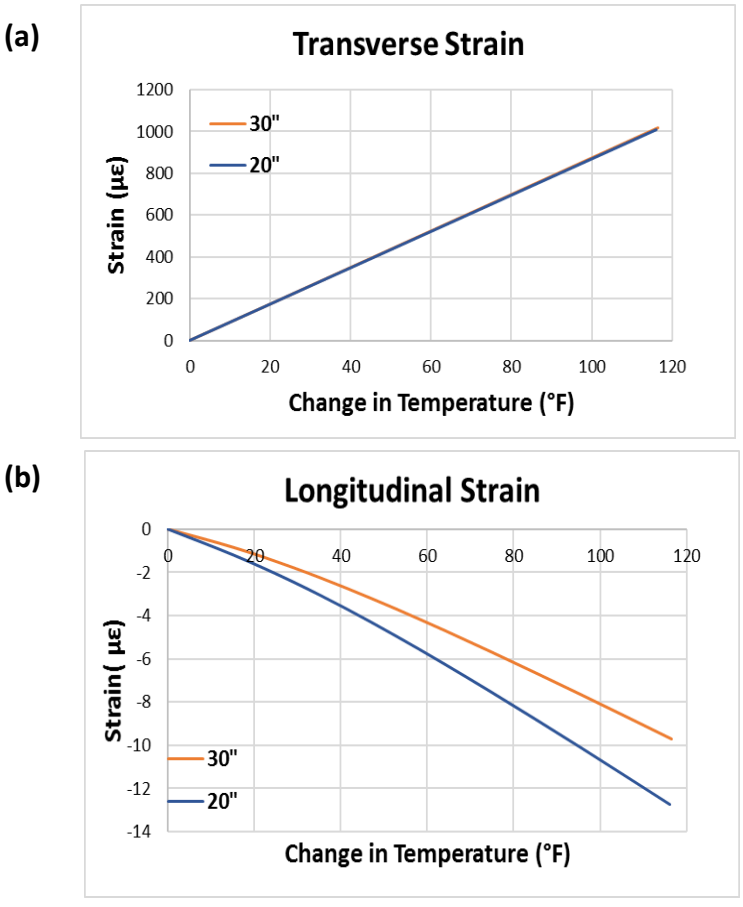

Figure 5.22: Plots of FE strains with respect to temperature change to investigate the effects of tie spacing: (a) Transverse strain; (b) Longitudinal strain

5.5.3 Discussion and Conclusions on the Tie Spacing Parametric Study

Upon completion of the tie spacing study, the following conclusions can be made:

- An increase in tie spacing causes an increase in the shape deformations and changes in deformations in both the rail head and base regions.
- An increase in tie spacing, causes an increase in the curvatures and changes in curvature along the rail head, whereas both tie spacings produce similar curvatures along the rail base.
- The transverse strain is not affected by the tie spacing.
- The longitudinal strain for both tie spacings is very small compared to the transverse strain and can be considered negligible.

Therefore, future construction of the indoor testing track at USC should consider increasing the current tie spacing as a means of increasing the changes in deformations to minimize issues associated with noise with the proposed technology.

5.6 Effects of Track Stiffness

Different tie plate types are considered to investigate the effect that track stiffness has on the thermal deformations along the rail head and base and the thermal strains located at a center web cross section between consecutive ties. Various tie plate types are investigated including: Resilient tie plates, Old Pandrol tie plates, and New Pandrol tie plates. The general track moduli for each tie plate type is listed in the same order: 4,000 psi, 11,000 psi and 22,000 psi (RailTEC - University of Illinois at Urbana-Champaign n.d.). The tie spacing is constant throughout this study, 20”, and with the listed General Track

Moduli, different tie plate stiffnesses are computed. The stiffness of the springs is adjusted following **Table 5.7** below.

Table 5.7: General Track Modulus and computed spring stiffness per tie plate type

Tie Plate Type	General Track Modulus	Tie Plate Spring Stiffness
Resilient Tie Plate	4,000 psi	80,000 psi
Old Pandrol Tie Plate	11,000 psi	220,000 psi
New Pandrol Tie Plate	22,000 psi	440,000 psi

Each tie plate spring stiffness is evenly distributed amongst nine springs equidistance apart relative to the center of the tie plate, as described in section **4.5.1**. In this study, the baseline model is modified to reflect the varying tie plate stiffnesses.

5.6.1 Deformation Output – Track Stiffness

The deformed shape and curvature profiles are analyzed to determine the effect that track stiffness has on the thermal deformations in the rail. **Figure 5.23** plots the shape and curvature profiles along the rail head path A-A and base path B-B. It is concluded that all models produce identical shape and curvature profiles regardless of the track stiffness, for both the rail head and base regions.

5.6.2 Strain Output – Track Stiffness

Following the rail head and base deformation analysis, the effects of track stiffness on the rail web thermal strain are investigated. All data is extracted from element A at the center of the rail web between two successive ties. **Figure 5.24** plots the transverse and longitudinal strain at this element for all track stiffnesses. **Figure 5.24(a)** displays the transverse strain of all models increasing linearly with temperature change at the same rate as the baseline model. This confirms that at this location the transverse strain is not

affected by the track stiffness. **Figure 5.24(b)** displays the longitudinal strain of all models decreasing with temperature change at the same rate as the baseline model. This confirms that the longitudinal strain is not affected by the track stiffness. Relative to the transverse strain, all longitudinal strains are very small and can be considered negligible. Therefore, the rail web transverse and longitudinal strain are not affected by the track stiffness.

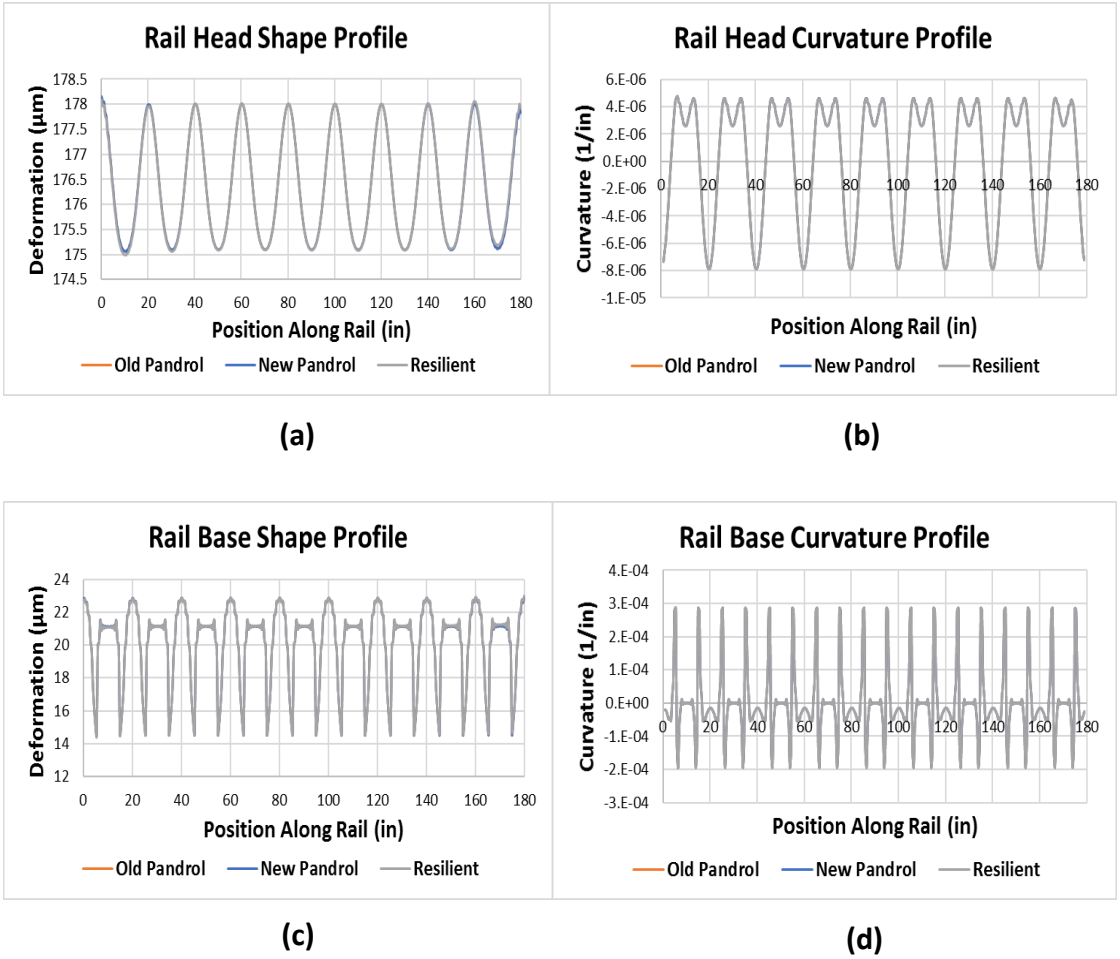

Figure 5.23: Plots of FE deformations with respect to position along the rail to investigate the effects of track stiffness: (a) Rail head shape profiles; (b) Rail head curvature profiles; (c) Rail base shape profiles; (d) Rail base curvature profiles

(a)

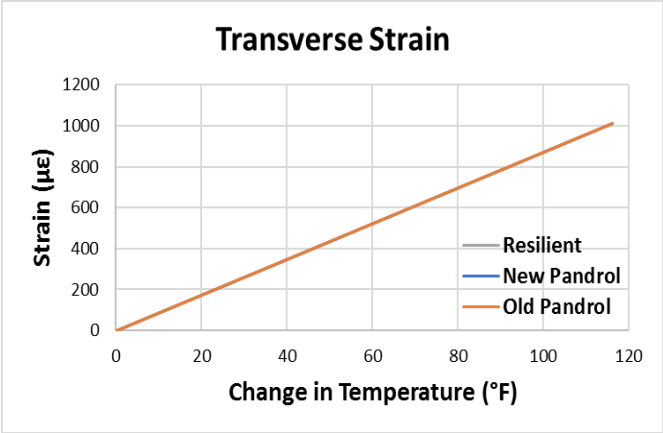

(b)

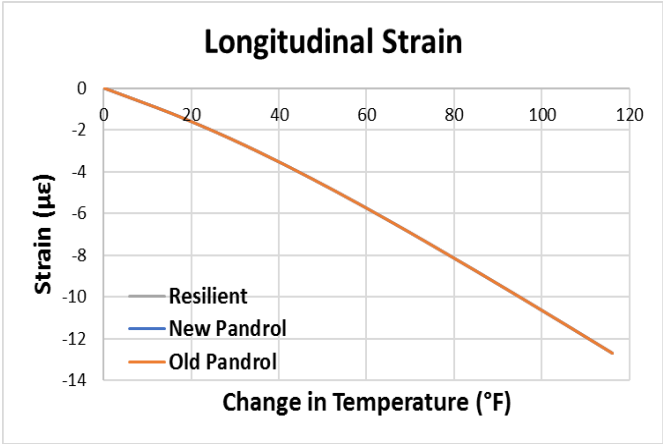

Figure 5.24: Plots of FE strains with respect to temperature change to investigate the effects of track stiffness: (a) Transverse strain; (b) Longitudinal strain

5.6.3 Discussion and Conclusions of the Tie Plate Type Parametric Study

Upon completion of the track stiffness study, the following conclusions can be made:

- The deformed shape profile is not affected by the track stiffness
- The curvature profile is not affected by the track stiffness.
- The transverse strain is not affected by the track stiffness.
- The longitudinal strain is not affected by the track stiffness.

Therefore, the proposed instrumentation and methodology can be simply implemented on any track system regardless of the potential tie plate types or track stiffnesses, provided that the longitudinal constraint exists.

5.7 Overall Assessment

Throughout the parametric studies, many conclusions are drawn about the impact that each parameter has on the deformed shape and curvature profiles along the rail head path A-A and base path B-B, along with the thermal strain at center rail web element A between two successive ties. Below is a summary of the findings per each parameter.

Boundary Conditions

- The shape and curvature along the rail head and rail base flange show similar trends. While the rail head produces larger shape deformations, the rail base produces higher changes in deformations.
- Inclusion of the fastener system produces negligible differences in shape, curvature, and strain in the rail head, base, and web, thus, the fastener system could be omitted.
- Shape and curvature measurements are not affected by either (i) the tie plate support when the rail is fully constrained longitudinally at the rail ends, or (ii) by the level of longitudinal constraint at the rail ends, provided that the rail is fully constrained vertically at tie supports.

- The unconstrained and partially constrained rail end cases with TPS supports produce global flexure along the rail, while the TPC supports produce local flexure between two successive ties.
- The transverse strain is not affected by the level of constraint at the rail ends or at the tie plate support locations.
- The TPS support models confirm that different levels of longitudinal constraint effect the longitudinal strain produced at the rail web. In contrast, the longitudinal strains that develop in TPC models are not affected by the level of constraint at the rail ends.
- The longitudinal strain for all practical models is very small compared to the transverse strain and can be considered negligible.

Heating Analysis/ Heating Surface Area

- The thermoelastic analysis is the more practical approach because it considers the effects of heat flow throughout a rail section. However, the static analysis is adequate because it produces deformations similar to the thermoelastic analysis.
- The transverse strain is not affected by the analysis type.
- The longitudinal strain in both analyses is very small compared to the transverse strain and can be considered negligible.
- Typically, an increase in the heating surface area will produce higher shape deformations and curvatures.

- The side heating strip is an exception to the above trend. This method proves that the region at which the heat source is applied affects the deformations. By heating a thinner volume, such as the rail web, will result in higher deformations in comparison to a thicker section, such as the rail head.
- The single top strip or side heating strip method require a much higher surface heat flux value. A decrease in the heating surface area, indicates a necessary increase in the heat flux to obtain similar temperature changes at the regions of interest.
- Inclusion of the bottom surface in the heating surface area method produces higher deformations and changes in deformations.
- The transverse strain is not affected by the heating surface area method.
- The longitudinal strain for all heating surface areas is very small compared to the transverse strain and can be considered negligible.

Rail Size

- An increase in rail size causes an increase in deformed shape profiles.
- The rail head change in deformation is constant for all rail sizes.
- The curvature appears to be approximately the same for all rail sizes in both the rail head and base regions.
- The transverse strain is not affected by the rail size.
- The longitudinal strain for all rail sizes is very small compared to the transverse strain and can be considered negligible.

Tie Spacing

- An increase in tie spacing causes an increase in the shape deformations and changes in deformations in both the rail head and base regions.
- An increase in tie spacing, causes an increase in the curvatures and changes in curvature along the rail head, whereas both tie spacings produce similar curvatures along the rail base.
- The transverse strain is not affected by the tie spacing.
- The longitudinal strain for both tie spacings is very small compared to the transverse strain and can be considered negligible.

Track Stiffness

- The deformed shape profile is not affected by the track stiffness.
- The curvature profile is not affected by the track stiffness.
- The transverse strain is not affected by the track stiffness.
- The longitudinal strain is not affected by the track stiffness.

The critical findings of the above conclusions are that the boundary conditions at the rail ends and at the tie supports behave synergistically. The rail must either be fully constrained longitudinally at the rail ends or vertically at the tie support locations to obtain the expected deformations. If the rail is fully constrained vertically at the tie locations, but not at the rail ends, measurements must be taken near the center tie location. The rail head is considered the more ideal region to acquire deformed shape profiles because much larger thermal deformations develop in comparison to the rail base

region. The longitudinal strain is only significantly affected when the rail is unconstrained at the rail ends and elastically supported at the tie supports. In the field, the continuity of rail is assumed to impose full longitudinal constraint because of the long lengths found with CWR. Therefore, this support condition combination is not considered realistic and the full-scale prototype system must be constructed in a way that ensures negligible longitudinal strain. Additionally, the transverse strain is significant and not affected by any of the investigated parameters, confirming the assumption that the rail is always stress-free in the central rail web region between consecutive ties. Thus, the proposed methodology, which requires the assumption to be made that transversely the rail is stress-free, can be successfully implemented for all track systems. Regarding the heating surface area methods, heating application should either be concentrated at thinner rail cross sections, such as the web, or cover larger surface areas to produce higher deformations and changes in deformations. Likewise, the maximum acceptable concrete tie spacing, 30" center-on-center, should be utilized because it produces higher deformations and changes in deformations. The variable rail sizes and track stiffnesses produced no significant differences on any of the deformation or strain measurements. Therefore, the proposed methodology can be simply implemented on any track where these parameters are varied. All findings will be used to guide the future construction of the full-scale track prototype system to optimize conditions for the proposed instrumentation.

Chapter 6. Method Verification through Simulated Measurements

This chapter showcases the implementation of the proposed RNT and stress measurement method, discussed in section **3.4**, based on simulated measurements for method verification. The FE computer simulated model is first presented by defining the model properties. The simulated measurements are then obtained considering only the measurements that the proposed instrumentation will acquire. Subsequently, the proposed methodology is implemented for RNT estimations and stress computations.

6.1 Computer Simulation

The model used is a derivative of the baseline model which considers the available laboratory materials and equipment, results from the parametric studies, and the most simplistic approach. The model parameters are summarized in **Table 6.1** below. The typical steel thermal and mechanical material properties used are defined in section **4.4**. This model performs a static analysis and defines a uniform predefined temperature field to impose the desired rail temperature changes. Two load cases are explored to analyze the rail deformation patterns when imposing a positive or negative temperature change. A positive rail temperature change, $\Delta T=+125°F$, and a negative rail temperature change, $\Delta T=-125°F$, are applied.

Table 6.1: Model parameters defined for implementation of the proposed methodology on simulated measurements

Parameter	Value
Rail Size/Length	132 RE/180”
Number of Tie Plates	9
Tie Plate Spacing	20”
Rail End Boundary Condition	Fully Constrained
Tie Plate Boundary Condition	TPC: X, Y, Z Constrained
Fastener System Used	No
Model Type	Static Analysis
Heating/Cooling Method	Predefined Temperature Field
Heating/Cooling Technique	Uniformly applied to entire rail body

Figure 6.1 shows the deformed configurations for the positive and negative temperature loadings throughout the solutions stages with the vertical deformation field (U2) superimposed on the rail. The typical two-step procedure is implemented to simulate an RNT of 100°F.

1. *Initial Step:* This is the first step that Abaqus requires. In this model, an initial predefined temperature field of 100°F is defined to the rail. Tie constraints between the rail-tie plate interface are activated in this step, but no mechanical boundary conditions currently exist, as depicted in **Figure 6.1(a).** The rail is existing stress-free at 100°F.
2. *Anchor/Load:* The mechanical boundary conditions are then activated in this step at a rail temperature of 100°F. This simulates an RNT of 100°F because this is the temperature at which the rail is anchored down to the ties. The rail ends are fully constrained longitudinally, and all deformations are constrained at the tie support locations. The predefined temperature field is then modified to impose the positive and negative temperature fluctuations over the time step. **Figure 6.1(b)**

displays the final deformed shape after the positive temperature changes have incurred. The rail expands vertically due to the positive temperature change, and local flexure exists along the rail head and base flange between successive ties due to the imposed boundary conditions.

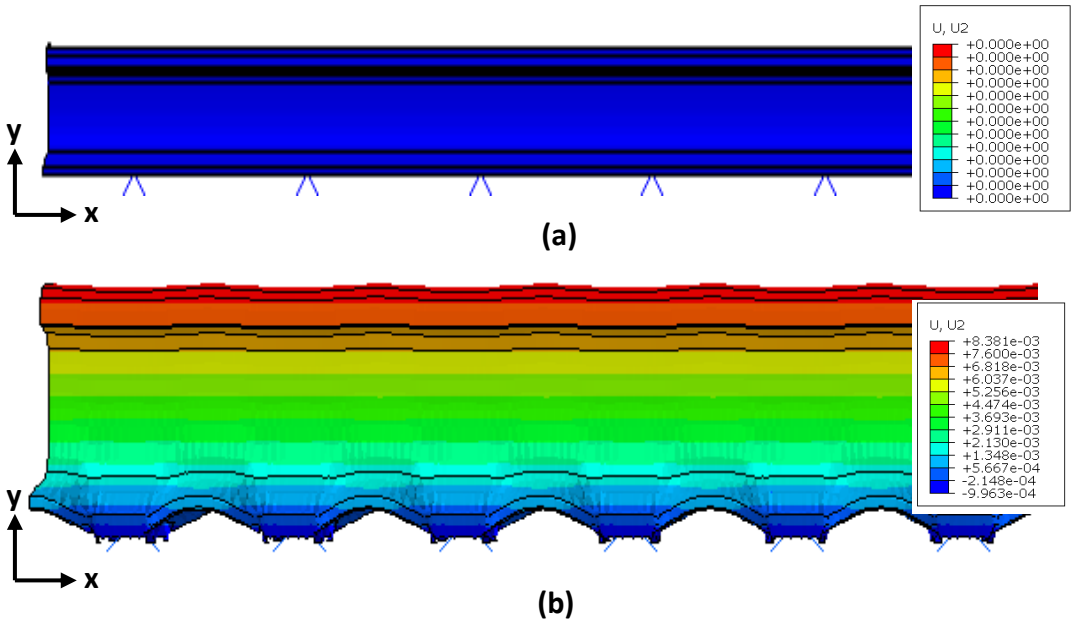

Figure 6.1: FE progression of deformed shapes of two-step procedure: (a) Initial step; (b) Anchor/Thermal Loading step at T=225°F (uniformly scaled at 10^3)

6.2 Acquisition of Simulated Measurements

Two types of data must be acquired by the proposed StereoDIC system to implement the proposed measurement system. First, the vertical shape deformations along the rail head must be obtained to compute the average curvature between two successive ties, followed by the RNT estimate. Subsequently, the changes in strain, with respect to the reference measurement, are acquired at the center rail web section between two successive ties. The captured measurements initially consider the reference image as the zero-strain state. Because the zero-strain state exists when the rail is at the

RNT, not necessarily when the initial reference image is captured, knowledge of the RNT is required to uniquely define the temperature-strain relationship. The strain measurements can then be used to estimate the longitudinal stress in rail.

6.2.1 Shape Deformation Measurements

The first set of data initially acquired by the StereoDIC system is the vertical shape deformation profiles along the rail head. Initially the FE shape profiles are extracted along the rail head for curvature computation. The rail head in the FE model represents a perfect rail cross section extruded uniformly to the necessary rail length. Because the model initially defines the rail at its RNT, and no geometric irregularities exist because the rail is perfectly flat along the rail head, the initial shape is considered zero. However, in the field the rail will more than likely not be resting at its RNT when initial reference images are captured, and geometric irregularities may exist, therefore the initial shape may not always be considered flat and zero. For the purposes of using simulated data, this is defined to simplify the procedure. Data pertaining to only a 10-inch section of the rail is extracted for analysis. This 10-inch section is centered between the 4^{th} and 5^{th} tie support locations. Any rail section centered between two ties could have been selected because deformations are periodic throughout. Deformed shape profiles are extracted along the rail head path a-a, visualized in **Figure 6.2**. The shape profiles are made relative to the center point between the ties, ranging from -5” and 5”.

The positive and negative predefined temperature fields produce different deformed shapes, as shown in **Figure 6.3**, which depicts the deformed rail shapes at T=225°F and T=-25°F. The vertical deformation (denoted as U2), is superimposed on the

rail. In **Figure 6.3(a)**, the positive temperature change causes local flexure and positive deformations in the region between two successive ties. This causes negative stress to develop and the rail head can be considered in compression. Based on the initial hypothesis presented in section **3.1**, it can be inferred that the rail temperature is above the RNT. In **Figure 6.3(b)**, the negative temperature change causes local flexure and negative deformations in the region between two successive ties. This causes positive stress to develop and the rail head can be considered in tension. Based on the initial hypotheses presented in section **3.1**, it can be inferred that the rail temperature is now below the RNT. This confirms that as the rail curvature changes from positive to negative, the rail is shifting from above to below the RNT, and vice versa. The temperature corresponding to zero-curvature represents the RNT.

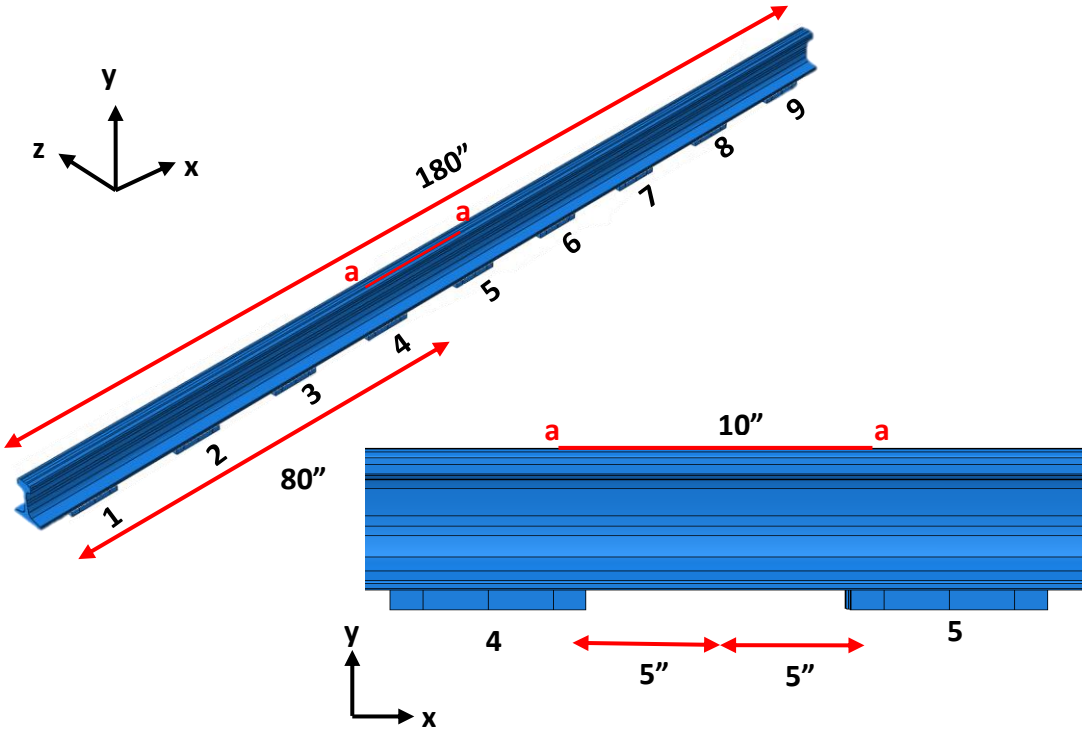

Figure 6.2: FE rail head shape deformations extracted along path a-a for analysis

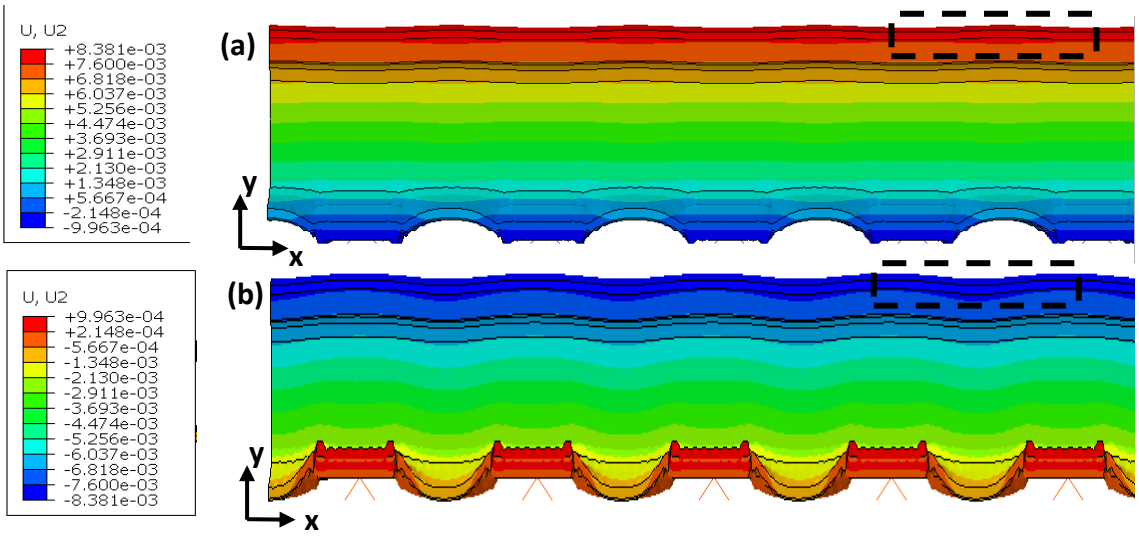

Figure 6.3: Deformed rail shapes show how the curvature in the area of interest (dashed black rectangle) changes from positive to negative when the rail is at a temperature: (a) 125°F above RNT (uniform scale deformation factor: 10^3); (b) 125°F below RNT (uniform scale deformation factor: 10^2 and additional y coordinate scaling: 5)

Figure 6.4(a) displays the five deformed shape profiles acquired that correspond to different rail temperatures upon completion of the positive rail temperature change. **Figure 6.4(b)** and **Figure 6.4(c)** plot two individual shape profiles for visualization of the deformation behavior corresponding to unique rail head temperatures (T=175°F and 125°F). The deformation behavior is not as easily seen in **Figure 6.4(a)** due to the y-axis scale. Curve fitting is applied to each shape profile to describe the average deformation behavior with a quadratic for a given rail temperature. As seen by the R^2 parameters in **Figure 6.4(b)** and **Figure 6.4(c)**, the quadratic accurately represents this data. It is concluded that as the change in temperature increases, the shape deformation magnitude increases accordingly. Specifically, as the rail temperature increases above the RNT, the deformations continually increase. This increase in deformation is associated with an increase in the magnitude of curvature; the curvature becomes more negative.

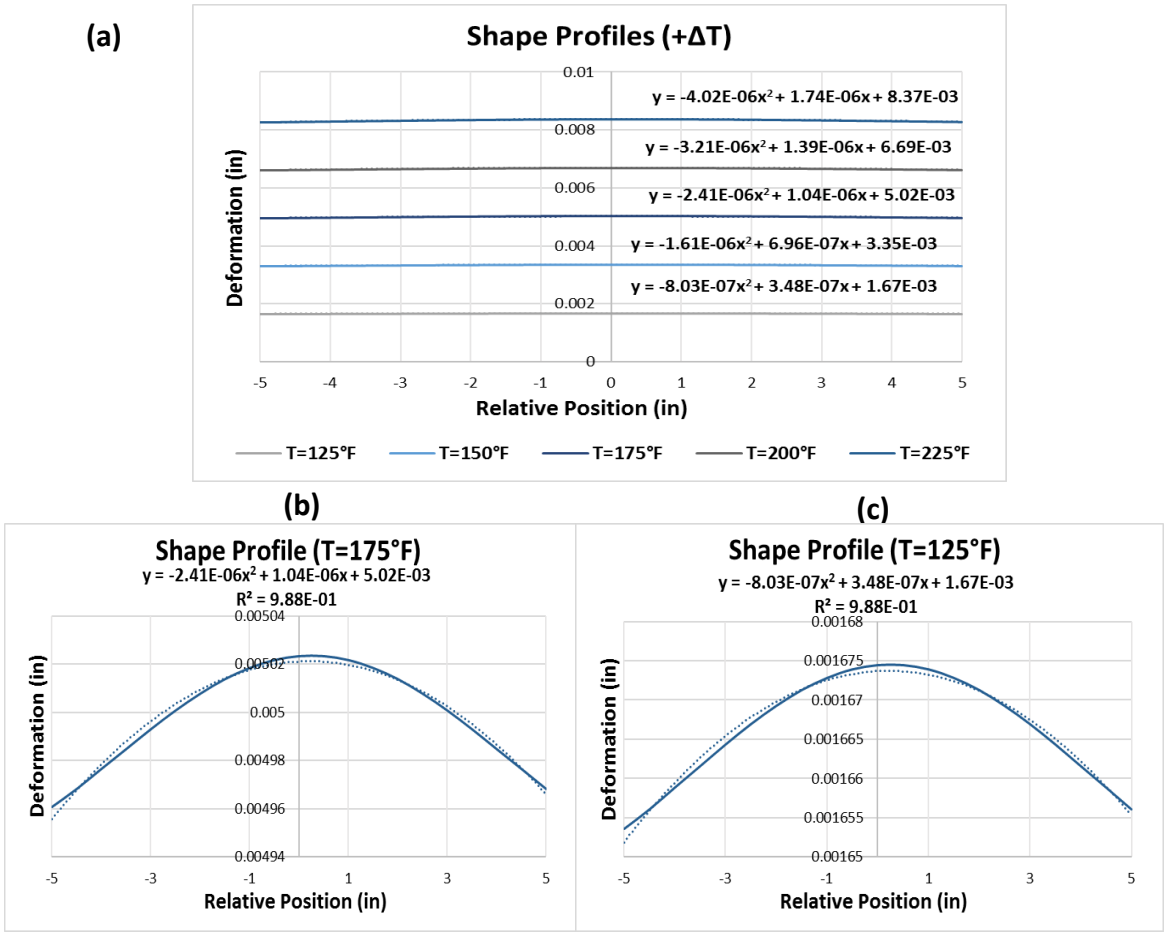

Figure 6.4: Plots of the FE deformed shape measurements along the rail head: (a) Shape profiles for rail temperatures above the RNT; (b) Shape profile at T=175°F (ΔT=75°F); (c) Shape profile at T=125°F (ΔT=25°F)

This process is repeated to acquire the negative temperature change FE deformed shape profiles for subsequent curvature computation**. Figure 6.5(a)** displays the five deformed shape profiles acquired that correspond to different rail temperatures upon completion of the negative rail temperature change. **Figure 6.5(b)** and **Figure 6.5(c)** plot two individual shape profiles for visualization of the deformation behavior corresponding to unique rail head temperatures (T=-25°F and 75°F). The deformation behavior is not as easily seen in **Figure 6.5(a)** due to the y-axis scale. Curve fitting is applied to each shape profile to describe the average deformation behavior with a quadratic for a given rail

temperature. As seen by the R^2 parameters in **Figure 6.5(b)** and **Figure 6.5(c)**, the quadratic accurately represents this data. It is concluded that as the change in temperature increases, the shape deformation magnitude increases accordingly. This increase in deformation also corresponds to an increase in curvature. Specifically, as the rail temperature decreases below the RNT, the deformations continually decrease (or increase in magnitude). This decrease in the deformations is associated with an increase in curvature magnitude; the curvatures become more positive.

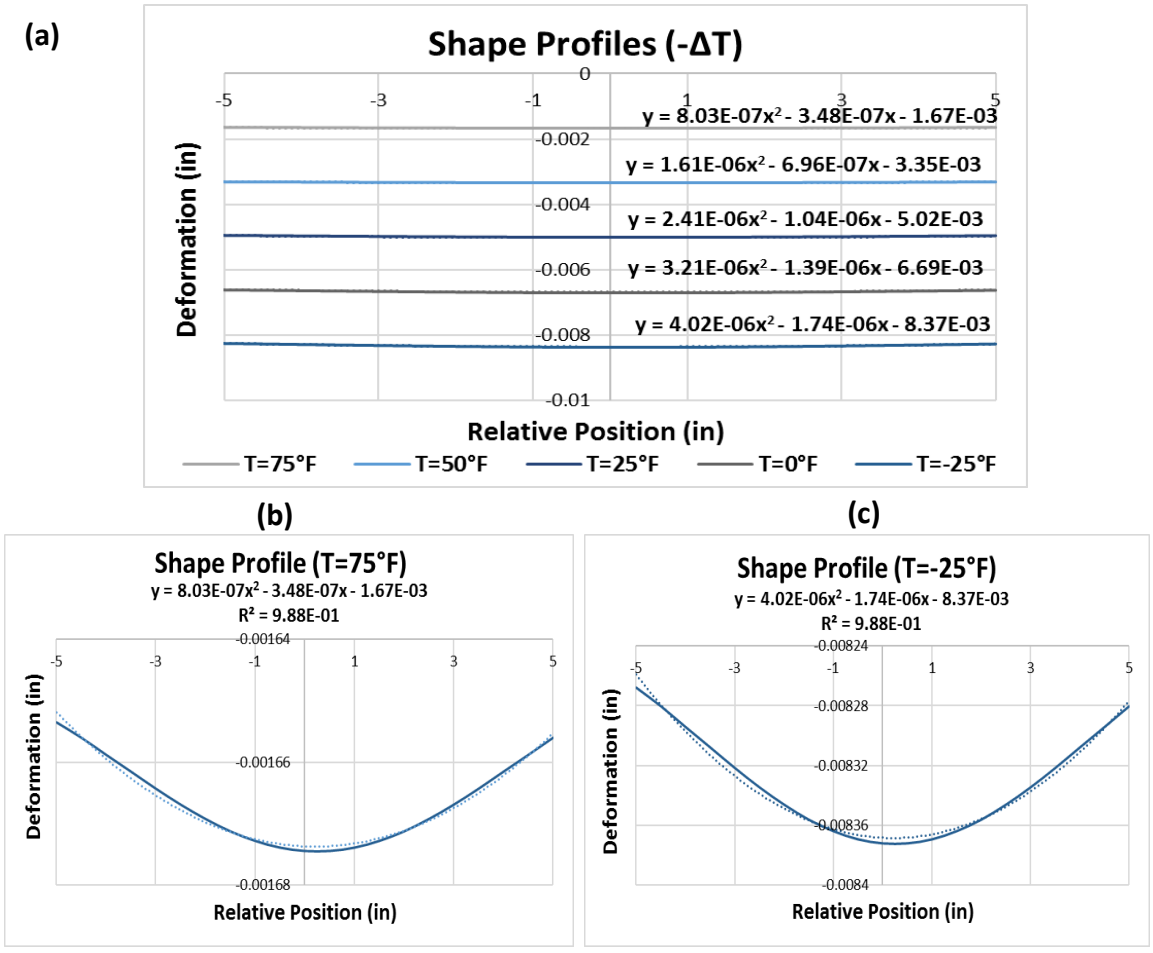

Figure 6.5: Plots of the FE deformed shape measurements along the rail head: (a) Shape profiles for rail temperatures below the RNT; (b) Shape profile at T=75°F (ΔT=-25°F); (c) Shape profile at T=-25°F (ΔT=-125°F)

6.2.2 Strain Measurements

The second set of data acquired by the StereoDIC system includes the longitudinal and transverse strain measurements at the rail web. The strain measurements are obtained for stress computation in rail. An element located at the center of the rail web between two successive ties is used for strain analysis. The element selected is located at a distance 80" along the rail length; the center distance between the 4th and 5th tie support locations. The height of this element is 3.2" from the bottom surface of the rail, the centroidal height for a 132 RE rail cross section. **Figure 6.6** depicts this location of this element along the FE rail and is denoted as element B.

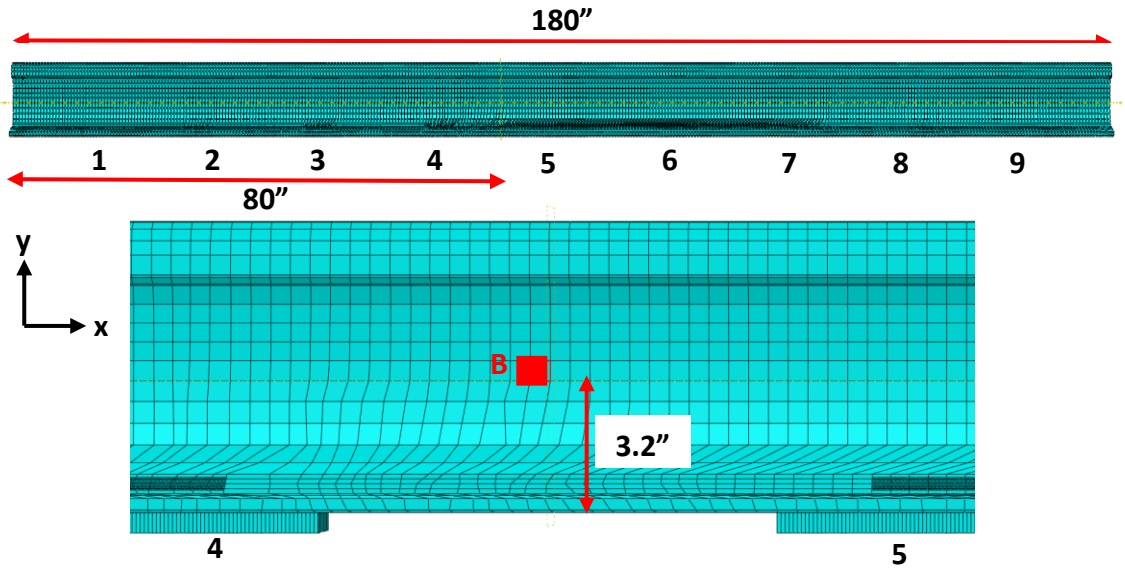

Figure 6.6: FE strain and stress measurements extracted from element B (red square); tie support locations are numbered in black along the rail

The StereoDIC system captures the change in strain with respect to the reference image. At the RNT, the initial strain is considered zero because temperature changes have yet to occur. Because the initial strain is unknown for the temperature state (more than

likely not the RNT) for which the initial reference image is captured, only the slope of the strain with respect to temperature can be obtained. In this simulation, the reference image is taken at the RNT, reference image is taken at the RNT, which is not always true but is done to simplify the procedure. Therefore, prior to implementation of the proposed measurement method on the simulated measurements, the uniquely defined linear relationship between temperature and strain is unknown. The acquired simulated measurements are then the change in temperature with respect to change in longitudinal strain, $\Delta\varepsilon_x$, and transverse strain, $\Delta\varepsilon_y$, as shown in **Figure 6.7** for both positive and negative temperature changes. Significant thermal strain exists transversely, increasing/decreasing linearly with rail temperature change. While the change in longitudinal strain can be considered negligible for all temperatures due to the imposed constraints at the rail ends and/or at the tie supports.

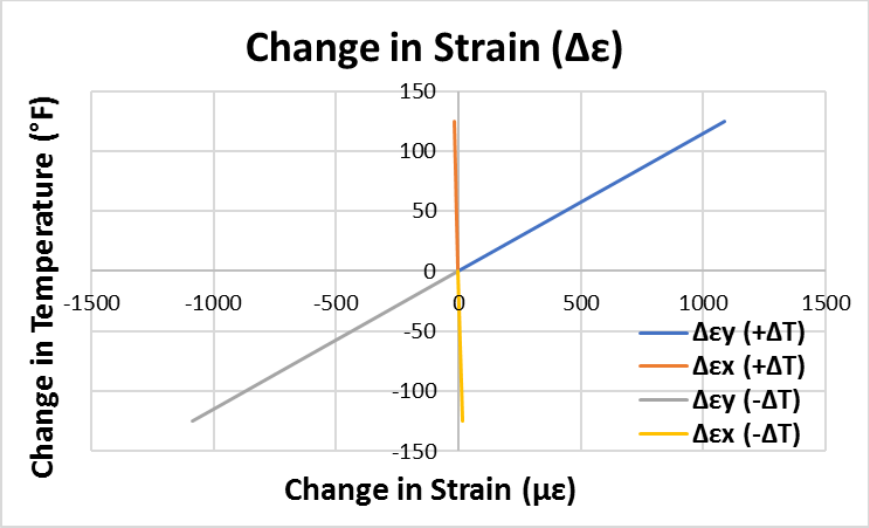

Figure 6.7: Plot of FE simulated measurements depicting change in temperature with respect to change in longitudinal strain, $\Delta\varepsilon_x$, and transverse strain, $\Delta\varepsilon_y$, located at element B

6.3 Demonstration of Proposed Methodology

Upon acquisition of the shape deformation and strain measurements, the proposed methodology can be used to estimate the RNT and the longitudinal stress in rail. The proposed methodology will be demonstrated in two ways: (I) two deformation measurements above the RNT will be selected and (II) two deformation measurements that bracket the RNT – one measurement above and one below the RNT will be selected. With the RNT estimate, the transverse strain can be uniquely defined with temperature for these measurements. Subsequently, the longitudinal stress for all rail temperatures can be estimated by assuming plane stress conditions, as a function of the acquired strain measurements and material properties.

6.3.1 RNT Estimate

The curvature can be computed by taking the second derivative of the quadratic shape trendline equations. This yields a constant which describes the average curvature for the 10-inch rail head section corresponding to a temperature. The curvatures for each temperature are computed for both temperature change cases and are summarized in **Table 6.2** below.

Table 6.2: Curvatures computed corresponding to a rail temperature

ΔT = -125°F		**ΔT = +125°F**	
Curvature (1/in)	**T (°F)**	**Curvature (1/in)**	**T (°F)**
8.04E-06	-25	-8.04E-06	225
6.42E-06	0	-6.42E-06	200
4.82E-06	25	-4.82E-06	175
3.22E-06	50	-3.22E-06	150
1.61E-06	75	-1.61E-06	125

The RNT can now be estimated in a simple and straight forward manner as the y-intercept or temperature corresponding to zero-curvature. Because of the established linear relationship between curvature and temperature, only two measurements are required for the demonstrations.

Demonstration I of the proposed methodology entails selection of two vertical deformation measurements above the RNT. Rail temperatures T = 175°F and T = 125°F are selected and plotted with respect to the curvature computed, as shown in **Figure 6.8(a)**. Through linear extrapolation, the RNT, or y-intercept, is estimated as 100.02°F. Because the actual RNT is known and is predefined in this simulation as 100°F, the error associated with Demonstration I can be calculated as 0.02%. Using the RNT, the simulated temperature-strain relationship captured by the StereoDIC system can now be uniquely plotted, as shown in **Figure 6.8(b)**. The temperature at zero-strain is defined by the RNT.

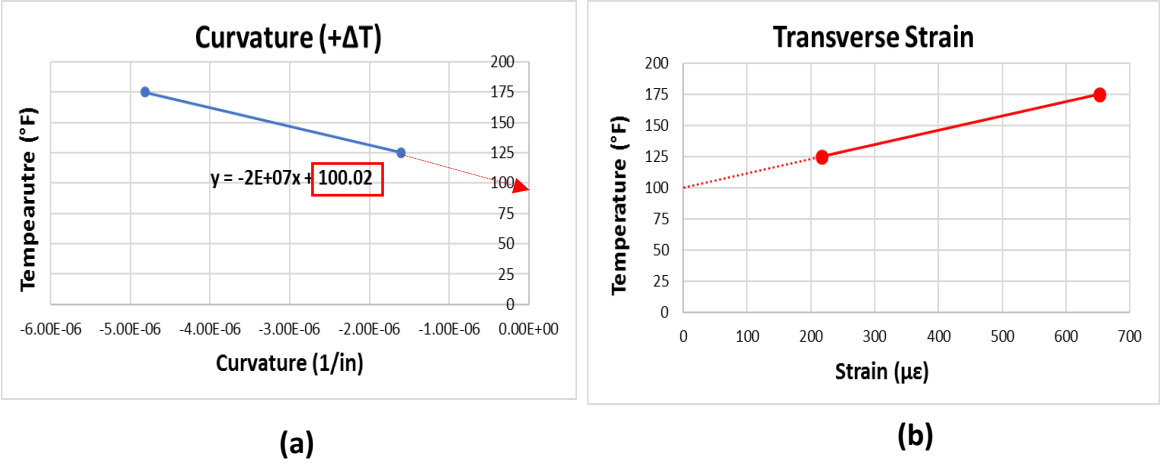

Figure 6.8: Plots of Demonstration I using the proposed methodology: (a) Temperature – cuvature relationship (linear extrapolation used to estimate the RNT); (b) Temperature – transverse strain relationship

Demonstration II of the proposed methodology entails selection of two vertical deformation measurements that bracket the RNT. Rail temperatures T = 150°F and T = 75°F are selected and plotted with respect to the curvature computed, as shown in **Figure 6.9(a).** Through linear interpolation, the RNT, or y-intercept, is estimated as 99.96°F. With the actual RNT known, the error associated with Demonstration II can be calculated as 0.04%. Using the RNT, the simulated temperature-transverse strain relationship captured by the StereoDIC system can now be uniquely plotted, as shown in **Figure 6.9(b)**. The temperature at zero-strain is defined by the RNT.

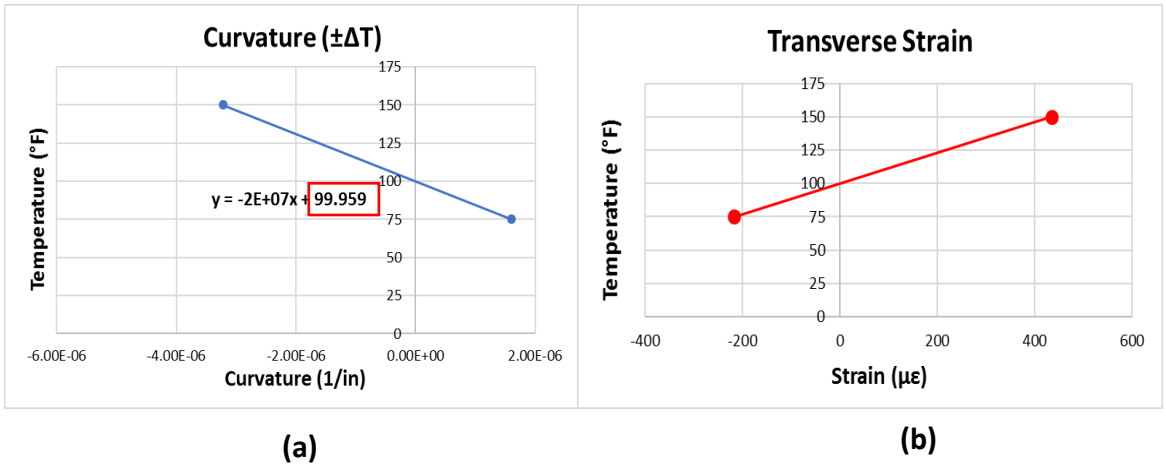

Figure 6.9: Plots of Demonstration II using the proposed methodologys: (a) Temperature-cuvature relationship (linear interpolation used to estimate the RNT); (b) Temperature-transverse strain relationship

Table 6.3 tabulates the simulated strain measurements for all rail temperatures above and below the RNT, which are extracted for analysis. These measurements will be used for implementation of the methodology for longitudinal stress computation in the subsequent section.

Table 6.3: Simulated strain values corresponding to rail web temperatures

Rail Web Longitudinal (ε_x) and Transverse (ε_y) Strain					
ΔT = +125°F			**ΔT = -125°F**		
T (°F)	**ε_y (με)**	**ε_x (με)**	**T (°F)**	**ε_y (με)**	**ε_x (με)**
100	0.00	0.00	100	0.00	0.00
125	217.53	-3.51	75	-217.53	3.51
150	435.07	-7.02	50	-435.07	7.02
175	652.60	-10.54	25	-652.60	10.54
200	870.13	-14.05	0	-870.13	14.05
225	1087.67	-17.56	-25	-1087.67	17.56

6.3.2 Stress Computation

This methodology is founded on the assumption that transversely the rail is stress free. This is because at this rail web cross section, the rail can freely deform allowing significant thermal strain to develop. At this same section, due to the imposed constraints, significant thermal longitudinal stress exists, proportional to temperature change. Without making this initial assumption, the methodology cannot be used to compute the longitudinal stress because too many unknowns would exist to use the plane stress equation. **Figure 6.10** displays the rail temperature with respect to the numerically computed FE longitudinal stress, σ_x, and transverse stress, σ_y. At this time, the proposed methodology has not been used to compute the stress in rail with acquired measurements, but the values in **Figure 6.10** will be used to calculate the error associated with the proposed measurement system. This stress is uniquely defined by the RNT estimate; the rail is stress-free at the predefined RNT, T=100°F. This plot also confirms that the transverse stress, relative to the longitudinal stress, appears negligible and can be considered zero.

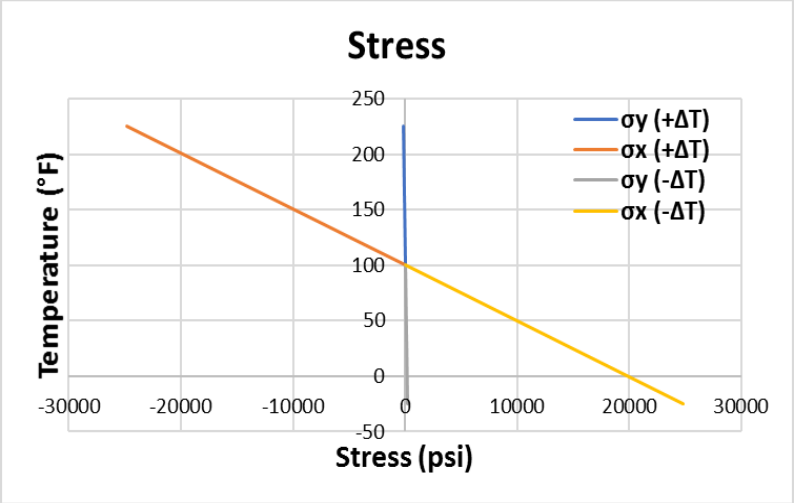

Figure 6.10: Plot of FE simulated temperature in respect to longitudinal and transverse stress at element A

The longitudinal stress, σ_x, will be computed as a function of the acquired strain measurements and material properties using the proposed methodology. The acquired strain values corresponding to a single rail temperature, along with the required elastic material properties of steel, are tabulated in **Table 6.4** for stress computation. Plane stress conditions are assumed.

Table 6.4: Required variables for longitudinal stress computation

FE Extracted Values:	
Temperature (°F)	175
Transverse Strain, ε_y (ε)	$6.52*10^{-4}$
Longitudinal Strain, ε_x (ε)	$-1.05*10^{-5}$
Material Properties:	
Modulus of Elasticity, E (psi)	$29*10^{6}$
Poisson's Ratio, v	0.3

Using the plane stress conditions equation developed in section **3.4**, the longitudinal stress, σ_x, can be computed with the following equation:

$$\sigma_x = \left(\varepsilon_x - \varepsilon_y\right)\frac{E}{(1+v)} + \sigma_y \tag{18}$$

Under the assumption that the rail is considered stress-free in the transverse direction (σ_Y = 0), the values given in **Table 6.4** can be inputted into the equation and the longitudinal stress, σ_x, can be directly solved as:

$$\sigma_x = (-1.05 * 10^{-5} - 6.52 * 10^{-4})\frac{29*10^6}{(1+0.3)} + 0 \tag{19}$$

$$\sigma_x = -14.79\ ksi$$

Using the proposed methodology, the longitudinal stress at T = 175°F is computed as σ_x = -14.79 ksi, yielding a 0.76% error with the actual numerically computed longitudinal stress, provided in **Figure 6.10**. This methodology requires the assumption to be made that transversely the rail is stress free, otherwise the longitudinal stress cannot be computed. For the purposes of comparing σ_Y = 0 to $\sigma_Y \neq 0$, the actual FE obtained transverse stress, σ_Y = -0.11 ksi, is inputted into the plane stress equation. The computed longitudinal stress when $\sigma_Y \neq 0$ then becomes:

$$\sigma_x = (-1.05 * 10^{-5} - 6.52 * 10^{-4})\frac{29*10^6}{(1+0.3)} - 0.11 \tag{20}$$

$$\sigma_x = -14.91\ ksi$$

By including the insignificant FE computed transverse stress, the calculated percent error becomes 0.00%. This confirms that assuming plane stress conditions is an acceptable assumption for this measurement system method. This process is repeated for all additional rail temperatures, and the longitudinal stress is computed considering σ_Y = 0

and $\sigma_Y \neq 0$, with the corresponding percent error for analysis. These computations are summarized in **Table 6.5** below. While the stress is computed for all rail temperatures, realistically only two stress measurements need to be computed because of the linear relationship that exists between temperature and stress. When the transverse stress is not assumed as zero, $\sigma_Y \neq 0$, the percent error for all data sets is 0.0%. However, when the rail is considered stress-free, $\sigma_Y = 0$, the percent error for all data sets is less than 1.0%.

Table 6.5: Rail temperature corresponding to the calculated longitudinal stress and the associated percent error

Longitudinal Stress σ_x (+ΔT)					
T (°F)	**Actual σ_x (ksi)**	**σ_x (σ_y=0) (ksi)**	**% Error (σ_y=0)**	**σ_x ($\sigma_y \neq 0$) (ksi)**	**% Error ($\sigma_y \neq 0$)**
100	0	0	0.00%	0.00	0.00%
125	-4.97	-4.93	0.76%	-4.97	0.00%
150	-9.94	-9.86	0.76%	-9.94	0.00%
175	-14.91	-14.79	0.76%	-14.91	0.00%
200	-19.87	-19.72	0.76%	-19.87	0.00%
225	-24.84	-24.66	0.76%	-24.84	0.00%
Longitudinal Stress σ_x(-ΔT)					
T (°F)	**Actual σ_x (ksi)**	**σ_x (σ_y=0) (ksi)**	**% Error (σ_y=0)**	**σ_x ($\sigma_y \neq 0$) (ksi)**	**% Error ($\sigma_y \neq 0$)**
100	0.00	0.00	0.00%	0.00	0.00%
75	4.97	4.93	0.76%	4.97	0.00%
50	9.94	9.86	0.76%	9.94	0.00%
25	14.91	14.79	0.76%	14.91	0.00%
0	19.87	19.72	0.76%	19.87	0.00%
-25	24.84	24.66	0.76%	24.84	0.00%

Therefore, it is concluded that the insignificant transverse stress computed numerically by the FE model can be considered negligible to accurately compute the longitudinal stress with only a 1% error using the proposed methodology. Thus, at any rail temperature, the longitudinal stress can be estimated as shown in **Figure 6.11**. The temperature at which longitudinal stress is zero, approximately T = 100°F, is the

computed RNT estimate. When the rail temperature is above the RNT (red), the rail is in compression, and when the rail temperature is below the RNT (blue), the rail is in tension.

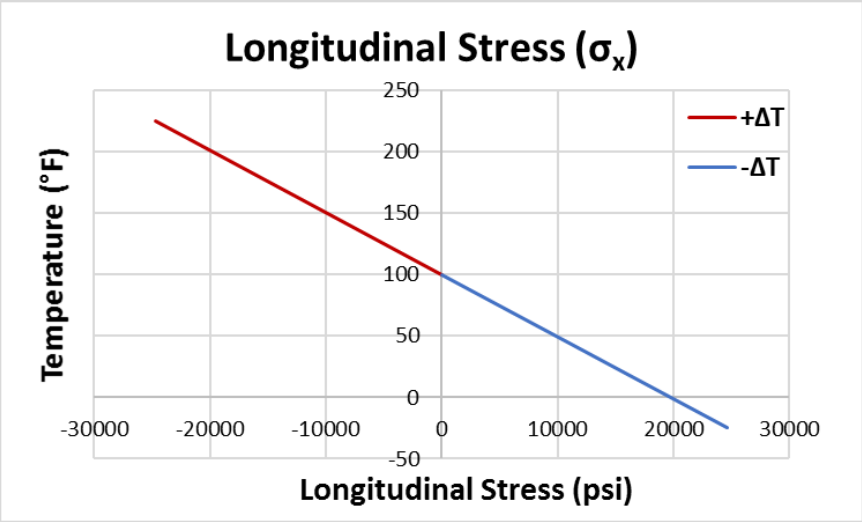

Figure 6.11: Plot of temperature with respect to longitudinal stress computed with the proposed methodology

6.4 Discussion of Results and Observations

After implementation of the proposed methodology on the computer simulated data it is found that this method can accurately estimate the RNT and longitudinal stress in rail. This confirms the initial hypotheses that this measurement method is develop on. Thermal loads induce local flexure between successive ties due to the level of constraint. This local flexure produces measurable deformed shape profiles along the rail head that are used to compute curvature. The rail head temperature is then plotted in respect to curvature to successfully estimate the RNT. Demonstration I and II are performed to estimate the RNT using only two unique temperature-curvature states and are compared to the actual pre-defined RNT. In Demonstration I the RNT is estimated with 0.02% error, and in Demonstration II, the RNT is estimated with 0.04% error. Overall, both

demonstrations confirm that the RNT can be accurately estimated with a ± 1°F confidence. These RNT estimates are then used to uniquely define the relationship between rail temperature and the acquired strain measurements. The thermal strain is then used to estimate the longitudinal stress. At a center web cross section between two successive ties, transversely, significant thermal strain develops proportionally to temperature change, while the thermal stress can be considered negligible. The opposite relationship exists in the longitudinal direction. The transverse strain is then indicative of the longitudinal stress. Using the proposed methodology which assumes that transversely the rail is stress-free, the longitudinal stress can be estimated under plane stress conditions for less than a 1% error of the actual longitudinal stress computed numerically by the FE model. In conclusion, this simulation verifies that the proposed measurement system can be implemented to accurately estimate the RNT and stress in rail and demonstrates the feasibility of complete implementation of this method for future laboratory experimentation and field testing.

Chapter 7. Conclusion and Recommendations

7.1 Conclusions

This thesis presents a novel method that demonstrates the feasibility to develop the non-contacting, reference-free measurement system and set the foundations for the design of a full-scale prototype rail system. The proposed system and method are developed to uniquely estimate the RNT and the rail longitudinal state of stress. A FE qualitative analysis is initially performed to define the type of deformation data to be expected for experimental testing. A small-scale prototype is constructed in view of these observations and deformation and strain measurements are captured using the proposed StereoDIC system. 3D FE thermoelastic computer models are developed and designed to simulate laboratory testing for validation. The experimental data and FE computer simulations verify and validate the initial observations that are subsequently used to develop the complete RNT and stress measurement methodology. The FE models are then developed to simulate a full-scale rail system to investigate various parameters that may affect the experimental measurements. The parametric study findings will also serve as a guide for the construction of a full-scale track system in the Railway Testing Facility at USC. The investigated parameters include the effects of boundary conditions, FE analysis types, heating surface area methods, rail geometry, track stiffness, and tie

spacing. A computer model is then selected to simulate the acquisition of measurements by the StereoDIC system, followed by implementation of the method for RNT estimation and stress computation for verification of the proposed measurement system. This demonstrates the ability to use this technique on a full-scale rail system.

Upon completion of this work, the following conclusions can be made:

- Experimental data and FE solutions verify and validate that thermal loads will induce local flexure between two successive ties, causing measurable thermal deformations along the rail head that the StereoDIC system can capture.
    - The experimental prototype system confirms that the level of constraint directly affects the thermal longitudinal strain, while the transverse strain remains free and unaffected.
    - The FE model can be used to accurately estimate the strain for the free rail specimen. In contrast, the strain for the partially constrained rail cannot be accurately estimated because the stiffness imposed by the fabricated supports is unknown. Only the upper and lower limit of thermal strain can be predicted with the FE model for this rail specimen.
    - Despite various experimental sources of errors, the acquired measurements appear to accurately capture the strain between the supports and adequately estimate the RNT.
- Computer simulations on the full-scale track models are conducted to investigate the critical parameters that affect the thermal deformation and strain

measurements. Findings of these simulations will guide future construction of the indoor testing track and field testing.

- Vertical deformation measurements are considered along the rail head and base flange. The rail head shape deformations are far above the proposed technology lower limit of accuracy, but the change in deformation is small which may lead to challenges concerning the noise in measurements. In contrast, the rail base flange shape deformations are much smaller, residing below the lower limit of accuracy of the proposed instrumentation, but the change in deformation is much larger relative to the rail head. Because the deformations are much higher in the rail head, and experimental testing simply obtained the changes in deformation along the rail head, the rail head is primarily used for analysis.
- Additionally, the regions between two successive ties and about the anchoring points are considered. It is found that the region between two successive ties produces a more uniform curvature and therefore, will be the region primarily used for analysis.
- The most critical parameter investigated pertains to the rail boundary conditions, including either the level of longitudinal constraint at the rail ends or the vertical constraint at the tie supports. These two boundary conditions behave synergistically; either must be fully constrained to induce practical deformations along the rail. If only the vertical tie supports

are fully constrained, measurements must be captured within the three center ties to eliminate the impractical rail end affects.

- Additional significant parametric findings pertain to the tie spacing and the heating surface area. An increase in tie spacing or an increase in the heating surface area/volume or application of heat to thinner rail regions, independently, causes an increase in the shape deformations and changes in deformations.
- The track stiffness and rail geometry had insignificant effects on thermal deformation and strain measurements. Therefore, this method can be simply implemented on any track system where these parameters may vary.

- Implementation of the complete RNT and stress measurement method on computer simulated data led to successful findings that verifies the feasibility of implementing this method on a full-scale track system.
  - The deformed shape profiles are used to accurately compute the average curvatures corresponding to a known rail temperature. The two demonstrations confirm that the RNT can be estimated with a ± 1°F confidence of the actual RNT.
  - FE solutions confirm that plane stress conditions in the rail web region is an accurate assumption in estimating the longitudinal stress.
  - FE solutions confirm that the transverse stress can be considered negligible for all rail temperatures to estimate the longitudinal stress.

- The longitudinal stress can be accurately estimated with less than a 1% error of the numerically computed FE solution, using the proposed methodology.

7.2 Recommendations

While this thesis successfully demonstrates the feasibility of the proposed measurement system, this is only the initial phase of a multi-phase project. This work provides a preliminary guide for future implementation of this method on a full-scale prototype system, followed by field testing. The recommendations made for future work consider both experimental and modeling recommendations.

Experimental:

- Investigate alternate methods of ensuring complete longitudinal constraint at the rail ends or vertical constraint at the tie supports. The small-scale prototype system required welding procedures to constrain the rail specimen, an impractical method of ensuring this constraint for a full-scale system. This approach also only partially constrains the rail specimen, whereas full constraint is necessary.
- Additional experimental heating techniques should be explored that minimize issues with non-uniform heat distributions, the speed of heat dissipation, and limit the heat applied to the supports.
- The StereoDIC system should be equipped with full-field thermal cameras to synchronize deformations measurements with thermal readings. The obtained

thermal field could also be used to adequately assess the temperature distribution uniformity.

- Construction of the full-scale track system on the indoor track bed at the Railway Testing Facility should utilize the effects that increased tie spacing and heating surface area have on the measurement data.
- Patterning the specimen requires a meticulous effort and can be very time consuming; it would be ideal to investigate other patterning techniques that create the necessary high contrast pattern on the specimen, but in a more time efficient way.

Modeling:

- Thermal properties should be defined for the other track components in the model, rather than only the rail. The effects of heat flow throughout track components of varying material properties could then be investigated. Additionally, it would eliminate any modeling irregularities due to the rail's inability to transfer heat to the tied track components.
- The fastener component could be developed into a more intricate model design. This thesis found that the inclusion of this component unnecessary. In the field, this component is incorporated to help secure the rail to the ties, so if it were more adequately modeled, perhaps it may further tie down the rail at the anchoring points.
- Calibrate FE models with experimental data from field and/or laboratory testing.

- Consider use of non-uniform heat flux loading techniques to investigate deformation patterns when exposing some rail sections to a higher heat intensity than others. For example, in the field, one side of the rail has more sun exposure compared to the other side of the rail depending on the time of day.
- Develop a full track system model that considers two adjacent rail segments and investigate the relationship the two rails may have on one another throughout a thermal loading cycle.

References

Abdulqader, Ali Haider. 2017. *Production Qualification and Performance Assesment of HSRM Prestressed Concrete Railroad Ties Through Laboratory Testing.* Thesis, Columbia: University of South Carolina.

Agico Group. 2019. *Rail Joint.* Accessed September 12, 2019. http://www.railjoint.com/news/the-function-of-rail-fastening-system.html.

Alers, George A., and Alfonoso Manzanares. 1990. "Use of surface skimming SH waves to measure thermal and residual stresses in installed railroad tracks." *Review of Progress in Quantitative Nondestructive Evaluation* 1757-1764.

Arts, T, M.A. 2011. *Measuring the Neutral Temperature in Railway Track During Installation and Use.* Thesis Report Delft University of Technology.

Austill, Robert J. 1991. Process for Determining and Controlling Railroad Rail's Neutral Temperature to Prevent Track Buckling and Rail Fractures. U.S.A. Patent 5, 655,120.

Bartelmo, S., S. Rajan, N. Li, M. A. Sutton, and D. C. Rizos. 2016. "Digital Image Correlation Techniques for Prestressed Concrete Tie Quality Control." *Proceedings of the 2016 Joint Rail Conference.* Columbia.

Boston University Mechanical Engineering. 2019. *Mechanics of Materials: Stress Transformation.* Accessed September 16, 2019. https://www.bu.edu/moss/mechanics-of-materials-stress-transformation/.

Chinowsky, Paul , Jacob Helman, Sahil Gulati, James Neumann, and Jeremy Martinich. 2019. "Impacts of climate change on operation of the US rail network." *Transport Policy* 75: 183-191. Accessed 2019. doi:10.1016/j.transpol.2017.05.007.

Correlated Solutions, Inc. . 2019. *Correlated Solutions- Non-Contacting Measurement Solutions.* Accessed September 8, 2019. https://www.correlatedsolutions.com/.

Dassault Systèmes Simulia Corporation. n.d. *ABAQUS User's Manual (6.12).*

Elert, Glenn. n.d. *The Physics Factbook.* Accessed September 12, 2019. https://hypertextbook.com/facts/2005/steel.shtml.

Federal Railroad Administration. 2019. "Continuous Welded Rail Generic Plan." *Federal Railroad Administration-Office of Safety Analysis.* September 17. Accessed September 17, 2019. http://safetydata.fra.dot.gov/officeofsafety/Documents/CWR_GenericPlan_1_8_18_Final.pdf.

Harmer Steel Co. 2014. *Harmer Steel Products Co. .* http://www.harmersteel.com/v2/wp-content/uploads/Harmer_Steel_Catalog-2015.pdf.

Hauk, Viktor. 1997. "X-ray Diffraction." In *Structural and Residual Stress Analysis by Nondestructive Methods*, by Viktor Hauk, 17-494. Elsevier Science.

Johnson, Erland. 2004. *Measurement of forces and neutral temperatures in railway rails - an introductory study.* SP Report, Boras: Building Technology and Mechanics.

Kelly, P. 2015. *Solid Mechanics Book.*

Kish, A. 2013. "Best Practice Guidelines for CWR Neutral Temperature Management." *in: Proceedings of hte 2013 AREMA Annual Conference.* Indianapoli, IN.

Kish, A., and G. Samavedam. 2013. *Track Buckling Prevention: Theory Safety Concepts and Applications.* Final Report, Report# DOT/FRA/ORD-13/16.

Kish, Andrew. 2005. "Improved Destressing of Continuous Welded Rail For Better Management of Rail Neutral Temperature." *Transportation Research Record* 1916: 0361-1981.

Kjell, G., and E. Johnson. 2009. "Measuring axial forces in rail by forced vibrations: experiences from a full scale laboratory experiment." *Proceedings of the Institution of Mechanical Engineers, Part F: Journal of Rail and Rapid Transi* 241-254.

Liu, X, X Qin, M R Saat, and C P Barkan. 2013. "Analysis of U.S. freight-train derailment severity using zero-truncated negative binomial regression and quantile regression." *Accident Analysis & Prevention* 87-93. doi:10.1016/j.aap.2013.04.039.

Orringer, O., J. M. Morris, and D. Y. Jeong. 1986. "Detail Fracture Growth in Rails: Test Results." *Theoretical and Applied Fracture Mechanics* 63-95.

Palese, Joseph W, and Allan M Zarembski. 2006. "Managing Risk on the Railway Infrastructure." *Proceedings of the 7th World Congress on Railway Research.* Montreal.

Pandrol USA. 2019. "Pandrol Track Systems 'e' clip Product Brochure." *Pandrol USA.* Accessed September 16, 2019. https://www.pandrolusa.com/product/e-clip/.

Phillips, Robert, Xuan Zhu, and Francesco Lanza di Scalea. 2012. "The Influence of Stress on Electro-mechanical Impedance Measurements in Rail Steel." *Materials Evaluation* 70 (10): 1213-1218.

Posgay, Gyorgy, Ferenc Varga, Peter Molnar, Tibor Zsakai, Alfonz Szamos, Janos Beli, and Jozsef Vegi. 1999. Method and Device for Determing the Neutral Temperature of Welded Tracks. U.S.A. Patent 5,992,241.

RailTEC - University of Illinois at Urbana-Champaign. n.d. *Study of Modified Rail Joint Bolt-Hole Arrangement Options Volume - I.* Final Project Report, New York City Transit Authortiy.

Rajan, S., M. A. Sutton, D. C. Rizos, A. R. Ortiz, and J. M. Caicedo. 2017. "A Stereovision Deformation Measurement System for Transfer Length Estimates in Prestress Concrete." *Experimental Mechanics* 1-14.

Rizzo, Piervincenzo, and Amir Nasrollahi. 2019. "Numerical Analysis and Experimental Validation of an Nondestructive Evaluation Method to Measure Stress in Rails." *Journal of Nondestructive Evaluation, Diagnostics and Prognostics of Engineering Systems* 2 (3): 031002-1 - 031002-12.

Ruud, Clayton O. 1979. "X-Ray Diffraction Analysis for Railroad Rail." *Nondestructive Techniques for Measuring the Longitudinal Force in Rails: Proceedings of a Joint Government-Industry Conference.* Washington, D.C. : FRA. 160-165.

Schreier, Hubert, Jean-Jose Orteu, and Michael A. Sutton. 2009. *Image Correlation for Shape, Motion, and Deformation Measurements.* Springer US.

Sutton, M. A., J. H. Yan, V. Tiwari, H. W. Schreier, and J. J. Orteu. 2008. "The effect of out-of-plan motion on 2D and 3D digital image correlation measurements." *Optics an Lasers in Engineering* 46 (10): 746-757.

Synnergren, P., and M. Sjok. 1999. "A stereoscopicdigital speckle photography system for 3-D displacement field measurements." *Optics and Lasers in Engineering* 31: 425-443.

Szelazek, J. 1998. "Monitoring of thermal stresses in continuously welded rails with ultrasonic technique." *NDTnet.*

Timoshenko, S., and B. F. Langer. 1932. "Stresses in Railroad Tracks." *Transactions* 54: 277-302.

Weaver, Richard L., and Vesna Damljanovic. 2005. "Laser vibrometry technique for measurement of contained sress in railroad rail." *Journal of Sound and Vibration* 341-366.

Wegner, Alfred . 2007. "Prevention of Track Buckling and Rail Fracture by Non-Destructive Testing of the Neutral Temperature in cw-Rails." *Proceedings of the International Heavy Haul Conference (IHHA).* Kiruna, Sweeden: IHHA. 557-564.

White, John G. 1984. "Concrete Tie Track System." *Transportiation Research Record* 5-11.

Zhu, Xuan, and Francesco Lanza di Scalea. 2016. "Sensitivity of Axial Stress of Electro-Mechanical Impedance Measurements." *Experimental Mechanics* 56 (9): 1599-1610.